博士論文

Polymer Structure and Processing of Newly-Developed Films

新規フィルムの構造と成形加工

金沢大学大学院自然科学研究科
物質科学専攻
先端機能物質講座

学　籍　番　号　　1123132313
氏　　　　　名　　細田　友則
主任指導教員名　　山田　敏郎　教授

A Doctoral Dissertation

Polymer Structure and Processing of Newly-Developed Films

Kanazawa University

Graduate School of Natural Science & Technology

Division of Material Sciences

ID No.   1123132313

Name,   Tomonori Hosoda

Supervisor, Professor Toshiro Yamada

Contents

Chapter 3.   Effect of TiO₂ on morphology and mechanical properties of PVDF/PMMA blend films prepared by melt casting process

Chapter 4.   Morphological study of PVDF/PMMA/TiO₂ blend films prepared by melt casting process

Acknowledgements

ABSTRUCT

Effect of solvents and thermal annealing on the morphology development of sulfonated polystyrene-*b*-fluorinated polyisoprene (s-PS-*b*-f-PI) and property-morphology-processing relationship on poly(vinylidene fluoride) (PVDF)/poly(methyl methacrylate) (PMMA)/titanium dioxide (TiO_2) blend films were studied.

The film of the block copolymer ionomer with acid form (sH-PS-*b*-f-PI) cast from anhydrous tetrahydrofuran (THF) formed a well-ordered cylindrical morphology which was to be explicable in terms of the solvent effect and the Bjerrum length. However, the morphology changed to the no-long range ordered structure by thermal annealing. This result was very different from the usual behavior of uncharged block copolymers. The study on the film of the block copolymer ionomer with a cesium neutralized form (sCs-PS-*b*-f-PI) revealed that a small amount of water and thermal annealing promoted the ionic cluster formation. The result was to be indicated the order-disorder transition of sH-PS-*b*-f-PI.

PVDF/PMMA/TiO_2 blend films were prepared by a melt casting process. Morphological observation indicated that the TiO_2 particles did not affect the crystal structure of PVDF and the morphology of PVDF/PMMA amorphous phase. The decrease of crystallinity with increasing TiO_2 particles was due to the hindrance of crystal growth by some TiO_2 particles, even though different TiO_2 particles acted as a nucleus regent. It was clarified that the anisotropic elongation at break was due to the anisotropic morphology of spherulites. In addition, the crystal structure of PVDF was dominated by the chill roll temperature. It was deduced that a large amount of PMMA was entrapped within interlamellar region in the spherulites composed of α phase and that the storage modulus (E′) was related to the actual weight fraction of PMMA in the mixed amorphous phase.

The study revealed that the microphase-separated structure of the newly-synthesized block copolymer ionomers was affected by the solvent effect

and the Bjerrum length and the ionic cluster formation using small angle x-ray scattering (SAXS), intermediate angle x-ray diffraction (IMAXD), and transmission electron microscopy (TEM). In the study of PVDF/PMMA/TiO$_2$ blend films prepared by a melt casting process, the elongation at break was dominated by the anisotropic morphology of spherulites, and we clarified that the storage modulus above glass transition temperature (T$_g$) was influenced by the ratio of PVDF and PMMA. Such mechanical properties are one of the important properties in practical usage, and it is thought that the conclusion of the thesis gives valid points of view and analytical approaches for functionalizing block copolymers and multicomponent polymer blends, hereafter.

List of Abbreviations

Ai	Constant value defined by morphology
DMA	Dynamic mechanical analysis
DFMC	Direct methanol fuel cell
DMSO	Dimethylsulfoxide
DSC	Differential scanning calorimetry
E [Mpa]	Tensile modulus of blend material
E_1 [MPa]	Tensile modulus of component 1
E_2 [MPa]	Tensile modulus of component 2
E´	Storage modulus
E″	Loss modulus
E_m [MPa]	Tensile modulus of matrix
E_d [MPa]	Tensile modulus of domain
FT-IR	Fourier transform infrared spectroscopy
GPC	Gel permeation chromatography
h	hour
IMAXD	Intermediate angle x-ray scattering
IUPAC	International union of pure and applied chemistry
LCST	Lower critical solution temperature
MD	Machine direction
MeOH	Methanol
MEK	Methyl ethyl ketone
M_n	Number average molecular weight
M_w	Weight average molecular weight
N	Degree of polymerization
Na^+	Sodium ions
NMR	Nuclear magnetic resonance
PS-PIB-PS	Poly(styrene-*b*-isobutylene-*b*-styrene)
OBDD	Ordered bicontinuous diamond
PA6	Polyamide 6
PCT	Pressure cooker test
PEMFC	Proton exchange membrane fuel cell
PI	Polyisoprene
PCL/PVC	Poly(ε-caprolactone)/poly(vinyl chloride)
PB	Polybutadiene
PS	Polystyrene

PVDF	Poly(vinylidene fluoride)
PMMA	Poly(methyl methacrylate)
s	Second
SAXS	Small angle x-ray scattering
SBS	Polystyrene-polybutadiene-polystyrene block copolymer
SCFT	Self-consistent field theory
SEM	Scanning electron microscopy
scSBS	Sulfonated cross-linked poly(styrene-b-butadiene-b-styrene)
sCs-PS-b-f-PI	Sulfonated polystyrene-b-fluorinated polyisoprene with a cesium neutralized form
sH-SEBS	Sulfonated SEBS
sH-PS-b-f-PI	Sulfonated polystyrene-b-fluorinated polyisoprene with an acid form
sNa-SEBS	Alkali-metal-neutralized ionomers with Na salts
s-PS-b-f-PI	Sulfonated polystyrene-b-fluorinated polyisoprene
SSL	Strong segregation limit
sSEBS	Sulfonated poly(styrene-b-(ethylene-r-butylene)-b-styrene)
s-SEBS	Sulfonated polystyrene-b-poly(ethylene-ran-butylene)-b-polystyrene copolymer
sZn-SEBS	Sulfonated SEBS with zinc salts
TEM	Transmission electron microscopy
TD	Transverse direction
T_g	Glass transition temperature
THF	Tetrahydrofuran
TiO_2	Titanium dioxide
T_m	Melting temperature
UCST	Upper critical solution temperature
UV	Ultraviolet
vol%	Percent by volume
WAXD	Wide angel x-ray scattering
WSL	Weak segregation limit
wt%	Percent by weight
wt/wt	Weight ratio
Zn^+	Zinc ion
φ_1	Volume fraction of component 1
φ_2	Volume fraction of component 2
υ	Poisson's ratio

υ_m	Poisson's ratio of matrix
υ_d	Poisson's ratio of domain
φ_m	Volume fraction of matrix
φ_d	Volume fraction of domain
χ	Kai parameter

Chapter 1.

Introduction

1.1 Overview

According to International Union of Pure and Applied Chemistry (IUPAC), polymer is defined as a molecule of high relative molecular mass, the structure of which essentially comprises the multiple repetition of units derived, actually or conceptually, from molecules of low relative molecular mass. Thus, polymer is something like a long chain, and plastic materials (polymer) which is indispensable our life are consisted by assembly of myriad chains. As an essential character of polymer, large flexibility of a molecule is designated. Owing to its flexibility, a polymer chain forms various morphologies which are affected by polymer process conditions. Control of morphology is one of the most important technologies in the field of polymer science, and there are many reports on properties-morphology relationship [1-3]. Molecular orientation and crystallinity for polymer blends and homopolymer strongly influences properties of mold products (film, fiber). Polymer chains form random coil structures in a polymer solution and a melt state, and high modulus and strength of mold products are obtained by a stretching process causing the molecular orientation. The value of tensile modulus of ultrahigh molecular weight polyethylene film obtained from the single crystal mat attained 210~220 GPa using uniaxially drawn techniques [4]. In addition, it was reported that mechanical properties and dimensional stability of mold products with were improved by the annealing. This was because of the relaxation of molecular segments in the amorphous phase and the increase of crystallinity promoted by the annealing [5-7].

Film properties of block copolymers and multicomponent polymer blends are subject to conditions of processing such as mixing, drawing, extrusion, molding or forming, and various morphologies are formed with different process conditions. In general, for polymer blend materials composed of different kinds of polymer, a component forms either matrix or domain phase because each component usually immiscible each other at the molecular level, and μm-scale order structures are commonly observed. On the other hand, for block copolymers that different polymers are combined with a chemical

bonding, each block can not be made apart at a certain distance or more because of a chemical bonding between each block. As a result, microphase-separated structure, form 10 nm to 1 μm scale order, is formed. The morphology-mechanical property relation was investigated on a polystyrene-polybutadiene-polystyrene (SBS) block copolymer cast from different solvents. As seen Figure 1-1 and 1-2, as-cast films with lamellar morphology always exhibit high moduli and "plastic-to rubber" transitions, while those with PS-dispersed-in-PB-matrix morphology always exhibited low moduli and cross-linked rubberlike behavior [1].
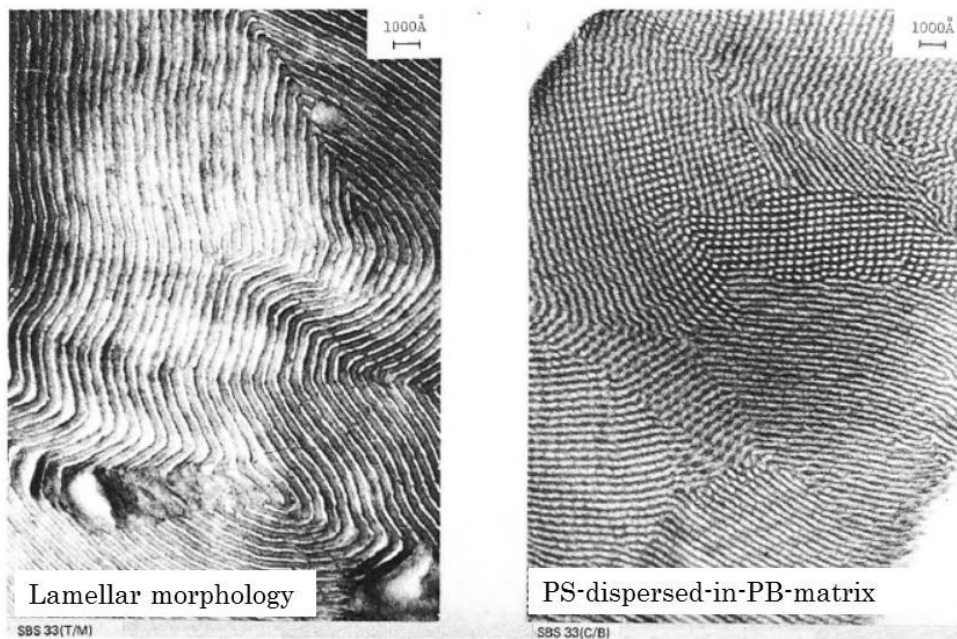
Figure 1 -1 Electron micrographs of SBS films cast from different solvents.
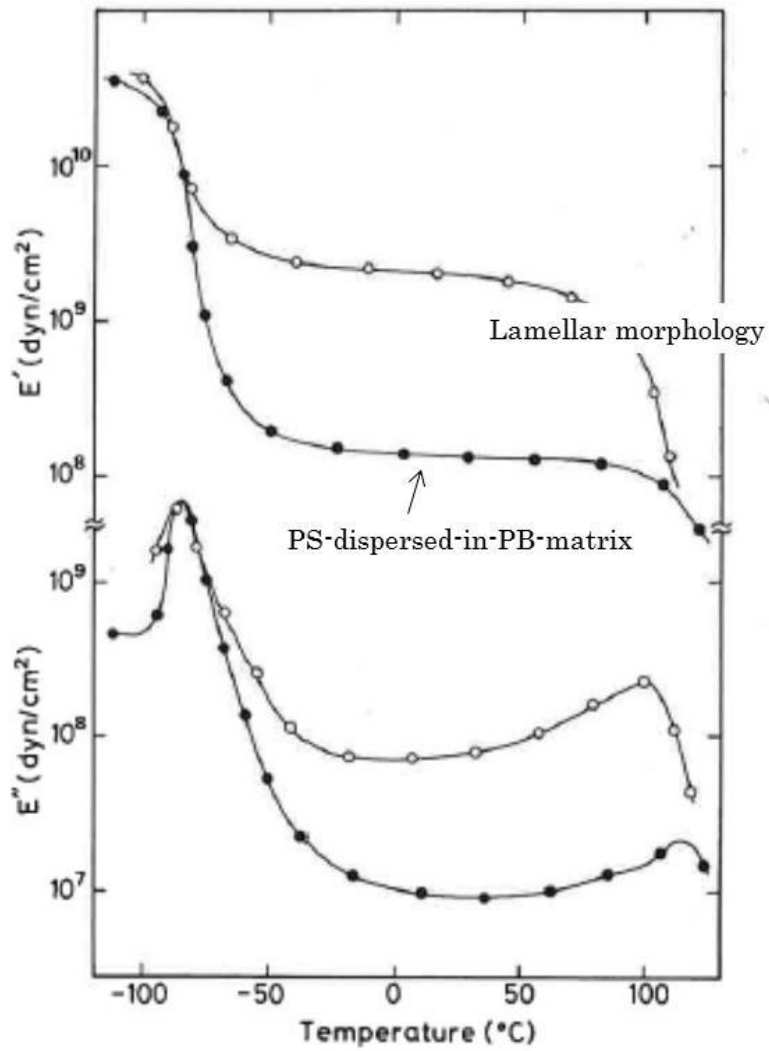
Figure 1 -2 Dynamic storage E' and loss E″ moduli versus temper5ature for SBS films cast from different solvents.

The morphology reported to date for two components systems (AB and ABA types) and star block AB copolymers are represented in Figure 1-3. As seen in the Figure, it is well known that block copolymers form equilibrium morphology: lamellar, spherical imbedded in a continuous phase, cylindrical in a continuous phase and ordered bicontinuous diamond (OBDD).
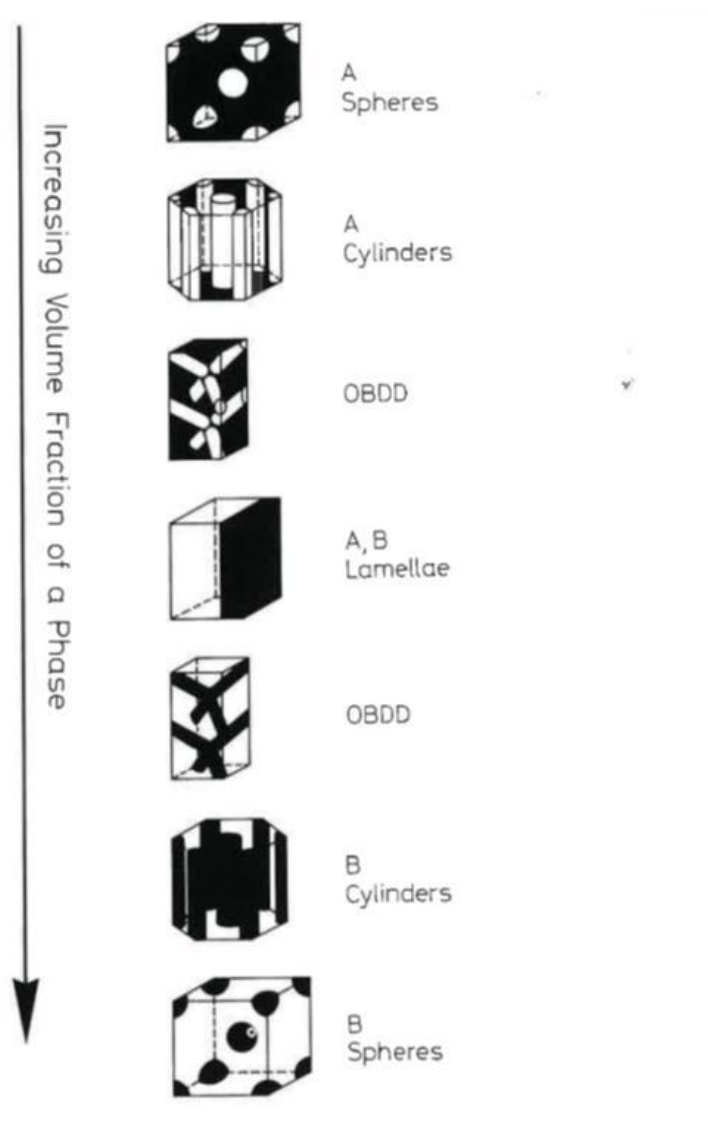
Figure 1-3 Phase separation morphologies for AB type block copolymers.

The strong segregation limit (SSL) theory, the weak segregation limit (WSL) theory, and the self-consistent field theory (SCFT) are known as a thermodynamic theory of microphase separation on block copolymers. Those theories are based on free energy of a polymer chain and an interface [8-13]. Based on the theories, we can predict an equilibrium morphology of a block copolymer. However, in practical cases, nonequilibrium morphologies are often formed in the solution casting films [13-14]. This is due to a solvent effect that polymer chains should be extended in a good solvent and attractive in a poor solvent, and a solvent give an effect until the last evaporation stage. Since properties (mechanical properties, permeability of a low molecule) for films forming microphase-separated structures are strongly affected by morphologies [1,15]. Therefore, morphological control is a worthy for practical usage and industry.

Recently, proton exchange membrane fuel cell (PEMFC) and direct methanol fuel cell (DMFC) are extremely attractive as power sources for transportation, distributed power, and portable electrical devices, because those power sources do not rely on fossil fuels. Membranes for PEMFC are required to have a higher proton conductivity for practical usage. At present, Nafion (DuPont, Wilmington, DE, USA) which is one of the perfluorinated ionomers is widely used in industry. However, Nafion is very expensive, and alternative membranes with economic efficiency are more desirable. According to the study of the sulfonated block copolymer ionomer and Nafion membrane, proton conduction occurred through the ionic channels of the membranes, and these channels were formed by micro- or nanophase separation between the hydrophilic proton exchange sites and the hydrophobic domain [16]. In addition, Kim et al. investigated proton conductivity of sulfonated polystyrene-*b*-poly(ethylene-ran-butylene)-*b*-polystyrene copolymers (s-SEBS) with regard to as a function of sulfonation degree. Their results revealed that there was no significant change in the conductivity up to 15 mol% s-SEBS, but an abrupt increased at about 15 mol% and then gradual increased after 20 mol% [17]. In a different paper, the relationship between the microphase-separated structures and proton conductivities for s-SEBS was studied, and the morphology that styrene blocks with sulfonated groups exhibited a higher proton conductivity, because the styrene blocks formed the matrix phase [15].

On the other hand, phase structure for polymer blend materials is classified into three types (miscible, partially miscible, and immiscible state). Different

5

polymers are not miscible each other in molecular level without especial interaction. Therefore, most of polymer blends exhibit an immiscible state, but there are many cases of polymer blends appearing an miscible state. The system is called the lower critical solution temperature (LCST) and the upper critical solution temperature (UCST). In case of LCST, the system is completely miscible at temperature below LCST and immiscible at temperature upper LCST. By contrast, UCST exhibits the opposite behavior of LCST. For the systems, a miscible and an immiscible state are dominated by temperature and composition.

More than thirty years ago, it was discovered that the blend materials of poly(vinylidene fluoride) (PVDF), crystalline polymer, and poly(methyl methacrylate) (PMMA), amorphous polymer exhibited LCST behavior around 330°C. The blends shows molecular miscible above melting point (T_m), and PVDF crystalizes below the T_m if the blend was maintained above its glass transition temperature (T_g). As a result, microphase separation occurs in the system, and the melting point and crystallinity depression take place because the amorphous polymer exists in the amorphous phase [18-21]. Figure 1-4 shows differential scanning calorimetry (DSC) curves and Figure 1-5 shows T_g and T_m with different PVDF contents of PVDF/PMMA blend films. The solution casting samples were quenched in a liquid nitrogen bath after conditioning at 200°C for 30 min, and the DSC curves as seen Figure 1-4 was obtained. As seen in Figure 1-5, the additivity on T_g was observed in the samples. The result proved that both polymers are miscible at the melt state. In addition, the melting point depression was found to be explicable in terms of thermodynamic mixing of a crystalline polymer with an amorphous polymer [21].
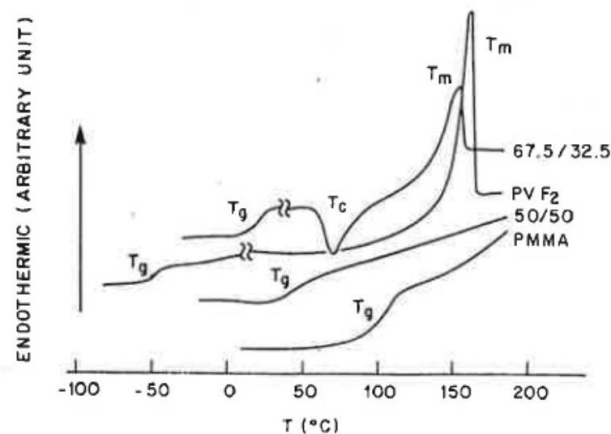
Figure 1-4 Thermograms of quenched samples obtained at the heating rate of 10°C/min.
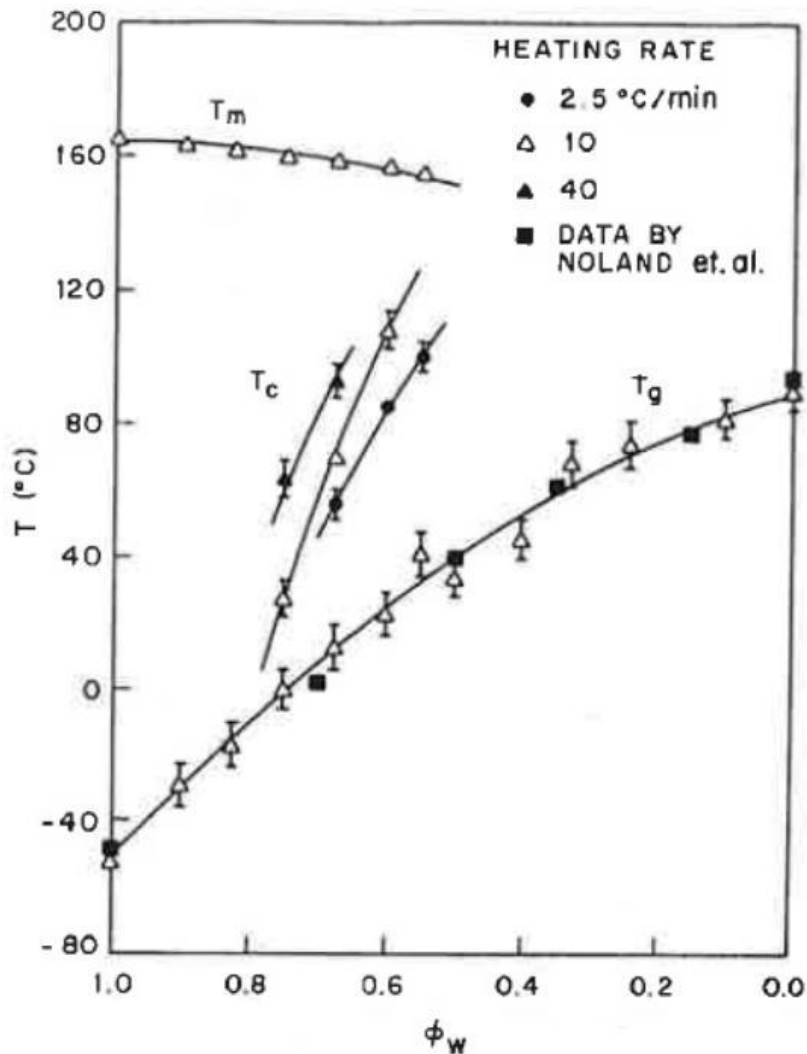
Figure 1 -5 Dependence of glass transition temperature (T_g), crystallization temperature (T_c), and melting temperature (T_m) of the quenched mixture on the weight fraction (φ_w) of PVDF.

It is considered that PVDF is miscible with PMMA because of specific interaction between the fluorine atom acting electron-withdrawing in PVDF and a carbonyl group in PMMA [22-23] In addition, PVDF gives chemical stability and good mechanical properties owing to the strong bonding between carbon and fluorine atoms in the main chain. PVDF does not have absorption in the ultraviolet (UV) region and not deteriorate by the UV. Therefore, PVDF owes not only long-term weatherability, good chemical resistance, and

abrasion resistance but also excellent melt casting processability. However, PVDF shows low adhesive properties to other materials due to low surface tension. For that reason, its improvement is expected by polymer blends, but its improvement is not expected as long as PVDF forms the matrix phase. By contrast, such superior properties of PVDF lose if PVDF forms the domain. Therefore, PVDF/PMMA blend materials are suitable because those improve not only adhesive properties but also maintain superior properties of PVDF. Beside, economic efficiency is expected due to adding PMMA since PVDF is a slightly expensive material, so that there are many reports on PVDF/PMMA blend materials because of both interesting behavior of phase separation but also have a high utilization value for industry.

It is known that PVDF can crystallize into at least four different crystal forms (α, β, γ, and δ) [24]. So far, studies on morphology of PVDF/PMMA blend films clarified the relationship between crystal forms of PVDF and melt casting conditions. Generally, PVDF formed only α phase under cooling from a melt state. However, in the study on the PVDF/PMMA blend material, it was found that β phase was formed under particular cooling speed from a melt state and blend ratio, and annealing condition [25]. In addition, crystallization temperature influenced the structure and the growth mechanism of spherulites, and amount of PMMA entrapped within the interlamellar region in the spherulites was dominated by the growth rate of spherulites [26]. A different paper revealed that the growth rate of PVDF spherulites in PVDF/PMMA blend material was much slower that in pure PVDF. The growth rate of PVDF spherulites in PVDF/PMMA (50/50, wt/wt) blends was a thousand times slower than of pure PVDF spherulites [27]. Investigating on crystallization mechanism of PVDF in PVDF/PMMA blends well explained the reason why crystal structures of PVDF varied owing to different process conditions. On the other hand, in the study on mechanical properties of films prepared a melt casting process, its properties were strongly dominated by PVDF contents and annealing condition [28]. Those studies make us expect that morphology is controlled due to melt casting conditions for PVDF/PMMA blend films.

Since titanium dioxide (TiO$_2$) represents excellent long-term stability under UV light, TiO$_2$ has received the most attention in order to enhance the property of PVDF, recently [29]. Also, PVDF/PMMA/TiO$_2$ blend films own long-term stability because those films have outstanding properties such as mechanical properties, economic efficiency, and adhesive properties to other materials in practical usage [30-31]. For that reason, PVDF/PMMA/TiO$_2$

blend films are promising materials as a protective sheet of a photovoltaic cell in industry, and the film is usually obtained by melt casting process using a T-die, which is widely used in industry to produce flat films. In a T-die method, molten materials are flown from a narrow die gap of the T-die, so that the shear flow field yields. Therefore, it is expected that molecular orientation of PVDF causes anisotropic mechanical properties due to the orientational effect. However, there is limited investigation into the relationship between morphology and polymer processing, although anisotropic properties of films are an important factor in practical usage.

As mentioned above, morphological control is an important aspect in terms of controlling film properties. Therefore we focused on effect of solvents and thermal annealing on the morphology development of a novel block copolymer ionomer, and property-morphology-processing relationship on PVDF/PMMA/TiO$_2$ blend films was studied as a function of TiO$_2$ content and melt casting conditions. Electron microscopy and X-ray scattering were mainly used for the study.

1.2   Thesis Outline

Polymer morphology has strongly related to polymer properties, and it is no exaggeration to say that morphological control is as same as property control. In chapter 2, we synthesized a newly-developed block copolymer ionomer, sulfonated-polystyrene-*b*-fluorinated polyisoprene, which is expected to produce a higher proton conductivity and thermal stability. In this chapter, we attempted to reveal how different kinds of solvents and thermal annealing affect microphase separation and ionic aggregation of the film obtained solution casting method.

In chapter 3, we studied the effects of TiO$_2$ on mechanical properties and morphology of PVDF/PMMA blend films prepared by a melt casting process. Especially, anisotropic mechanical properties and morphology of films with different TiO$_2$ contents was investigated.

In chapter 4, we focused on a morphological study of PVDF/PMMA/TiO$_2$ blend films prepared by a melt casting process in terms of different chill roll temperatures. Furthermore, we discussed on effect of morphology on mechanical properties and deduced the phase structure in the film.

Chapter 5 summarizes morphological development of the block copolymer ionomers, and process-property-structure relationship on PVDF/PMMA/TiO$_2$ blend materials.

1.3 References

[1] Kotaka T, Arai K. J. *Macromol. Sci. Phy.* 1980, B17(2), 303-336

[2] Ward IM. Structure and Properties of Oriented Polymers, Applied Science Publishers, London, 1975

[3] Van Krevelen D. W. Properties of Polymers, Elsevier, Amsterdam-Oxford-New York-Tokyo, 1990

[4] Kanamoto T. Porter RS, *Macromolecules* 1988, 21 470-477

[5] Maruhashi Y. *J. Polym. Eng. and Sci.* 2001, 41, 2194-2199

[6] Khanna YP, *J. Appli. Polym. Sci.* 1990, 40, 569-579

[7] Smith PB, Hsu SL. *J. Appli. Polym. Sci.* 2001, 82 2497-2505

[8] Woodward E, Atlas of Polymer Morphology, Distributed in the United States of America by Oxfrod University Press, New York and in Canada by Oxford Press, Canada

[9] Helfand E. *Macromolecules* 1975, 8, 552-556

[10] Leibler L. *Macromolecules* 1980, 13, 1602-1617

[11] Fredrickson GH. *Macromolecules* 1898, 22, 1238-1250

[12] Maten MW. *Eur. Phys. J. E.* 2006, 21, 199-207

[13] Bates FS, *Fredricson GH. Annu. Rev. Phys. Chem.* 1990, 41, 525-557

[14] Funaki Y, Hashimoto T. *Polymer* 1999, 40, 7147-7156

[15] Kim B, Jung B. *J. Membrane Sci.* 2005, 250, 175-182

[16] Won J, *Macromolecules* 2003, 36, 3228-3234

[17] Kim J, Jung B. *J. Membrane Sci.* 2002, 27, 129-137

[18] Paul DR, Polymer Blends, vol. 1, Chap. 2, Academic Press, New York, 1978

[19] Noland JS. Adv. Chem. Ser. 1971, 99, 15-28

[20] Bernstein RE. *Macromolecules* 1977, 10, 681-686

[21] Nishi T, Wang TT. *Macromolecules* 1975, 8, 909-915

[22] Saito H, Inoue T. *Macromolecules* 1991, 24. 4446-4449

[23] Leonard C, Halary L. *Polymer* 1985, 26, 1507-1513

[24] Tashiro K. *Ferroelectrics* 1981, 32, 167-175

[25] Horibe H. *J. Electrochem. Soc.* 2006, 153, G119-G124

[26] Okabe Y, Saito H. *Polymer* 2010, 51, 1494-1500

[27] Wang TT, Nishi T. *Macromolecules* 1977, 10, 421-425

[28] Mijovic J, Han CD. *Polym. Eng. Sci.* 1982, 22, 234-240

[29] Cao X, Ma J. *J. Applied Surface Sci.* 2006, 253, 2003-2010

[30] Li W, Zhang LM. *J. Mater. Sci.* 2009, 44, 2977-2984

[31] Lee JG, Kim SH. *Macromolecular Research* 2011, 19, 72-78

Chapter 2.

Effect of solvents and thermal annealing on the morphology development of a novel block copolymer ionomer

2.1 Introduction

Fuel cells have been considered to be one of the most promising electric power sources. Power is generated by the chemical reaction between hydrogen and oxygen. The proton exchange membrane for fuel cells (PEMFC) has a high possibility for portable electrical device usage, such as transportable applications, and some stationary applications in the near future. The direct methanol fuel cell (DMFC), which directly delivers methanol to the anode side, is a kind of PEMFC, and further development is expected, because DMFC is more compact and lighter due to the production systems of hydrogen being unnecessary. The membranes for PEMFC are required to have higher proton conductivities for practical usage. So far, many researchers have worked on the transmission properties and nano- or micro scale membrane structures [1-3].

Nafion (DuPont, Wilmington, DE, USA) is one of the perfluorinated ionomers and widely used in industry because of its high proton conductivity, superior mechanical properties and oxidative stability. It has been suggested that Nafion has ionic clusters, due to the existence of ion exchange sites, whose size and shape have been clarified by using X-ray scattering techniques [4-7]. It is reported that the conductivity of the Nafion membrane is proportional to the size of the ionic aggregation and water uptake [7]. However, Nafion is very expensive, and has limitations in applications requiring temperature in excess of 100ºC because of its lack of heat resistance. Therefore, membrane materials with economic efficiency and a higher heat resistance are more desirable within industry.

In this context, block copolymer ionomers are promising candidates as a substitutable membrane material. According to the mean-field theory, block copolymers develop various equilibrium morphologies, such as spheres, cylinders and lamellae. Such microphase structures might make the proton conductivity higher if sulfonic groups in block copolymers connect to both sides of the membrane. Many of the studies on block copolymer ionomers have

reported on the relationship between microphase-separated morphologies and transmission properties [3]. In particular, shape and size of the ionic aggregation within microdomains strongly influence the proton conductivity or methanol permeability [4]. Other studies have shown better proton conductivity by the sulfonated cross-linked poly(styrene-*b*-butadiene-*b*-styrene) (scSBS) membrane when compared with Nafion. They ascribed it to the presence of the proton transport channels [2]. For the sulfonated styrene-ethylene copolymer, the presence of a bicontinuous network of hydrophilic and hydrophobic domains in water-swollen samples was suggested by X-ray and neutron scattering [8]. Also, it has been suggested that microphase structures are closely related to mechanical properties, which are worthy of practical use [9]. Block copolymer ionomers, such as sulfonated poly(styrene-*b*-(ethylene-r-butylene)-*b*-styrene) (sSEBS), sulfonated poly(styrene-*b*-isobutylene-*b*-styrene) (PS-PIB-PS) and sulfonated poly(styrene-*b*-ethylene, have been investigated as substitutions for Nafion, because those kinds of block copolymers are derived from economical block copolymers such as SEBS or PS-PIB-PI.

A statistical thermodynamic theory on block copolymers called the strong segregation limit (SSL) theory, developed by Meier and Helfand and Wasserman, gives equilibrium morphology minimizing the free energy of microdomains [10-14]. Equilibrium morphologies such as spheres, cylinders, lamellae and disordered structures, are predicted by both χN and volume fraction of each block, where χ is the Flory-Huggins interaction parameter and N is the degree of polymerization. Morphological change does not occur under any given composition, except for order-disorder transition. By contrast, the weak segregation limit (WSL) theory developed by Leibler [15], Fredrickson and Helfand [16] and Frederickson and Leibler [17], predicts morphological change with temperature at a fixed volume fraction of block copolymers and also considers the composition fluctuation. Ohta and Kawasaki generalized the WSL to the SSL by taking into account a long-range interaction of the local monomer concentration deviation by the Ginzburg-Landau type mean-field theory [18]. Recently, the self-consistent field theory (SCFT) suggested by Matsen and Bates describes the crossover from the WSL theory to the SSL theory [19-23]. All of those theories let us predict equilibrium morphology of block copolymers.

In practical cases, nonequilibrium morphology is often formed in the films by the evaporation rate of solvents, which is known as the solvent effect. The morphology of the films prepared using the solvent-casting method strongly

depends on the solvent used in experiments. The solvent effect can be explained by the effective volume which resulted from the polymer-solvent interactions in the polymer solution [24]. It was reported that the evaporation rate of the solvent and the thermal annealing process influences the evolution of morphologies in the PS-PIB-PS [9]. Additionally, it is commonly known that initially formed morphology changes into more stable morphology with thermal annealing above glass transition temperature (T_g). However, in the case of block copolymer ionomers, morphological studies should consider not only a microphase structure, but also the effect of ionic aggregation.

Weiss, and Lu and Weiss, reported the ionic aggregation in block copolymer ionomers [25-29]. One report revealed the effect of the temperature history on the ionic cluster in the sulfonated PS ionomers with Na^+ and Zn^{2+} salts, by small angle x-ray scattering (SAXS). In a different paper, they suggested that partially sulfonated SEBS triblock copolymers possess a three phase microstructure, which is an ionic cluster within polystyrene domains, PS domains and poly(ethylene-co-butylene) matrix. They have also reported an ionic aggregate dissociation temperature, Td, which was determined from a function of temperature by time-resolved SAXS on the partially sulfonated SEBS block copolymer ionomers.

As mentioned above, although Nafion is the most well-known membrane for fuel cells improvement with regards to heat resistance, membrane economics are required. Therefore, we synthesized a new type of block copolymer, sulfonated PS-*b*-fluorinated polyisoprene (s-PS-*b*-f-PI). Fluorination is expected to produce a higher T_g due to hydrophobic and mechanically stiffened properties, which are useful for application in high temperatures. Sulfonation makes proton conductivity higher, as already reported by many researchers. Thus, the experimental results of the new material are very interesting and significant not only for academics, but also for industry. In this paper, we focused on morphological developments caused by microphase separation and ionic aggregation, in terms of functions of different kinds of solvents and thermal annealing by using not only transmission electron microscopy (TEM, JEOL Ltd, Japan), small angle x-ray scattering (SAXS, Rigaku Corporation, Japan) but also intermediate angle x-ray diffraction (IMAXD, Rigaku Corporation, Japan). The solubility parameters and the Bjerrum length were applied to discuss the solvent effect.

2.2 Experimental

2.2.1 Synthesis

Sulfonated polystyrene-*block*-fluorinated polyisoprene as an acid form was derived from a PS-*b*-PI precursor, which was synthesized by anionic polymerization. The precursor was first fluorinated at 180ºC in cyclohexane, by using hexafluoropropylene oxide. Next, sulfonation was conducted in dichloroethane by acetic sulfate, which is formed from a mixture of acetic anhydrous and sulfonic acid. This sample will be referred to as sH-PS-*b*-f-PI hereafter. In addition, the block copolymer ionomer was neutralized into a cesium salt form. This sample will be referred to as sCs-PS-*b*-f-PI hereafter. The synthesis conditions are shown briefly in Scheme 2-1. The molecular characteristics such as molecular weight, the degree of fluorination and sulfonation, were determined by ^{1}H NMR, gel permeation chromatography (GPC) and elemental analysis. The degree of sulfonation and fluorination was 30 mol% and >98 mol%, respectively, for both of the block copolymer ionomers. In order to determine the volume fraction of each block unit, the density was measured in the mixed solvent of carbon tetrachloride (1.594g/ml) and cyclohexane (0.779 g ml^{-1}). The film for measurement of the density was dried up in a vacuum oven for 24 h before the film was put into the mixed solvent. The density of the sH-PS-*b*-f-PI was found to be 1.2902 g cm^{-3} and that of the sCs-PS-*b*-f-PI was found to be 1.3423 g cm^{-3}. The density of f-PI was directly measured by using the synthesized homopolymer and found to be 1.262 g cm^{-3}. Based on the overall density, the density of the f-PI, the weight fraction of the block copolymer ionomers and the volume fractions of each block component, were calculated. The molecular characteristics are given in Table 2-1.

2.2.2 Sample preparation

The sH-PS-*b*-f-PI samples were dissolved in anhydrous tetrahydrofuran (THF) at a concentration of 3 wt% and were cast into Teflon Petri dishes. The dishes were covered with a glass hood in order to slow the evaporation rate, and it was took 3 days to evaporate the solvent at room temperature. After evaporating the solvent, vacuum drying at room temperature for 24 h was employed to expel the residual solvents in the film. Finally, the dried film was peeled off the dish, and the unannealed film was obtained. For the examination of the annealing effect, the films were annealed at 120ºC under

the vacuum condition.

In order to study the existence of ionic clusters, the sCs-PS-*b*-f-PI film was prepared. We attempted to obtain solution casting film using anhydrous THF, but we could not dissolve this sample. This was probably due to it having a lower solubility caused by cesium salts. A THF/water mixture (98/2 wt/wt) and dimethylsulfoxide (DMSO) were used to obtain the solution casting film. Similar to the first experiment, 3 wt% polymer solution was prepared and cast into Teflon Petri dishes. The dishes were put under vacuum conditions for 24 h at room temperature. After that, the thermal annealing at 140ºC was employed. The solution casting film obtained from DMSO was dried at 60ºC under vacuum conditions, before annealing, because the evaporation rate of the solvent was very slow under ambient conditions, due to its high vapor pressure itself.

2.2.3　Morphological Characterization

The morphology of the films was observed by TEM. All samples were cut across the thickness of the film using a Leica Ultracut UCT cryomicrotome, at −110ºC and −60ºC for unannealed and annealed films, respectively. These were then collected on copper grids and stained with RuO_4 vapor for 1 h. It is assumed that only the sulfonated PS blocks were stained because of oxidization of the aromatic ring. The thickness of the thin sections was approximately 40−60 nm. TEM images were obtained using an A JEOL 100CX microscope, operating at an accelerating voltage of 100 kV in the bright field mode.

SAXS measurements were conducted with an apparatus consisting of a rotating-anode X-ray generator, with a three-slit collimator, a vacuum path for incident and scattered beams. A measurement of 1195 mm of the camera length was calculated by silver behenate. IMAXD was carried out by a Rigaku RU-H3R rotating anode X-ray diffractometer at 40 kV and 200 mA. The camera length, calculated by tricosan, was approximately 233 mm. The wavelength of the X-rays used in both the SAXS and the IMAXD was 1.54 Å. Scattering patterns obtained from both measurements were acquired with 10 × 15 cm² Fuji BAS-2500 ST-VA image plates and were read with a Fiji BAS-2500 image plate scanner.

2.3 Results and Discussion

2.3.1 Morphological study on sulfonated polystyrene-*block*-fluorinated polyisoprene with an acid form (sH-PS-*b*-f-PI)

Figure 2-1(A) and (B) show the TEM micrographs of the sH-PS-*b*-f-PI films cast from anhydrous THF. The left side is the image of the unannealed film, and the right side is that of the annealed film at 120℃ for 168 h. The dark phase represents the sulfonated PS (sH-PS) matrix, since RuO_4 stains the aromatic ring in the PS blocks. The bright phase represents the f-PI of the cylindrical microdomains. The TEM image showed the well-ordered honeycomb-like cylindrical morphology in the unannealed film, and the well-ordered morphology changed into the no-long range order structure, through the annealing, which is a wormlike cylindrical morphology.

The corresponding SAXS profiles are presented in Figure 2-2. For the unannealed film, the relative peak positions were observed with the ratio of 1, √3, √4, √7, √9 and √12. Their peaks correspond to the Bragg diffraction of (1 0), (1 1), (2 0), (2 1), (3 0) and (2 2) planes, respectively. Those values of the peaks indicate a typically cylindrical morphology, and the result by SAXS was consistent with the TEM image of the unannealed film. The d-spacing can be calculated by equation (1) and (2):

$$q = \frac{4\pi}{\lambda} \sin\theta \tag{1}$$

$$d = \frac{2\pi}{q} \tag{2}$$

where q is the scattering vector, d is the Bragg spacing, which means the center-to-center distance (d-spacing) of block copolymer domains. The d-spacing calculated from the first order peak of the unannealed film was 25.2 nm. From hexagonally packed geometry, the average distance between two cylinders is represented by 2d/√3; it was calculated to be 29.1nm. From Figure 2-2, it was found that the higher ordered peaks completely disappeared through thermal annealing. This means that the well-ordered morphology changed to the no-long range ordered morphology by thermal annealing, as seen in the TEM image.

In this experiment, the microdomains of the f-PI blocks and the continuous

phase of the sH-PS matrix were observed. It should be noticed that the sH-PS blocks of 21.4 vol% formed the continuous phase of the matrix and f-PI of 78.6 vol% formed the discontinuous phase of the cylindrical domains. Equilibrium morphology was predicted by a volume faction of each block component and χN, as mentioned in the introduction. The χ of PS-PI diblock copolymer, which is a precursor of the sH-PS-b-f-PI under any temperatures, is calculated by equation (3) [30]. According to the SSL theory, the volume fraction between 0.17 and 0.28 of one component in diblock copolymers and χN>10 should form cylindrical morphology, because it makes minimizes free energy in each polymer chain [31]. The SCFT predicts either equilibrium cylinders or spheres if χN>10.

$$\chi = -0.0258 + 27.9/T \tag{3}$$

Equation (3) gave 19.3 of the χN at 25°C. The χN of PS-PI is different from the sH-PS-b-f-PI, but sulfonation and fluorination will make χ larger due to the chemical characteristics. The χ value of the sH-PS-b-f-PI predicts an ordered cylindrical morphology in the continuous f-PI phase. However, the morphology was completely reversed to morphologies predicted by the SSL, the WSL and the SCFT [10,14,17,21,23].

Morphological change of the SEBS is due to residual solvents that cause morphological transition selectivity during the membrane formation. For the 27 mol% sulfonated SEBS, the morphology transformed from the lamellar to a disordered structure with the increasing concentration of methyl alcohol (MeOH) in THF/MeOH solvent. This is because the residual MeOH that exists due to the lower vapor pressure swells the sPS selectively during the last evaporation stage. Namely, MeOH caused a disorderly interconnected nature of the morphological transition [1]. Various morphologies of poly(2-vinylpridine)-b-PI, developed by the solution casting method from different solvents, are reasonably explained by the difference of Hansen's solubility parameters between solvents and each block polymers. It was suggested that microphase-separated structures were already formed in the solution and nonequilibrium morphology were developed in the dried films. The development of various structures such as spheres, cylinders and lamellae, are due to the preferential affinity of the solvents to each block. It was also revealed that the nonequilibrium structure developed from the various solvents was maintained in the as-cast and even the annealed film under particular temperature and times [10]. Therefore, it is expected that

17

the reversal morphology obtained in our experiment should be explained by the solvent effect. Hensen's solubility parameter is mentioned by equation (4):

$$\delta^2{}_H = \delta^2{}_d + \delta^2{}_p + \delta^2{}_h \tag{4}$$

where δ_d is dispersive and δ_p is permanent dipole-dipole interaction and δ_h is hydrogen bonding forces. Table 2-2 shows Hansen's solubility parameter of THF, PS and PI [34, 35]. The solubility parameters of THF, PS and PI are 19.5, 18.6 and 16.6 Mpa$^{1/2}$, respectively. When comparing the solubility parameter differences between solvents and each block, the influence of sulfonation and fluorination should be considered. It is generally expected that sulfonation makes the solubility parameter larger because it causes strong interaction between the polymer chains, due to sulfonic groups having strong dipole. By contrast, it is estimated that fluorination makes the solubility parameter smaller. As a result, the solubility parameter of the partially sulfonated PS will probably be >18.6 MPa$^{1/2}$ and closed to THF. Therefore, THF was expected to be good solvent for the sH-PS, and the sH-PS blocks might form a continuous phase due to the rather extended polymer chains in the polymer solution. In contrast, the f-PI blocks make the polymer chains attractive in the solution. Based on the discussion, it was interpreted that the effective volume fraction of the f-PI of 78.6 vol% is much smaller in THF and that that of the sH-PS becomes much larger than the calculated volume fraction of THF, if the sH-PS-*b*-f-PI behaves like an uncharged block copolymer.

The effect of charge groups in the polymer chains in solutions is described by the Bjerrum length [32, 33]. It is known that the Bjerrum length, at which distance two unit charges have an interaction energy $\pm K_B T$, provides a measure of the strength of electrostatic energy. A shorter Bjerrum length means a weak interaction between two charges. Also, the same charges such as positive-positive or negative-negative cannot get close to each other within the Bjerrum length. The Bjerrum length was defined by equation (5).

$$l_B = \frac{e^2}{4\pi\varepsilon\varepsilon_0 K_B T} \tag{5}$$

In the equation, l_B is the Bjerrum length, and e is the electron charge, and ε is the dielectric constant of the solvent in a polymer solution. The following, $1/(4\pi\varepsilon_0)$, is the Coulomb force constant, and the value is $8.988 * 10^9$ Nm^{-2}C^{-2}. K_B is the Boltzmann constant, and the value is $1.38 * 10^{-23}$ m^2 kgs^{-2} K^{-1}. Table 2-3

shows both the dielectric constant and the Bjerrum length. As seen in Table 2-3, the Bjerrum length of THF was 7.5 nm. This value was approximately 10× that of water. This means that the interactions between two charges in the sH-PS-*b*-f-PI in THF are much stronger than those in water. It is assumed that the dissociation of charges of the sulfonic groups in THF is difficult. For that reason, the sH-PS chains can behave like uncharged block copolymers and extend fully, due to the affinity in the solvent in terms of its solubility parameter. As a result, we end up with the effective volume in the continuous phase of the sH-PS. The well-ordered cylindrical morphology in the film cast from anhydrous THF, is explained based on the solubility parameter and the Bjerrum length.

As stated above, the well-ordered morphology changed to the no-long range ordered morphology through thermal annealing. Hence, invariant Q, which gives useful information about an interface for a two-phase system, was calculated. The invariant Q is related to the hindrance and promotion of microphase separation and can be calculated by the following equation:

$$Q = \frac{1}{2\pi} \int I(q) \, q^2 \, dq \qquad (6)$$

where q is the scattering vector and $I(q)$ is the scattering intensity at the scattering vector q. Figure 2-3 shows that the invariant Q rapidly decreased during the first 24 h of the thermal annealing and equilibrated to some extent. Generally, the decrease of the invariant Q, means hindrance of microphase separation with thicker interfacial region. From this result, it was estimated that the microphase separation was impeded by thermal annealing. Annealing above T_g, facilitates formation of a more ordered morphology, by minimizing free energy on each chain. From the equation (3), at 120°C, the calculated χN of the PS-*b*-PI, which is the precursor of the sH-PS-*b*-f-PI, was 12.8. However, actual χN is larger than the calculated value, due to sulfonation and fluorination. Thus, a more ordered morphology was expected by annealing, based on the mean-field theory. The previous study on the PS-*b*-poly(butadiene)-PS block copolymer (SBS), with PS of 53 vol%, reported the nonequilibrium cylindrical morphology formed from methyl ethyl ketone (MEK), which is a selective solvent, i.e., good for PS chains but not for PB chains. The morphology was transformed into the equilibrium lamella from the cylinder, by thermal annealing. This morphological change was predicted by SCFT [36]. In other reports, the PS-PI block copolymer, with PS of 16 wt%,

formed the ordered cylindrical morphology at 150ºC and changed into the ordered sphere morphology at 200ºC [30]. Therefore, it is considered that our results are very different from the usual behavior of uncharged diblock copolymers. This might be due to ionic cluster formation.

According to the recent papers, ionic clusters are scattered at the values of the scattering vector, q, from 1.0 to 2.0 nm^{-1}. This corresponds to the Bragg spacing from 3.1 nm to 6.3 nm [25,26]. However, the ionic clusters in the sH-PS-*b*-f-PI film were not detected by IMAXD. This is because the electron density difference between the clusters and the surrounding media is very small, as reported by Fujimura [5]. In order to examine ionic clusters, the sCs-PS-*b*-f-PI films were subjected to IMAXD.

2.3.2 Microphase-separated structure and ionic cluster formation on sulfonated polystyrene-block-fluorinated polyisoprene with a cesium neutralized form (sCs-PS-*b*-f-PI)

The mixed solvent of THF/Water (98/2, wt/wt) was used for solution casting films of the sCs-PS-*b*-f-PI. Figure 2-4 shows TEM images of both the unannealed film and the annealed film at 140ºC and 168 h. The reason of having 140ºC as the annealing temperature is that it is favorable when compared with 120ºC in terms of increasing the chain mobility causing ionic aggregation. Another reason is for making up for the reduction of the mobility of the polymer chains due to cesium salts. The disordered morphology of the f-PI matrix was observed in both the images. The microphase-separated structure was a completely reversal to that of the sH-PS-*b*-f-PI film cast from anhydrous THF. Figure 2-5 shows the time resolved SAXS profiles of the film. There is only one peak at around 0.035 Å^{-1} of the q value. The SAXS profiles were consistent with the TEM images and confirmed the disordered morphology for both the unannealed and the annealed film. It was hard to see the change of the peak position and the broadening with the lapse of the thermal annealing time.

Several studies on ionic aggregation have been reported by R.A.Weiss, and scattering peak positions attributed to ionic clusters were mentioned. One of the studies investigated the morphologies and mechanical properties of the block copolymer ionomer based on the lightly sulfonated SEBS triblock copolymer with zinc salt of approximately 10%. According to the report, 3-4 nm ionic clusters within 20-30 nm polystyrene domains in a rubbery continuous phase were suggested. The q value associated with the ionic

clusters was seen at around 0.15 Å^{-1} [26].

Figure 2-6 shows the time resolved IMAXD profiles of the film cast from THF/Water (98/2, wt/wt). The unannealed film exhibited one small peak at around 0.35 Å^{-1} of the q value. This peak can be attributed to ionic clusters dispersing within the sCs-PS blocks. In our experiment, the q value associated with the ionic aggregation was larger than q values mentioned in the previous reports. This is because the higher sulfonation level of 30% cesium salts causes the smaller d-spacing compared with previous reports [5,26,29]. From equation (2), the cluster d-spacing attributed to the ionic aggregation was calculated to be 1.77 nm at the unannealed film, and the d-spacing was hardly changed by thermal annealing. From Figures 2-4 – 2-6, we can see that there were no significant changes caused by thermal annealing for both the microphase-separated structure and the ionic aggregation. It was considered that the stable structure was developed by the ionic cluster formation in the unannealed film. The disordered morphology and the ionic cluster formation were observed in the sCs-PS-b-f-PI film by adding a small amount of water. It was found that water affects the sulfonic groups selectively and helped the ionic aggregation. However, the morphological change due to the ionic cluster formation induced by thermal annealing was not revealed.

Through various experiments, DMSO was found to completely dissolve the block copolymer ionomer. The TEM images for the unannealed and the annealed film cast from DMSO are shown in Figure 7. As seen in the images, both films showed distinct lamellar morphology. In particular, the thin parts seen in the annealed film support the lamella, because of the twist itself. The lamellar morphology indicates that the effective volume fraction of the sCs-PS blocks is nearly equal to that of the f-PI blocks. Figure 2-8 shows the time-resolved SAXS profiles with thermal annealing. The relative peak positions of 2, 3 to the first order peak denote lamella morphology which is consistent with the TEM images.

The morphology was discussed with regards to the solubility parameter and the Bjerrum length. The solubility parameter of DMSO is 26.7 as seen in Table 2-2. This value is much different from both the sCs-PS and the f-PI. Therefore, it is expected that both the sCs-PS and the f-PI chain should be as attractive as possible to the solvent. On the other hand, the Bjerrum length of DMSO is 1.1 nm, as seen in Table 2-3. The value is quite low and similar to that of water. Therefore, it is estimated that SO_3Cs will easily be dissociated with SO_3^- and H^+ in DMSO, because of the weak interaction between the neighboring charges. The average distance between the sulfonic groups was

calculated, in order to estimate the chain conformation in the polymer solution. For calculation purposes, 1.53 Å of the length between two carbons and 112° of the bond angle between skeletal carbons in polymers were applied [37]. The distance between two aromatic rings can be calculated by $2 \times 1.53\cos(180° - 112°)$. As a result, 0.116 nm was calculated as the length between two aromatic rings. The average distance between sulfonic groups in the sCs-PS-*b*-f-PI should be 0.34 nm, since the degree of sulfonation is 30%. The Bjerrum length of 1.1 nm is larger than the average distance between sulfonic groups. Therefore, it was estimated that SO_3^- existing in isolation repel each other in the block copolymer ionomer. As a consequence, the sCs-PS chains should be extended in DMSO, and the formation of the ionic aggregation becomes difficult. The stretched sCs-PS chains using the Bjerrum length and the attractive f-PI chains using the solubility parameters, explain the lamellar morphology.

Figure 2-9 shows the IMAXD profiles exhibiting the thermal annealing effect on the film cast from DMSO. One small peak at around 0.327 Å^{-1} of q value was observed in the unannealed film. This small peak can be attributed to the ionic clusters dispersing within the lamellar phase of the sCs-PS and supports the validity of the interpretation based on the Bjerrum length. From equation (2), the average d-spacing between the clusters in the unannealed film was calculated to be 1.94 nm. It was clearly observed that the peak intensity rapidly increased by the lapse of thermal annealing time, and the d-spacing changed to 1.79 nm.

Comparison of the scattering peak area of the films cast from THF/Water (98/2, wt/wt) and DMSO is feasible, because the thickness of the two kinds of the films was nearly the same. Figure 2-10 clearly shows that the peak areas for both films are almost saturated within 24h of thermal annealing and reached almost the same values. This means that the cluster formation took place within 24 h in the sCs-PS phase in both cases.

The d-spacing ascribed to the ionic clusters was calculated and shown in Figure 2-11. The d-spacing of the clusters in the film cast from DMSO changed from 1.94 Å to 1.79 Å through annealing. By contrast, there was no significant change in the d-spacing in the film cast from the mixed solvent of THF/Water (98/2, wt/wt) through annealing (1.77 Å–1.74 Å). The reduction of the d-spacing with the increase of the annealing time indicates the promotion of the ionic cluster formation. This was consistent with the results obtained from IMAXD, and thermal annealing promoted newly-developed ionic aggregation in the film cast from DMSO.

As seen in Figure 2-8, the first and the second order peaks became slightly broader with the lapse in the annealing time. It was suggested that the broadening of the scattering peak is the result of the ionic aggregation, which enhances the electron density fluctuations in the sulfonated PS microdomains [28]. Thus, the peak broadening seen in our experiment by annealing can also be ascribed to the formation of the ionic clusters. The result is consistent with the promotion of the ionic cluster formation as seen in Figure 2-9. Also as can be seen in Figure 2-8, the relative peak position of 3 to the first order peak appeared clearly. This denotes the increase of the periodicity of the lamellar morphology. By contrast, the d-spacing in the unannealed and the annealed film for 168 h was 25.6 nm and 27.3 nm, respectively. For the mean-field theory, free energy per chain is proportional to $D^2/(a^2N)$, where D is a domain period, a is a characteristic segment, and N is the degree of polymerization [31]. This means that the increase of d-spacing increases the free energy in each chain in the lamella. From the results, it was indicated that the ionic cluster formation and the microphase separation simultaneously occurred at the film cast from DMSO. In the case of the sH-PS-*b*-f-PI, the morphology changed to the no-long range ordered structure, as mentioned above, and the reason was assumed to be the ionic aggregation. However, the hindrance of the microphase separation by the promotion of the ionic cluster formation was not confirmed in the sCs-PS-*b*-f-PI film cast from DMSO.

According to Weiss et al., the sulfonated SEBS with cesium salts showed a more thermally stable ionic cluster compared with the acid form and the zinc salts. They have suggested that the alkali-metal salts may have tighter packing of ionic species in the aggregation because of stronger interactions between the ion pairs. As a result, a dissociation transition of an ionic aggregation in the sulfonated SEBS with acid form (sH-SEBS) and the sulfonated SEBS with zinc salts (sZn-SEBS) was observed around 200°C. By contrast, the alkali-metal-neutralized ionomers with Na salts (sNa-SEBS) and those with Cs salts (sCs-SEBS) were thermally stable to at least 300℃. The strength of the ionic interaction is $Na^+ > Zn^+ > H^+$. Furthermore, the ionic aggregation impeded the diffusion of the block segment, and the extent of the block microphase separation decreased with the increase of sulfonation level and the strength of the ionic interaction. It is also mentioned that the ionomer blocks in the sNa-SEBS have poor mobility, even in solution compared with the sZn-SEBS [28, 29]. Those previous reports support that the ionic aggregation in the sCs-PS-*b*-f-PI film cast from THF/Water and DMSO is stable under the thermal annealing at 140°C.

On Careful study of the TEM image of the annealed film in Figure 2-7, dis-ordered parts were observed; the morphology was similar to that cast from the mixed solvent of THF/Water (98/2, wt/wt). Additionally, Figure 2-8 denoted that the third order peak started to get slightly broader at $140^{\circ}C-168$ h. This strongly indicates initiation of a morphological change. The higher annealing temperature, or the longer annealing time, might induce order-disorder transition. Therefore, the morphological behavior and the ionic cluster formation by thermal annealing in the film cast from DMSO might be dominated due to the poor mobility of the sCs-PS blocks compared with the sH-PS blocks. Additionally, the difference in the stability of the unannealed film might be the reason, because lamellar morphology is more stable than cylindrical morphology in terms of the volume fraction for the s-PS-*b*-f-PI. Future studies are planned to identify this assertion on morphological changes, and to investigate the relationship between proton conductivity and morphologies.

2.4 Conclusion

The sH-PS-*b*-f-PI film cast from anhydrous THF had a well-ordered cylindrical morphology. The morphology was explained by the solubility parameters and the Bjerrum length. It was estimated that the solubility parameter of the partially sulfonated PS was close to anhydrous THF and the polymer chains were extended in the solution. However, the f-PI chains became more attractive, because of the large difference in the solubility parameter. From the Bjerrum length data, it is expected that the sH-PS chains behave like uncharged block polymers. As a result, the effective volume fraction of the f-PI, although its calculated volume fraction is 78.6%, is actually much smaller in the anhydrous THF, whereas that of the sH-PS became much larger than the calculated volume fraction. The well-ordered morphology changed to the no-long range ordered structure through thermal annealing at 120°C. This behavior was very different from the usual behavior of uncharged diblock copolymers and was presumed to be due to the ionic cluster formation.

The sCs-PS-*b*-f-PI film cast from the mixed solvent of THF/Water (98/2, wt/wt) had a disordered morphology, and the ionic cluster formations occurred within the sCs-PS blocks. After annealing at 140°C, there was no significant change in both the microphased-separated structure and the ionic cluster formation. It was considered that adding a small amount of water added to THF helped the ionic cluster formation and induced stable structure.

In the case of using DMSO as a solvent, the lamellar morphology was developed. Attractive polymer chains for both the sCs-PS blocks and the f-PI blocks were estimated in terms of the difference in the solubility parameters between each block and DMSO. However, the Bjerrum length of 1.1 nm indicates the extended chain conformation of the sCs-PS blocks, due to the repellence between SO_3^- caused by easy dissociation of SO_3Cs. As a result, almost the same effective volume fraction of the sCs-PS and the f-PI was conceivable. A small amount of ionic aggregation in the unannealed film supported the validity of the interpretation of the Bjerrum length. With thermal annealing at 140°C, the rapid promotion of ionic aggregation and the periodicity of the lamellar morphology were observed simultaneously. However, the distinct hindrance of the microphase separation by the ionic cluster formation was not confirmed. This could attribute to the poorer mobility of the sCs-PS blocks compared with the sH-PS blocks and the better stability of lamellar morphology compared with cylindrical morphology in the

unannealed film.

2.5 References

[1] Kim J, Kim B. *J. Membr. Sci.* 2002, 207, 129-137

[2] Won J. *Macromolecules* 2003, 36, 3228-3234

[3] Kim B. *J. Membr. Sci.* 2005, 250, 175-182

[4] Gierke TD. *J. Polym. Sci.* 1981, 19, 1687-1704

[5] Fujimura M, Hashimoto T. *Macromolecules* 1981, 14, 1309-1315

[6] Gebel G. *Macromolecules* 1997, 30, 7914-7920

[7] Lin H-L. *J. Polym. Sci. Part B* 2005, B43, 3044-3057

[8] Serpico JM. *Macromolecules* 2002, 35, 5916-5921

[9] Crawford DM, Gido SP. *Thermochim. Acta* 2001, 367-368, 125-134

[10] Meier DJ. *J. Polym. Sci. Part C* 1969, 26, 81-98

[11] Helfand E, Wasserman ZR. *Macromolecules* 1975, 8, 552-556

[12] Helfand E, Wasserman ZR, *Macromolecules* 1976, 9, 879-888

[13] Helfand E, Wasserman ZR, *Macromolecules* 1978, 11, 960-966

[14] Helfand E, Wasserman ZR, *Macromolecules* 1980, 13, 994-998

[15] Leibler L. *Macromolecules* 1980, 13, 1602-1617

[16] Fredrickson GH, Helfand E. *J. Chem. Phys.* 1987, 87, 697-705

[17] Fredrickson GH, Leibler L. *Macromolecules* 1898, 22, 1238-1250

[18] Ohta T, Kawasaki K. *Macromolecules* 1986, 19, 2621-2632

[19] Matsen MW, Bates FS. *Macromolecules Rev.* 1996, 29, 1091-1098

[20] Matsen MW, Bates FS. *J. Chem. Phys.* 1997, 106, 2436-2448

[21] Matsen MW. *Eur. Phys. J. E.* 2006, 21, 199-207

[22] Matsen MW. *Eur. Phys. J. E.* 2009, 30, 361-369

[23] Matsen MW. *Eur. Phys. J. E.* 2010, 33, 297-306

[24] Funaki Y, Hashimoto T. *Polymer* 1999, 40, 7147-7156

[25] Weiss RA. *Polymer* 1986, 27, 3-10

[26] Weiss RA. *Polymer* 1991, 32, 2785-2792

[27] Lu X, Weiss RA. *Macromolecules* 1993, 26, 5876-5884

[28] Lu X, Weiss RA. *Macromolecules* 1993, 26, 6525-6530

[29] Lu X, Weiss RA. *Macromolecules* 1995, 28, 2831-2839

[30] Sakurai S, Hashimoto T. *Macromolecules* 1993, 26, 5796-5802

[31] Bates FS, Fredrickson GH. *Annu. Rev. Phys. Chem.* 1990, 41, 525-557

[32] Yin D, Pablo JJ. *J. Chem. Phys.* 2005, 123, 174909:01-174909:09

[33] Kong CY, Muthukumar M. *J. Chem. Phys.* 1998, 109, 1522-1527

[34] Hansen CM. *Hansen Solubility Parameters,* CRC Press: New York, 2000

[35] Hansen CM, Skarrup K. *J. Paint Tech.* 1967, 39, 511

[36] Sakurai S, Umeda H. *J. Chem. Phys.* 1996, 105, 8902-8908

[37] Yoon DY, Flory PJ. *Macromolecules* 1975, 8, 776-783

Table 2-1 Molecular characteristics of s-PS-*b*-f-PI diblock copolymer ionomers.						
Sample	Mw (g/mol)	Mw/Mn	Degree of sulfonation (%)	Degree of fluorination (%)	%PS (w/w)	%PS (v/v)
PS-*b*-PI	23,600	1.01	0	0	21	18.7
PS-*b*-fluorinated PI	31,700	1.05	0	>98	14	16.4
sH-PS-*b*-f-PI[a)]	—	—	30	>98	23	21.4
sCs-PS-*b*-f-PI[b)]	—	—	30	>98	28	24.1
a) Sulfonated PS-*b*-fluorinated PI with acid form						
b) Sulfonated PS-*b*-fluorinated PI with cesium salt						

PS-*b*-PI, polystyrene-*b*-polyisoprene (precursor)

Sec-Bu-(-CH$_2$-CH-)$_m$-(-CH$_2$-C=CH-CH$_2$)-$_n$ $\Longrightarrow$ Sec-Bu-(-CH$_2$-CH-)$_m$-(-CH$_2$-CH-CH-CH$_2$)-$_n$

CH$_3$

$\begin{array}{c} F \diagdown C \diagup F \\ | \\ \end{array}$

CH$_3$

F O F 180℃

F$_3$C F $\longrightarrow$:CF$_2$
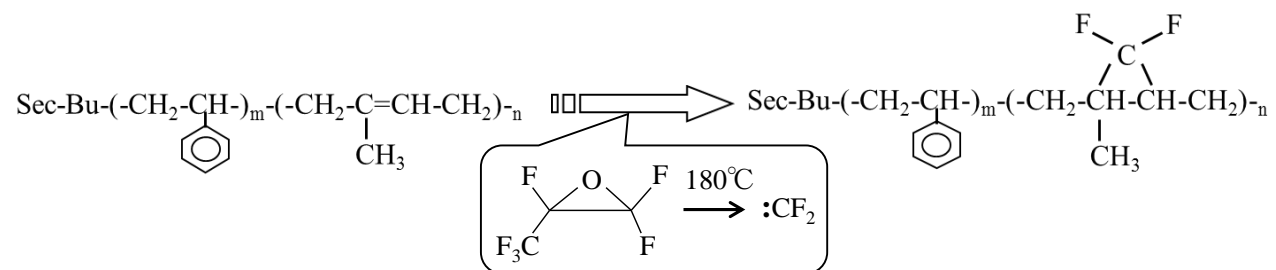
Sulfonated PS-*b*-fluorinated PI (Materials for the experiments)

F C F

Sec-Bu-(-CH$_2$-CH-)$_m$-(-CH$_2$-CH-CH-CH$_2$)-$_n$ $\Longrightarrow$ Sec-Bu-(-CH$_2$-CH-)$_m$-(-CH$_2$-C-CH-CH$_2$)-$_n$

F C F

CH$_3$

Sulfuric acid/
Acetic anhydrous

SO$_3$H **or** SO$_3$Cs
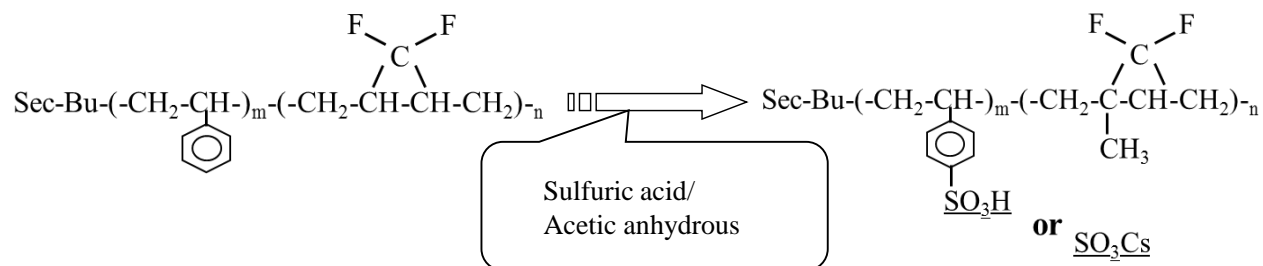
Scheme 2-1 Synthesis conditions for sH-PS-b-f-PI and sCs-PS-b-f-PI
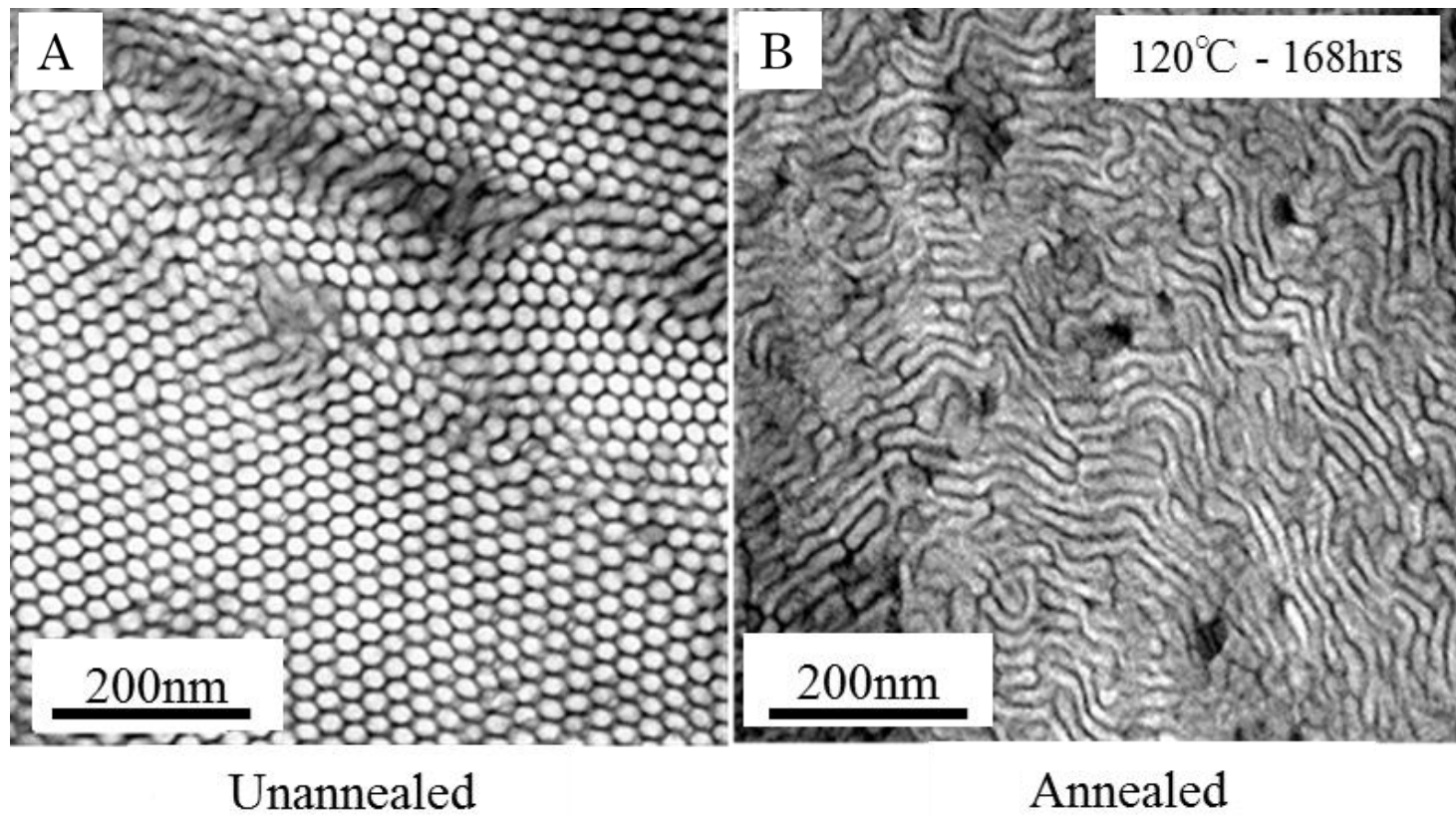
Figure 2-1 TEM micrographs of (A) unannealed and (B) annealed
s-PS-*b*-f-PI film cast from anhydrous tetrahydrofuran (THF).
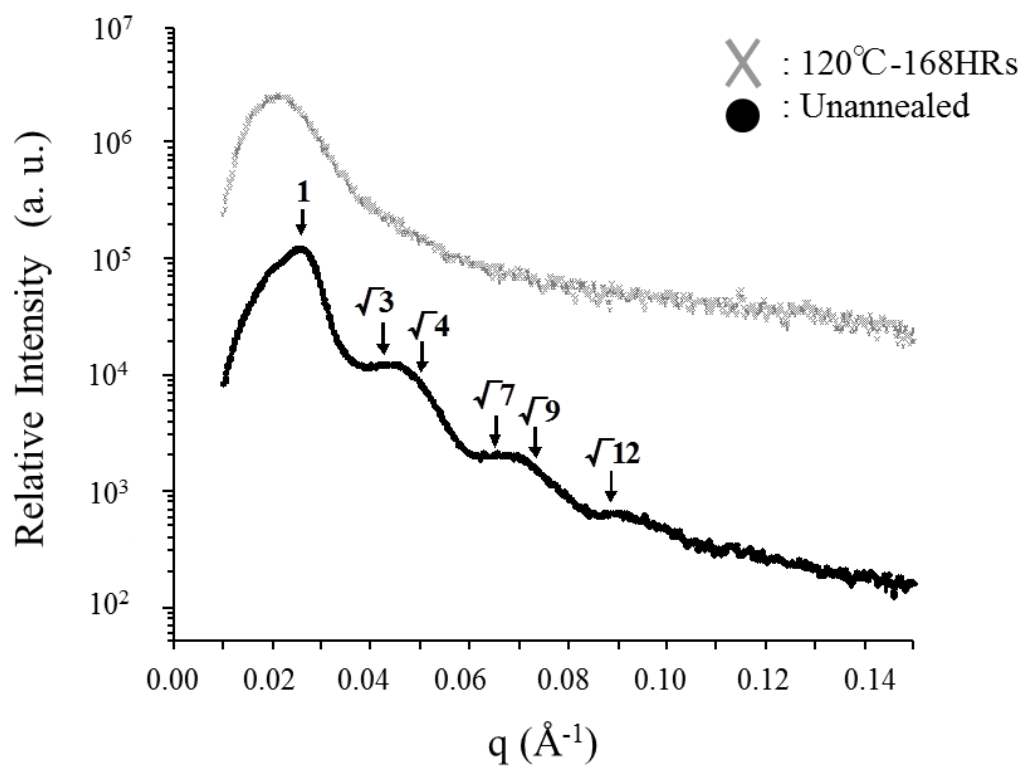
Figure 2-2 SAXS profiles for the unannealed and annealed
sH-PS-*b*-f-PI film cast from anhydrous THF: (●) unannealed,
(✕)120°C-168 h.
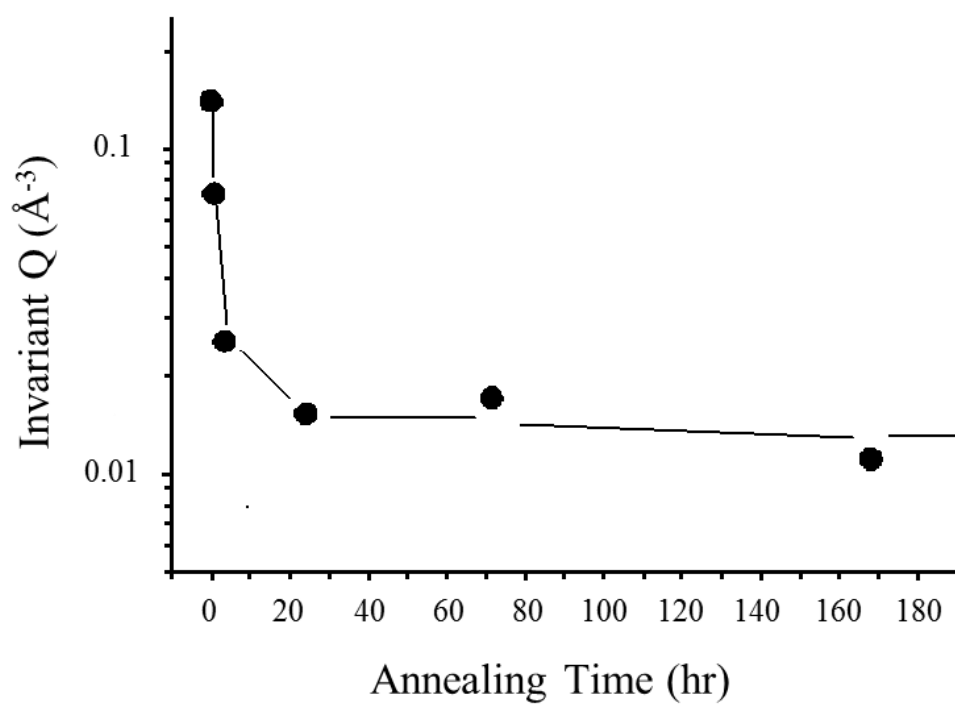
Figure 2-3   Invariant Q versus the annealing time of
the sH-PS-*b*-f-PI film cast from anhydrous THF

Table 2-2 Solubility parameters of solvents and polymers.

Sample	δ (MPa$^{1/2}$)
THF	19.5[a]
THF/Water (98/2, wt/wt)	20.1[b]
Water	48.8[a]
DMSO	26.7[a]
PS	18.6[c]
PI	16.6[c]
a); Taken from Ref. [32]. b); Calculated value.	
c); Taken from Ref. [33].	

Table 2-3 Dielectric Constant of the solvents and Bjerrum Length.

| Sample			Dielectric Constant		Bjerrum Length
					(nm)
THF			7.6		7.5
THF/Water (98/2, wt/wt)			8.8[a]		6.3
Water			80.0		0.7
DMSO			47.2		1.1
a) Calculated value					

(a) Unannealed   (b) Annealed
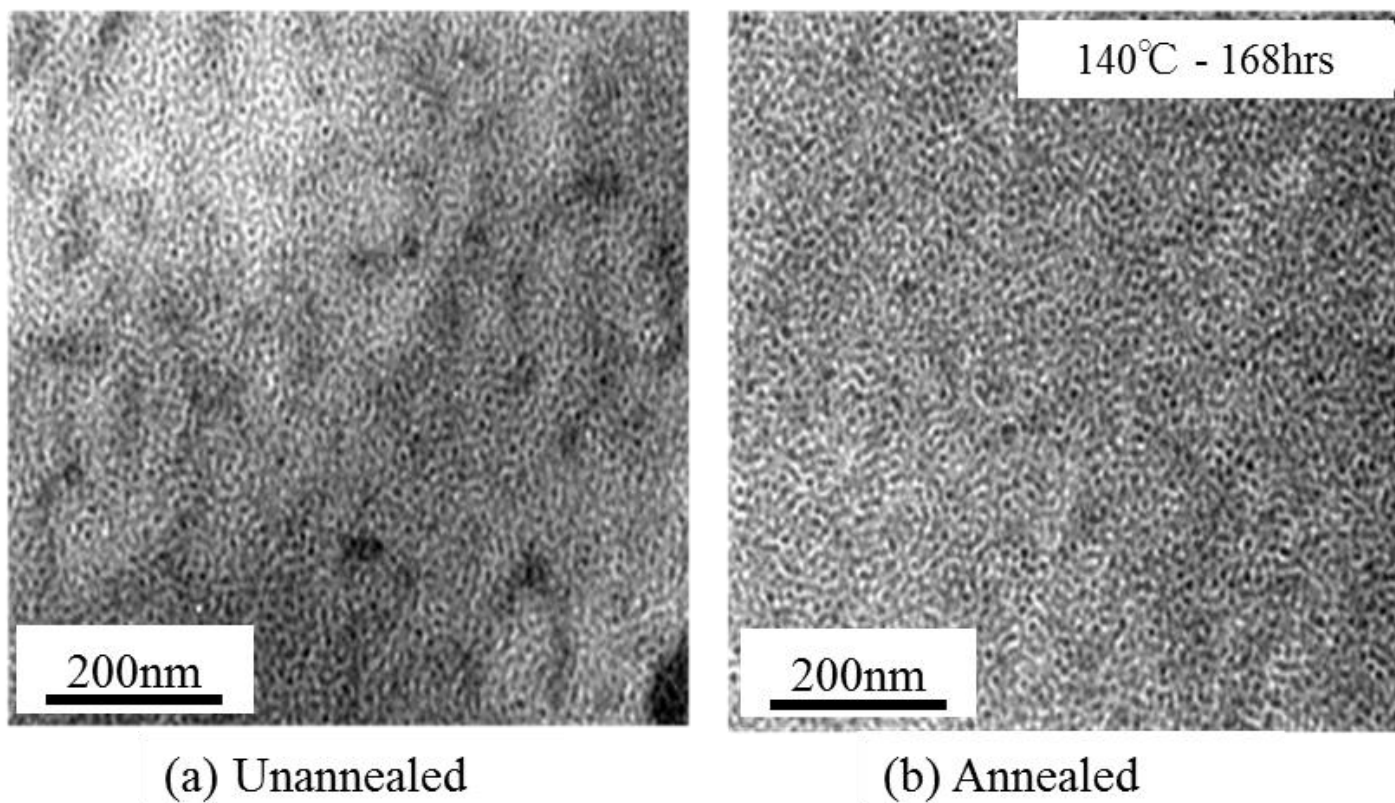
Figure 2-4 TEM micrographs of (A) unannealed and (B) annealed sCS-PS-*b*-f-PI film cast from anhydrous tetrahydrofuran (THF)/water (98/2, wt/wt).
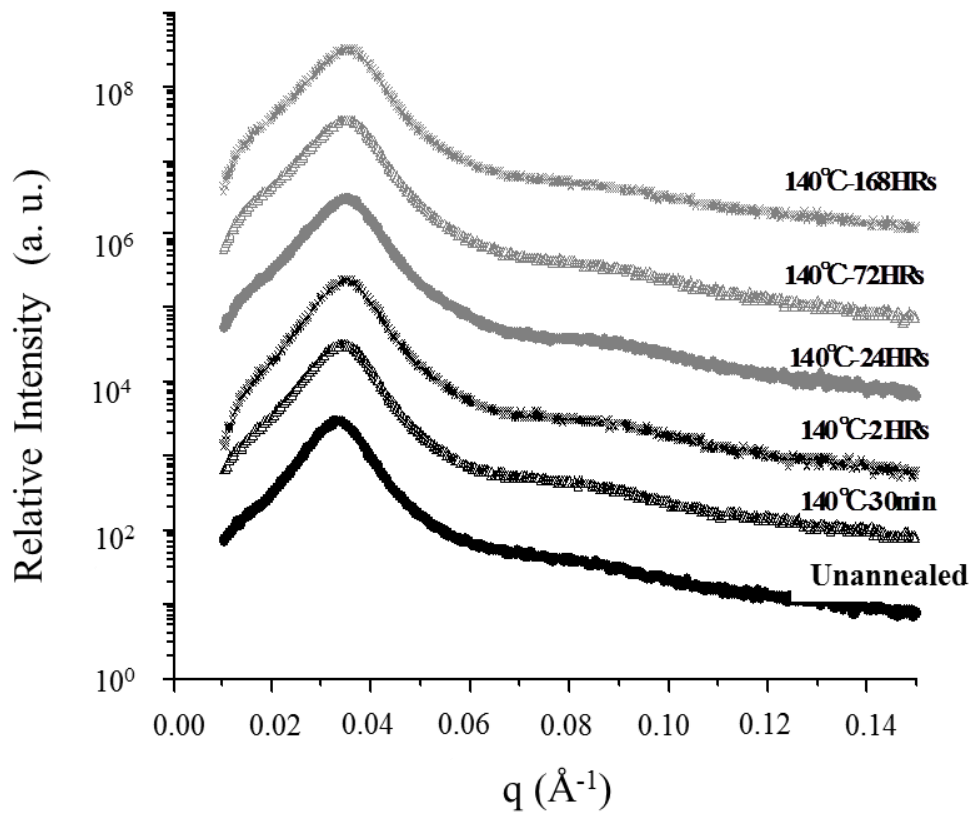
Fig 2-5　Time-resolved SAXS profiles of sCs-PS-*b*-f-PI film cast from THF/Water(98/2, wt/wt): (●)unannealed, (◯)140°C-30min, (✗) 140°C-2 h, (●)140°C-24 h, (◯)140°C-72 h, (✗) 140°C-168 h.
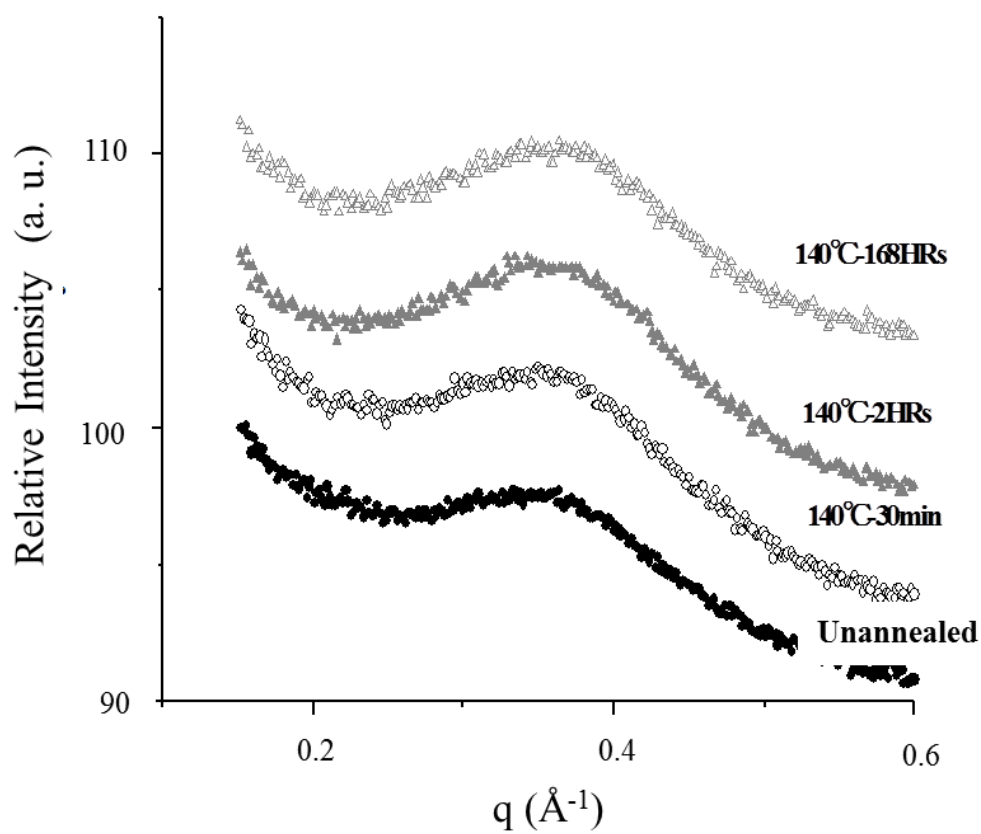
Fig 2-6 Time-resolved IMAXD profiles of sCs-PS-*b*-f-PI film cast from THF/Water (98/2, wt/wt): (●)unannealed, (○)140°C-30 min, (▲)140°C-24h, (△)140°C-168h.
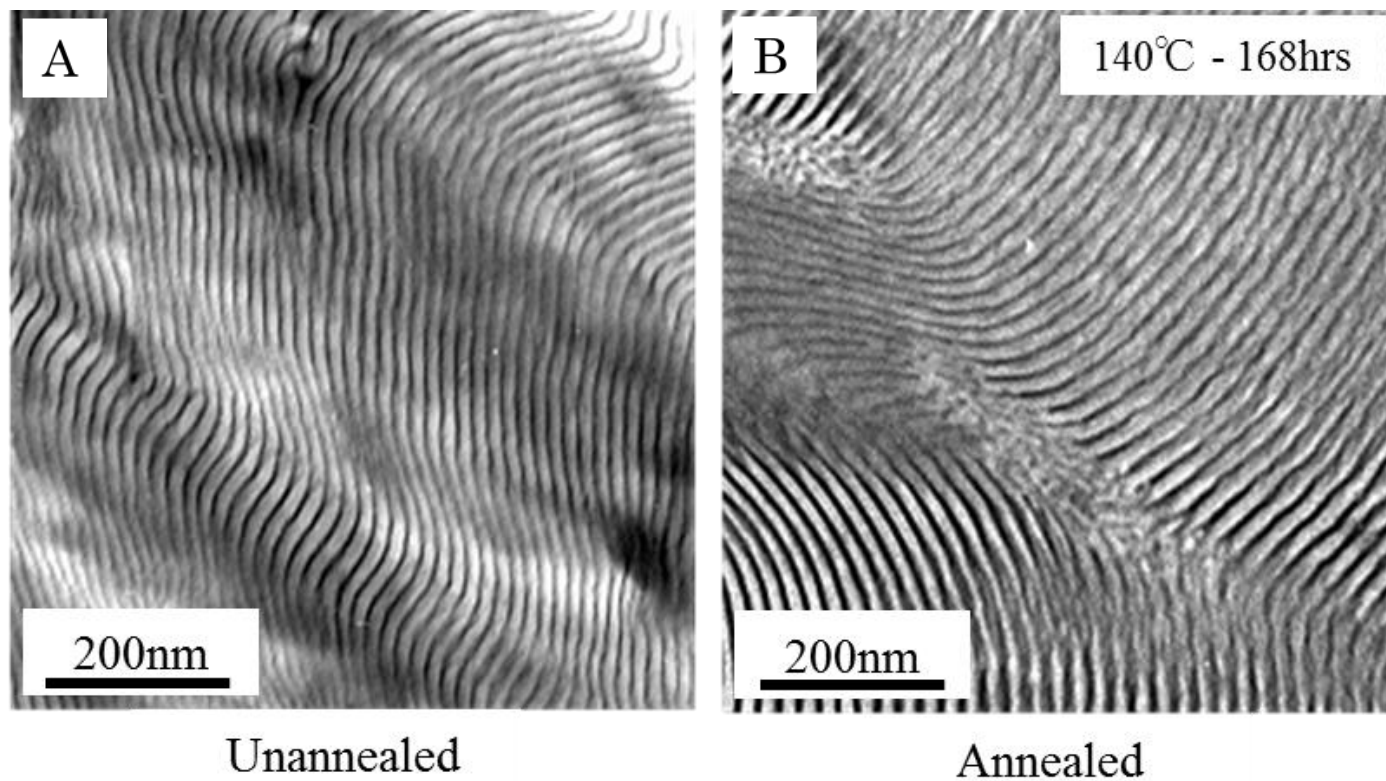
Figure 2-7 TEM micrographs of (A) unannealed and (B) annealed sCs-PS-*b*-f-PI film cast from DMSO.
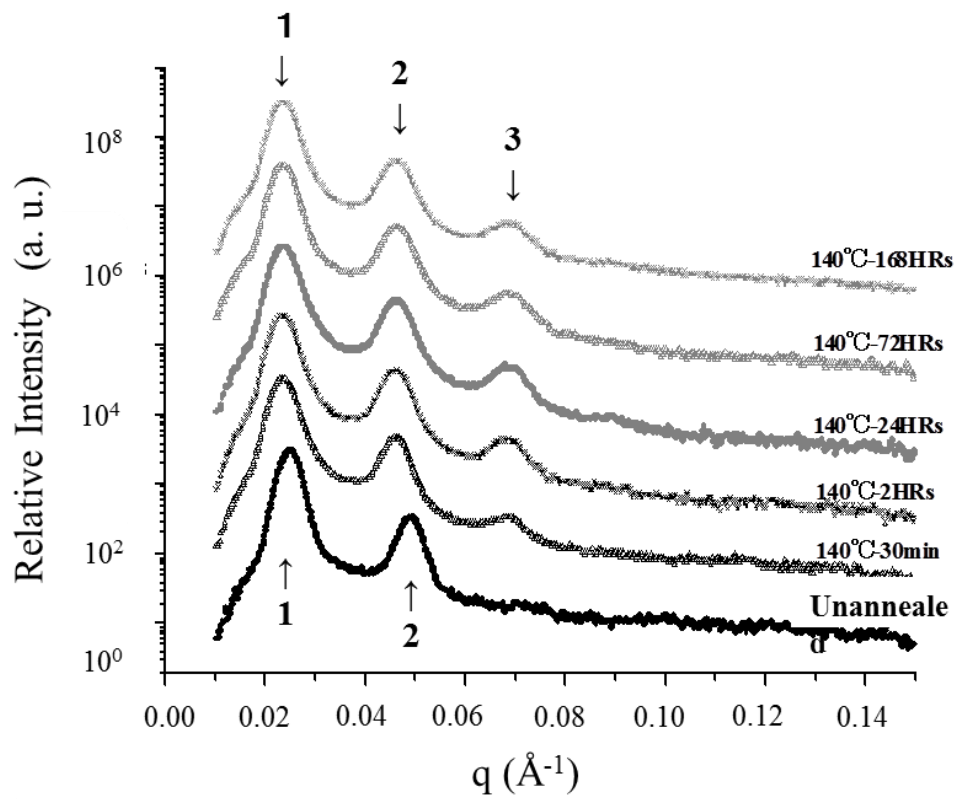
Fig 2-8 Time-resolved SAXS profiles of sCs-PS-*b*-f-PI film cast from DMSO: (●)unannealed, (O)140℃-30min, (✗)140℃-2 h, (●)140℃-24 h, (○)140℃-72HRs, (✗)140℃-168 h.
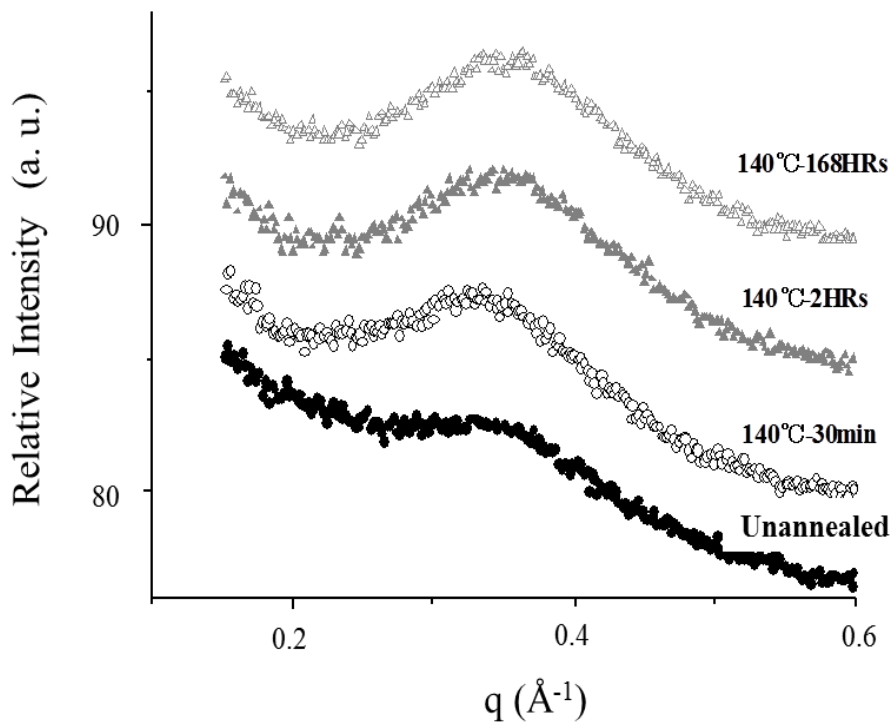
Fig 2-9 Time-resolved IMAXD profiles of sCs-PS-*b*-f-PI film cast from DMSO: (●)unannealed, (○)140℃-30min, (▲)140°C-2 h, (△)140°C-168 h.
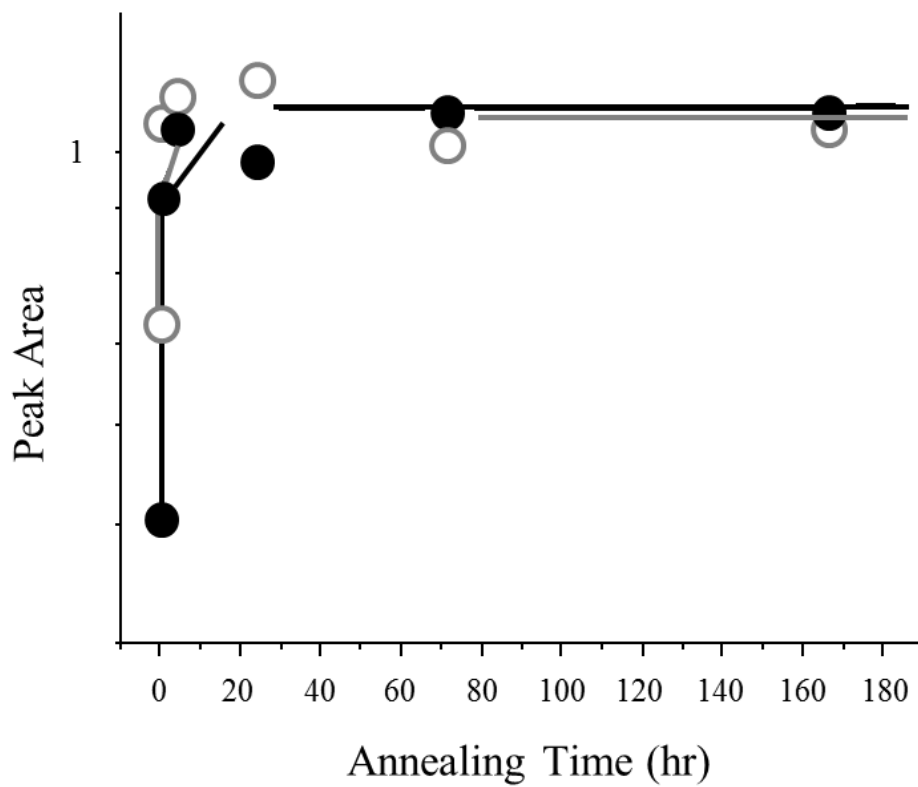
Fig 2-10 Peak Area versus the annealing time: (●)DMSO, (○)THF/Water (98/2, wt/wt).
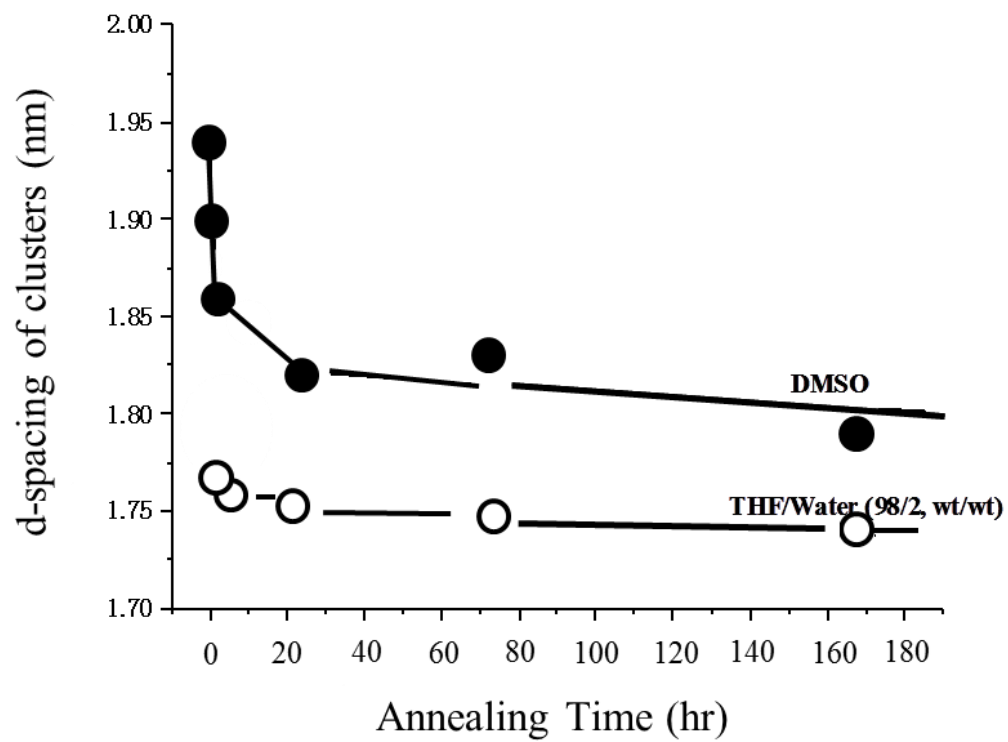
Fig 2-11 d-spacing of the ionic clusters of the sCs-PS-*b*-f-PI film:
(●)DMSO, (○)THF/Water (98/2, wt/wt).

Chapter 3.

Effect of TiO₂ on morphology and mechanical properties of PVDF/PMMA blend films prepared by melt casting process

3.1 Introduction

Introduction

Poly(vinylidene fluoride) (PVDF) is a semicrystalline polymer that is widely used in industry because of its excellent mechanical properties, good chemical resistance to severe environmental stress [1, 2]. However, PVDF has week adhesion to other polymers due to low surface tension resulted from its molecular structure. In order to improve adhesive properties of PVDF, many kinds of polymer blends were studied with respect to interaction between fluorine atoms in PVDF and carbonyl groups in a partner polymer. [3–5] According to those researches, the improvement of adhesive properties is not expected when PVDF forms matrix phase. On the other hand, excellent properties such as chemical resistance and long-term weatherability lose when PVDF forms domain phase in composite materials. In the early 1960's, it was discovered that PVDF and poly(methyl methacrylate) (PMMA) are molecularly miscible in the amorphous state, and the blend material has been studied extensively up to the present time, because the blend materials gave economic efficiency and good mechanical properties [6–8].

There are several reports on the polymer blends of PVDF and PMMA. The general conclusion is that such systems exhibit lower critical solution temperature (LCST) behavior around 330°C. Therefore, these components are miscible in the amorphous state above the melting point of PVDF ($T_m \cong$ 170°C), and PVDF crystallizes from the melt state below the T_m if the blend is maintained above its glass transition temperature (T_g) [9–16].

It is well known that PVDF can crystallize into at least four different crystal structures (α, β, γ, and δ) [17]. Crystal structures of PVDF depended on crystallization temperatures during melting process and stretching conditions [18-24]. For PVDF/PMMA blend materials, crystal structures were dominated by cooling conditions and the blend ratio of PVDF/PMMA [25, 26].

In the aim of the improvement of outstanding properties for PVDF films, titanium dioxide (TiO_2), one of the inorganic materials, has received the most attention because of its excellent properties such as long-term stability, nontoxicity, and resistance to discoloration under UV light. Cao et al. reported that the small nanoparticles (average diameter: ~10 nm) improved the antifouling property of the PVDF membranes and had a substantial effect on the crystallization of PVDF [27]. In addition, the crystallinity of PVDF decreased, as the ratio of TiO_2 nanoparticle (average diameter of ~400 nm) in the PVDF increased [28].

Economic efficiency, an improvement of adhesive properties to other materials, and hydrophilicity are expected by adding PMMA to PVDF. Since TiO_2 particles have superior properties as mentioned above, there are several reports on PVDF/PMMA/TiO_2 composite materials. Zhao et al. prepared PVDF/PMMA/TiO_2 composite materials by adding TiO_2 nanoparticles (1−5 wt%) during the in situ polymerization of methyl methacrylate (MMA) in PDVF. They revealed that the hydrophilicity was enhanced as the TiO_2 content increased [29]. For PVDF/PMMA/TiO_2 (65/20/15, wt/wt/wt) blend films prepared by the melt casting process, crystal structures of PVDF were studied. The result showed that the β phase of PVDF was formed and its structural conversion to the α phase was observed with increasing chill roll temperature [30]. In addition, for PVDF/PMMA/TiO_2 (80/20/30, wt/wt/wt) blend films, the α phase of the PVDF was formed when the chill roll temperature was above 78°C. Based on the morphological study, it was suggested that the excluded PMMA was entrapped within the interlamellar region in the spherulites because of the fast growth rate of the α phase [31]. Tang et al. studied melt-mixed PVDF, PVDF/PMMA and PVDF/PMMA/TiO_2 blown films developed for solar cell encapsulation. In the study, they found that PVDF films formed the α phase, and PVDF/PMMA films containing 10, 20, and 30 wt% PMMA exhibited coexistence of the α and β phase.

With regard to mechanical properties, the addition of 15 wt% TiO_2 to PVDF/PMMA blends (70/30, wt/wt) improved the elongation at break of the blown film compared with the film which were not containing TiO_2 [32]. In a different study of PVDF/PMMA/TiO_2 blend films, it was reported that the addition of 2−10 wt% TiO_2 (primary diameter of 260−300 nm) to PVDF/PMMA (70/30, wt/wt) resulted in an improvement in the tensile strength and elongation at break [30]. Lee et al. found that the elongation at break increased in the value from 0 to 10 wt% TiO_2 in the composite, followed by a decrease beyond 10 wt% [33]. Those results showed that PVDF/PMMA/TiO_2

blend films exhibited good mechanical properties. In addition, PVDF/PMMA/TiO$_2$ blend films are a promising material for a photovoltaic cell and module because of long-term weatherability. One of the studies revealed that the weatherability of the β phase of PVDF in the film after pressure cooker test (PCT) decreased as a result of yellowing because of the unstable structure of β phase [33−34].

Our previous study showed the crystalline orientation in PVDF/PMMA/TiO$_2$ blend films prepared by a melt casting process with a slit die, which is one of the melt casting process [31]. However, there is no investigation how orientation of crystals influences mechanical properties, although anisotropic morphology is an important factor dominating film properties in practical use. In addition, there are few reports on the effect of TiO$_2$ with regards to morphology and mechanical properties of PVDF/PMMA blend films. Lee et al. reported mechanical properties with respect to different TiO$_2$ contents on PVDF/PMMA/TiO$_2$ blend films cast at the chill roll temperature of 50°C, and they did not mention the blend ratio of PVDF/PMMA and anisotropic morphology on the film [34].

Therefore, we focused to study the effects of TiO$_2$ on mechanical properties and morphology of PVDF/PMMA blend films prepared by a melt casting process in terms of machine direction (MD) and transverse direction (TD). The morphology of PVDF/PMMA and PVDF/PMMA/TiO$_2$ blend films was evaluated by using wide-angle X-ray diffraction (WAXD), scanning electron microscopy (SEM), and dynamic mechanical analysis (DMA). Mechanical properties were conducted by a using tensile tester.

3.2 Experimental

3.2.1 Materials

The PVDF used in this study was supplied by Kureha Corporation (Japan), and the molecular weights were 194,000 (Mw) and 86,000 (Mn). The PMMA was purchased from Asahi Kasei Chemicals (Japan), and the molecular weights measured by gel-permeation chromatography were 130,000 (Mw) and 86,000 (Mn). The rutile TiO$_2$ particles (average diameter: ~290 nm) was purchased from DuPont (Wilmington, DE, USA).

3.2.2　Film preparation

PVDF/PMMA/TiO$_2$ blend films were prepared by a melt casting process with a slit die. The composition of PVDF/PMMA was fixed at the weight ratio of 80:20. 0, 10, 20, 30 wt% TiO$_2$ particles were added to the PVDF/PMMA blend materials. The composite materials of PVDF/PMMA/TiO$_2$ were first pelletized by using a twin screw extruder. After obtaining pellets, films (20 μm in thickness) were extruded and cast at the chill roll temperature of 100ºC. The barrel temperature was 240°C, the width of the slit die was 270 mm, and the die gap was 0.5 mm. The shear rate was calculated to be 38 sec^{-1} from the extrusion output of 3.1 kg/h, density of 1.7 g/cm^3 of the PVDF/PMMA blend material, and die size. Different TiO$_2$ contents of 0, 10, 20, and 30 wt% in PVDF/PMMA (80/20, wt/wt) blend materials were applied in this study. The corresponding films were coded as PMTi-0, PMTi-10, PMTi-20 and PMTi-30, respectively.

3.2.3　Measurement

The film surface temperature during the melt casting process was measured by a contact thermometer. The measured area was not evaluated in this study because its appearance was insufficient. In this study, chill roll temperature refers to the surface temperature of the chill roll measured by the contact thermometer.

Tensile modulus was measured with an Tensilon　RTM-100(Toyo　Baldwin Co., Japan) at 23ºC and 50% humidity. The specimen size was 20 mm wide by 100 mm long (gauge length), and the crosshead speed was 10 mm/min. Elongation at break was performed by the equipment and environment. The specimen size was 10 mm wide by 50 mm long with 500 mm/min in the crosshead speed. In order to measure Poisson's ratio, strain is measured both in the tensile direction and at horizontal direction using an Autograph (model AG-kNXPlus, Shimazu Seisakujyo Co., Japan) and a noncontact displacement gauge (model, TRViewX500D, Shimazu Seisakujyo). The original distance between gauge marks of length and wide was 25 mm and 10 mm respectively. The crosshead speed was 5 mm/min at 23ºC.

WAXD measurements were performed using a NANO-Viewer system (Rigaku Co., Japan). Cu–Kα radiation (40 kV, 20 mA) was generated and collimated by a confocal mirror system. The wavelength and the camera length were 1.54 Å and 70 mm, respectively. An imaging plate (IP), (BAS-SR

127, Fujifilm Co., Japan) was used as a two-dimensional detector, and the IP reading device RAXIA-Di (Rigaku Co.) was employed to transform the obtained image into text data.

The cross sections of PVDF/PMMA/TiO$_2$ films were prepared using an ion milling system (model IM4000, Hitachi Hightechnologies Co., Japan) with 4 kV for 1 h in cold atmosphere with liquid nitrogen. The samples were observed using SEM (model 8020, Hitachi Hightechnologies) with the accelerating voltage of 1 kV.

The thermal behavior of the films was examined using thermal analysis apparatus (DSC 8500, Perkin-Elmer, MA, USA). An appropriate amount of sample (typically 10mg) was sealed in an aluminum pan. The temperature was raised from 30ºC to 220ºC at a heating rate of 20ºC/min, then maintained for 10 min, then cooled to 30ºC at 20ºC/min. The whole process was conducted under a nitrogen atmosphere.
The morphology of the film surfaces was observed using the SEM with the accelerating voltage of 3 kV after coating platinum particles under vacuum-dried conditions.

DMA measurements were conducted by using an RSA-3 device (TA Instruments Inc., USA) at the heating rate of 2°C/min. The frequency was 10 Hz and the temperature range was from −80°C to 120°C.

3.3   Results and Discussion

3.3.1   Film temperature during the melt casting process

Film temperature during the melt casting process
Figure 3-1 shows the film temperature profile of PVDF/PMMA blend films during the melt casting process at the chill roll temperature of 100°C. Zero seconds on the x axis refers to the time at which the molten material just begins to flow from the die gap. As seen the figure, a rapid decrease in the film temperature begins at 2.6 s because the molten material contacted the chill roll at this time. It was found that the film temperature reached 102°C at 4.2 s. The film was pealed from the chill roll after casting for 10 s. The film was wound at room temperature after pealed the chill roll. This result indicates that the cooling system is sufficient for allowing the films to reach the chill roll temperature.

3.3.2 Effect of TiO₂ on tensile modulus and morphology

Figure 3-2 shows tensile moduli in the MD and the TD of films as a function of TiO₂ content. MD is parallel with the material flow during the melt casting process. TD is known as the cross direction to MD. Tensile moduli of PMTi-0 are approximately 2300 MPa in both the MD and the TD. The tensile moduli increased with increasing TiO₂ content, and that of PMTi-30 reached approximately 3000 Mpa in both the MD and the TD. The tensile modulus in the MD showed slightly higher than that in the TD, regardless of the TiO₂ content for all samples. Our previous study on PVDF/PMMA/TiO₂ (80/20/30, wt/wt/wt) blend films observed that molecular chains of PVDF had the slight MD orientation in films prepared by the melt casting process with the slit die when the chill roll temperature was above 90°C [31]. We confirmed the MD orientation of PVDF crystals for all samples by WAXD measurements in this experiment. Therefore, it is assumed the reason of the slightly higher modulus in the MD compared with that in the TD is the orientational effect.

In general, incorporating inorganic nanoparticles into polymer matrix is a practical way to obtain advanced materials of composites [35]. It is well known that tensile modulus of a two-phase blends depends on the size, shape, and distribution of dispersed particles or the coarseness and tortuosity of a continuous phase. Several theories were developed to predict the modulus of a two-phase blends [36−41]. It is estimated that PVDF/PMMA composite materials form matrix phase and TiO₂ particles disperse in the matrix. Therefore, it is expected that tensile modulus of films should be predicted by the theories which are the parallel model [36−39], the series model [36−39], the Halpin−Tsai model, and the Kerner model [37, 39]. Using these models, we examined dispersed state of TiO₂ particles and morphology of the matrix.

Parallel model is given by Equation (1), and represents the upper bounds of the tensile modulus. This model is applicable to materials in which the components are connected parallel to one another so that the applied stress lengthens each component to the same extent.

$$E = E_1\varphi_1 + E_2\varphi_2 \qquad\qquad\qquad (1)$$

Series model represents the lower bounds of the tensile modulus, and given by Equation (2). For the model, the blend components are arranged series perpendicular to the direction of the applied force.

$$\frac{1}{E} = \frac{\varphi_1}{E_1} + \frac{\varphi_2}{E_2} \tag{2}$$

where E is the tensile modulus of the blend material. E_1 and E_2 are tensile moduli of components 1 and 2. φ_1 and φ_2 are corresponding to volume fractions of components 1 and 2 [36, 37].

Halpin−Tsai model given by Equation (3) has been successfully applied by several researchers to systems of binary polymer composites [36, 37].

$$\frac{E_1}{E} = \frac{(1 + A_i B_i \varphi_2)}{(1 - B_i \varphi_2)} \tag{3}$$

where

$$B_i = \frac{(E_1/E_2) - 1}{(E_1/E_2) + A_i} \tag{4}$$

In the Halpin−Tsai Equation, subscripts 1 and 2 refer to the continuous and dispersed phases, respectively. The constant A_i is defined by morphology of the system. For elastomer domains dispersing in a continuous hard matrix, A_i is 0.66. Instead, if the hard material forms the dispersed phase, A_i is 1.5 [37, 38].

Another important model for perfect adhesion between a continuous and dispersed phase is the Kerner Equation. Kerner derived a theory for a matrix with spherical inclusions, when the system is isotropic and adhesion between the two phases is perfect. The Kerner model is given by equation (5) [37, 39].

$$E = E_m \left[\frac{\varphi_d E_d / [(7 - 5\upsilon_m)E_m + (8 - 10\upsilon_m)E_d] + \varphi_m/15(1 - \upsilon_m)}{\varphi_d E_m / [(7 - 5\upsilon_m)E_m + (8 - 10\upsilon_m)E_d] + \varphi_m/15(1 - \upsilon_m)} \right] \tag{5}$$

where E is the tensile modulus of the blend material, υ is Poisson's ratio of the matrix, and φ is the volume fraction. The subscripts m and d stand for the matrix and dispersed phase, respectively. Those models are applicable to a two-phase systems and useful for the prediction of the phase morphology in the system that TiO_2 particles disperse in PVDF/PMMA matrix. Figure 3-3

shows the SEM micrographs of the cross section of PMTi-30. As seen in Figure 3-3, the dispersity of TiO_2 was mostly homogeneous in the polymer matrix. We also confirmed that the dispersity of TiO_2 particles was improved as the TiO_2 content decreased in the composites.

Figure 3-4 shows comparisons of the calculated and the experimental curves of the tensile modulus in the MD as a function of TiO_2 content. Figure 3-5 represents those in the TD. For comparison, experimental tensile moduli exhibited in Figure 3-2 are also shown in Figure 3-4 and 3-5. Experimental tensile moduli in the MD and TD of PVDF/PMMA blend films with 0 wt% TiO_2 were adopted as the value of a continuous phase, when calculating tensile moduli of PMTi-10, PMTi-20, and PMTi-30. In addition, the tensile modulus of 283 GPa was used for the calculation as the value of TiO_2 particle [40]. Since TiO_2 is a harder material than the matrix, 1.5 of A_i is used for the Halpin−Tsai Equation. For the calculation of the Kerner model, the experimental values of the Poisson's ratio (MD: 0.040, TD: 0.042) was adopted.

As seen in Figure 3-4 and 3-5, moduli calculated by the series model exhibited smaller values compared with experimental moduli for all samples. By contrast, calculated moduli obtained from the parallel model attained extremely higher values. The moduli of PMTi-0 calculated by parallel model were approximately 14000 Mpa in the MD and TD. On the other hand, moduli of PMTi-10 calculated by the Halpin−Tsai model and the Kerner model were consistent with experimental moduli in the MD and TD. From these results, the isotropic dispersity of TiO_2 particles was indicated. Furthermore, it was estimated that the adhesion between TiO_2 particles and the PVDF/PMMA phase is significantly stronger under the strain in tensile measurements, which is less than 1%. However, experimental moduli of PMTi-20 and PMTi-30 in both the MD and TD were smaller values compared with calculated ones obtained from the Halpin−Tsai and Kerner model.

Figure 3-6 represents the WAXD profiles with different TiO_2 contents. All samples showed similar WAXD profiles, regardless of the TiO_2 content. All profiles had peaks 2θ of 17.4º, 18.2º, and 19.8º, and these peaks correspond to the α phase Bragg diffraction of (100), (020), and (110), respectively [30, 31, 33]. As seen in the Figure, all samples prepared at the chill roll temperature of 100ºC formed the α phase of PVDF. Therefore, it was revealed that TiO_2 particles had no significant effect on crystal structures of PVDF. Based on the WAXD profiles, crystallinity was calculated by Equation (6).

$$Xc\ (\%) = \frac{A_c}{A_\alpha + A_c} \times 100 \qquad\qquad (6)$$

where Ac is the area of the crystalline phase and Aα is the area of the amorphous in the WAXD profiles presented in Figure 3-6. Figure 3-7 shows crystallinity with different TiO_2 contents. The crystallinity of either PMTi-0 or PMTi-10 was 35%. However, the crystallinity followed by a decrease beyond 10 wt% TiO_2, and the crystallinity of PMTi-20 and PMTi-30 was 32% and 25%, respectively. As mentioned above, calculated tensile moduli were obtained by using experimental tensile moduli in the MD and TD of the PVDF/PMMA blend film which does not contain TiO_2 particles, so that it is assumed the deviation to lower side of experimental tensile moduli for films containing 20−30 wt% TiO_2 is due to the decrease of the crystallinity. If the modulus of PMTi-20 and PMTi-30 by the crystallization decreases approximately 4% and 7%, respectively, the experimental tensile modulus mostly coincided with calculated one obtained from the Halpin-Tsai model.

Figure 3-8 shows the SEM micrographs of the film surfaces of both chill roll side and the opposite one of PMTi-0 and PMTi-30. There are no significant difference between the chill roll side and the opposite one. Sheaflike spherulites can be clearly seen in PMTi-0, and both sheaflike spherulites and TiO_2 particles can be clearly seen in PMTi-30. Generally, inorganic particles act as a nucleus and enhance crystallinity [41, 42], and it was reported that the increase of crystallization temperature in the cooling process were observed in PVDF/PMMA/TiO_2 blend materials by differential scanning calorimetry (DSC). This result indicates that TiO_2 particle acts as a nucleus regent [33, 34]. Our result also showed the increase of crystallization temperature in the cooling process, as seen in Figure 9 and 10. The crystallization temperature of PMTi-0, PMTi-10, PMTi-20, and PMTi-30 was 127ºC, 129ºC, 130ºC, and 131ºC, respectively. However, on carefully study of the SEM micrographs of PMTi-30, it seems that TiO_2 particles hinder the crystal growth owing to the existence of TiO_2 particles. This observation is clearly recognized within the dotted circles in the micrographs. From the morphological observations, it was found that the decrease of crystallinity with increasing TiO_2 content was due to hindrance of crystal growth by some of TiO_2 particles, even though different TiO_2 particles acted as a nucleus regent. In addition, the MD orientation of PVDF chains is recognized because most of lamellae in sheaflike spherulites grow along the TD, as seen in all

SEM micrographs.

Figure 3-11 shows plots of the storage modulus (E') versus temperature in the TD of films. Figure 3-12 denotes plots of the loss modulus (E") versus temperature in the TD of films. With increasing TiO_2 content, the values of E' increased over the entire temperature range. This was similar result to the tensile modulus shown in Figure 3-2. All samples exhibited peaks of the E" curves at approximately -45ºC and 55ºC, as seen in Figure 3-12. Hirata et al. clearly defined the E" peaks for PVDF/PMMA composite materials obtained by melt-mixed blends [43, 44]. According to their reports, there is a four-phase morphology in the melt mixed PVDF/PMMA blend materials that the PVDF content is >60 wt%. The four-phase morphology composed of a mixed amorphous phase with $T_g \approx 55$ºC, an amorphous PVDF phase with $T_g \approx -40$ºC, an imperfect crystalline phase, and a nearly pure PVDF crystalline phase [43, 44]. PVDF/PMM/TiO_2 blend films prepared at various chill roll temperatures from 30ºC to 115ºC by the melt casting process with the slit die exhibited peaks at the similar temperature [33]. Therefore, based on previous studies, the peak observed near 55ºC is attributed to the mixed amorphous phase, and that near -45ºC is attributed to the amorphous PVDF phase for the films. It was found that the peak positions ascribed to the mixed amorphous phase of PVDF/PMMA was not affected by adding TiO_2 particles in our experiments. We also confirmed that peaks in the E" curves seen in the MD of films was the similar results.

Based on the theories on the tensile modulus for binary blends and the SEM micrographs, it was revealed that TiO_2 particles in the PVDF/PMMA/TiO_2 blend films disperse homogeneously in the polymer matrix and the system is isotropy and significant adhesion between the two phases. It was suggested that TiO_2 particles used in the experiment did not affected both the crystal structure of PVDF and the morphology of PVDF/PMMA mixed amorphous, but hindered the crystallization of PVDF.

3.3.3　Anisotropy on elongation at break of films

Figure 3-13 shows the effect of TiO_2 content on the MD and the TD elongation at break of films. The MD elongation at break of PMTi-0 represents 230%, and that of PMTi-10 reached 330%. This increment is because TiO_2 particles functioned as physical junctions in the film during the extrusion [34]. Beyond 10 wt% TiO_2 content, the elongation at break decreased with increasing TiO_2 content in the film, and the MD elongation at break of PMTi-30 became 280%.

Meanwhile, the TD elongation at break of PMTi-0 was 9%, and the value was quite small compared with that of 230% seen in the MD elongation at break of PMTi-0. The TD elongation at break slightly increased with increasing TiO_2 content, and that of PMTi-30 reached 21%. The results mean that films have an extreme anisotropy property with regard to elongation at break. In order to investigate the cause resulting in the anisotropic properties, we examined the relationship between spherulitic morphology and stress−strain (S−S) behavior.

Figure 3-14 shows the S−S curves and the SEM micrographs of the film surfaces when tensile force was applied along the MD. Figure 3-15 shows that in the TD. The SEM micrographs of the film surfaces seen in Figure 3-14 correspond to 200% and 170% elongation of PMTi-0 and PMTi-30, respectively. When comparing the SEM image of the film surfaces between 0% elongation seen in Figure 3-8 and 200% elongation seen in Figure 3-14, it was found that spherulites deformed significantly along the MD. For PMTi-30, it was observed not only the deformation of spherulites but also the interfacial peeling (shown within the dotted circles) between TiO_2 particles and the matrix. It was thought that the interfacial peeling is the reason for the decrease of the elongation with increasing TiO_2 content beyond 10 wt%. It was also reported in a different paper that the elongation at break decreased beyond 10 wt% along with the reduction of crystallinity, because lower crystallinity would break at a smaller stress [33].

On the other hand, the morphological observation for the TD seen in Figure 3-15 identified that cracks perpendicular to direction of the applied force were seen within spherulites. This event was observed regardless of incorporation of TiO_2 particles. PVDF crystals in films used in this experiment have the MD orientation, and the fact can be judged from our previous study [31] and the growth direction of lamellar seen in Figure 3-8 as mentioned above.

For PVDF/PMMA blend materials, PVDF crystalized with the exclusion of PMMA and the excluded PMMA existed in the amorphous pockets [8, 45] Therefore, when tensile force was applied along MD of the film, it is expected that spherulites deform easily under stress because the flexible amorphous existing within the interlamellar region can be stretched along the applied force. By contrast, when tensile force is applied along TD, lamellae themselves are compelled to the deformation of spherulites. Thus, the reason why films fractured at the small elongation because the spherulites could not endure the stress. Based on the morphological observations, it was deduced that the remarkable anisotropy on the elongation at break of films is due to the

orientation of PVDF crystals, and the orientation is owing to the flow field caused by the melt casting process with the slit die. Figure 3-16 shows a schematic illustration when tensile force was applied along MD and TD. Furthermore, the yield stress of PMTi-0 was higher than that of PMTi-30 for either the MD or the TD, as seen in Figure 3-14 and 3-15. This probably resulted in higher crystallinity of PMTi-0 because yield stress is attributed to tilting stress for lamellae in spherulites.

3.4 Conclusion

PVDF/PMMA/TiO$_2$ blend films were prepared by a melt casting process, and effect of TiO$_2$ on morphology and mechanical properties was studied using WAXD, SEM, DMA, and tensile testing machine. As increasing TiO$_2$ content, tensile moduli in both the MD and TD increased, and the modulus in the MD had slightly higher value than that in the TD regardless of the TiO$_2$ content. This is due to the MD orientation of PVDF crystals. Prediction of the tensile modulus by using several theories was conducted. As a result, tensile moduli calculated by the Halpin-Tsai and the Kerner model were consistent with experimental moduli in both the MD and TD for PVDF/PMMA blend films containing 10 wt% TiO$_2$. However, experimental tensile moduli exhibited smaller values compared with calculated ones, as the TiO$_2$ content increased to 30 wt%. Based on morphological observations, it was revealed that TiO$_2$ particles did not affect the crystal structures of PVDF and the morphology of the PVDF/PMMA amorphous phase. In addition, the decrease of crystallinity with increasing TiO$_2$ content was due to hindrance of crystal growth by some of TiO$_2$ particles, even though different TiO$_2$ particles acted as a nucleus regent. From the results, it was deduced that the deviation between the calculated and the experimental tensile modulus was due to the decrease of crystallinity.

In the study on the elongation at break of films, the MD elongation at break represented more than 200%, and the TD elongation at break exhibited less than 20%. Based on the result of the S-S behavior and the SEM micrographs of the film surfaces, it was identified that sheaflike spherulites can deform along the MD when tensile force is applied along MD of the film. The reason why such spherulites can deform along the MD is due to stretching of the amorphous phase existing within the interlamellar region. By contrast, sheaflike spherulites fractured when tensile force applied along TD, because lamellae themselves were compelled to deformation and could not deform along the TD, because of the orientation of PVDF crystals. Therefore, it was deduced that such properties of elongation at break is caused by the anisotropy of spherulites formed owing to the flow field caused by the melt casting process with the slit die.

3.5 References

[1] McCarthy, RA, *Encyclopedia of Polymer Science and Engineering*, Vol, 3, ed., John Wiley, New York, 1985.

[2] Scheinbeim JI, *Polymer Data Handbook*, Oxford Univ. Press, Oxford, UK. 1999

[3] Lee WK, Ha CS. *Polymer* 1998, 39, 7131-7134

[4] Salim A. Yousefi AA. *J. Polym. Sci.* 2004, B42, 3487-3495

[5] Huang C. Zhang L. *J. Appl. Polym. Sci.* 2004, 92, 1-5

[6] Hourston DJ, Hughes ID. *Polymer* 1977, 18, 1175-1178

[7] Wendorff H, Ullmann W. *Comp. Sci. and Tech.* 1985, 23, 97-112

[8] Cebe P, Chung SY. *J. Mater. Sci.* 1990, 25, 2367-2378

[9] Bernstein RE, Barlow JW. Macromolecules 1977, 10, 3, 681

[10] Noland JS, Schmitt JM. *Adv. Chem. Ser.,* 1971, 99, 15

[11] Nishi T, Wang TT. *Macromolecules* 1975, 8, 909

[12] Wang, TT, Nishi T. *Macromolecules* 1977, 10, 421

[13] Douglass D, McBrierty VJ. *Macromolecules* 1978, 11, 766

[14] Chuang H, Han CD. *J. Appl. Polym. Sci.* 1984, 29, 2205

[15] Wolf M, Wendorff JH. *Polymer* 1989, 30, 1524

[16] Yang H, Han CD. *Polymer* 1994, 35, 1503

[17] Tashiro K, *Ferroelectrics* 1981, 32, 167

[18] Nakamura S, Sasaki T. *Makromol Chem.* 1975, 176, 3471

[19] Welch GJ, Miller RL. *J. Polym. Sci. Polym. Phys. Ed.* 1976, 14, 1683

[20] Mancaella L. *Polymer* 1977, 18, 1240

[21] Prest MW. Jr, Luca DJ. J Appl. Phys. 1979, 46, 4136

[22] Lonvinger AJ, Keith HD., *Macromolecules* 1979, 12, 919

[23] Morra BS, Stein RS. *J. Polym. Sci. Polym.* Phys. Ed. 1982, 11, 2243

[24] Hsu TC, Geil PH. *J. Mater. Sci.* 1989, 24, 1219

[25] Horibe H, Baba F. *Nippon Kagaku Kaishi* 2000, No.2, 121

[26] Horibe H, Taniyama M. *J. Electrochem. Soc.* 2006, 153, G119

[27] Cao X, Ma J. *Applied Surface Sci.* 2006, 253, 2003-2010

[28] Rekik H, Boiteux G, Kallel A. *Composites* Part B, 2013, 45, 1199-1206

[29] Zhao X, Wang X. *J. Polym. Res.* 2012, 19, 9862-9871

[30] Lee JG, Kim SH. *Macro. Res.* 2011, 19, 72-78

[31] Hosoda T, Yamada T. *J. Polym. Eng.* 2013, 33, 639-649

[32] Tang E, Yuan H. *J. Mater. Sci.* 2011, 46, 6656-6663

[33] Lee JG, Park SH. *Macro. Res.* 2013, 21, 349-355

[34] Li W, Li H. *J. Mater. Sci.* 2009, 44, 2977-2984

[35] Long Y, Shanks RA. *J. Appl. Polym. Sci.* 1996, 61, 1877-1885

[36] Gregor-Svetec D. *J. Appl. Polym. Sci.* 2000, 75, 1211-1220

[37] Joseph S, Thomas S. *J. Polym. Sci. Part B*, 2002, 40, 755-764

[38] Senuma A, *Nippon Gomu Kyokaishi* 2003, 76, 86-89

[39] Robeson LM, Merriam CN. *Macromolekulare Chemine* 1973, 29/30, 47-62

[40] Shackelford JF, Alexander W. Materials Science and Engineering Handbook, CRC Press, New York, 2001

[41] Feng Y, Hay JN. *J Applied Polym. Sci.* 1998, 69, 2089-2095

[42] Huang Y, Wu Y. *European Polymer Journal* 2005, 41, 2753-2760

[43] Hirata Y, Kotaka T. *Reports on Progress in Polymer Physics in Japan*, 1979, XXⅡ, 177-180

[44] Hirata Y, Kotaka T. *Polymer J.* 1981, 13, 3, 273-281

[45] Okabe Y, Saito H. *Polymer*, 2010, 51, 1494-1500
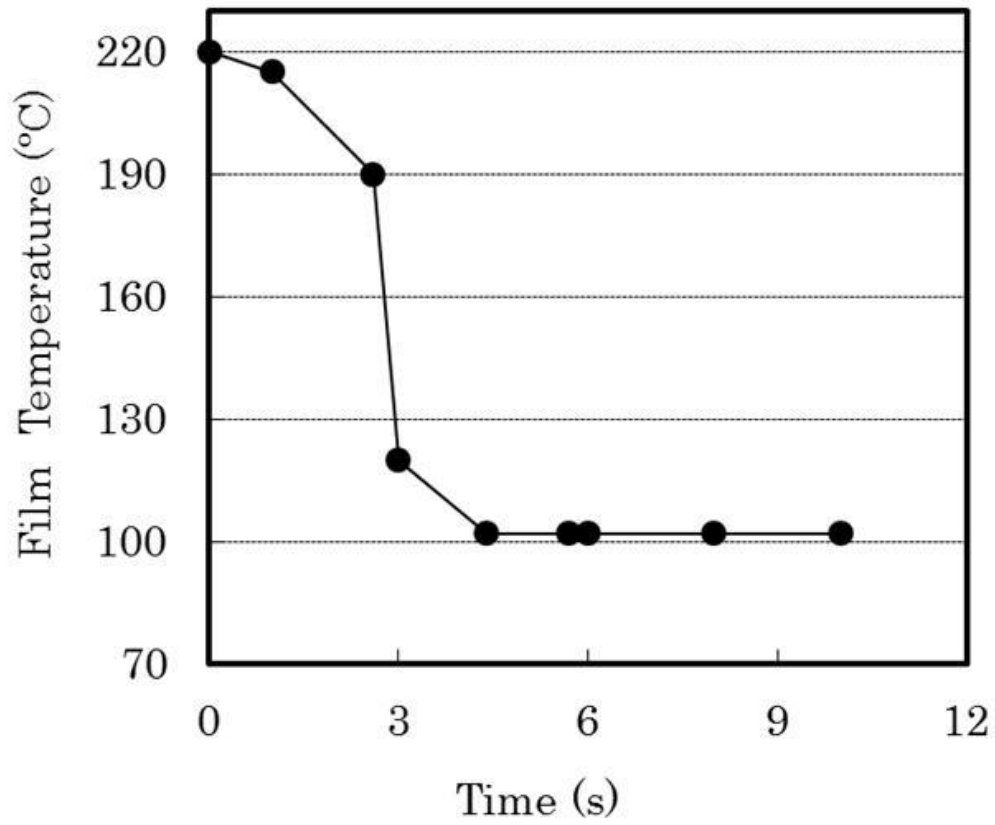
Figure 3-1　The film temperature profile during
the melt casting process.
(Chill roll temperature; 100 ºC)
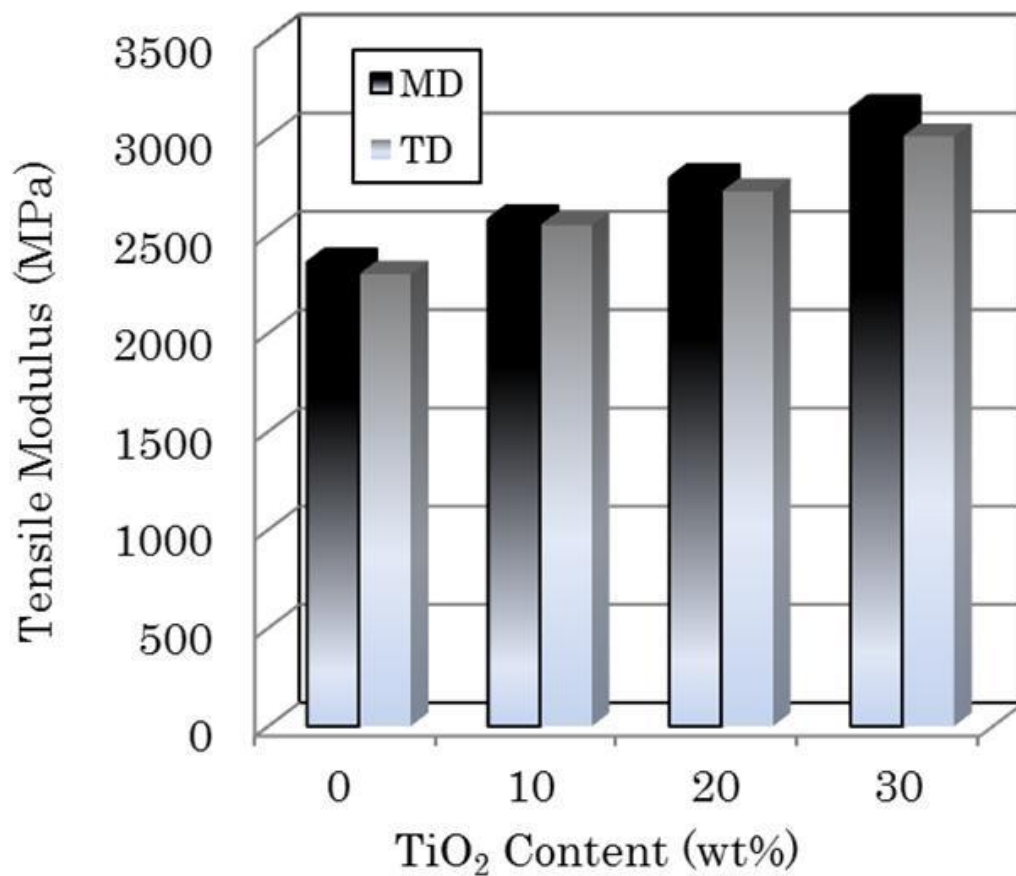
Figure 3-2　Tensile modulus of PVDF/PMMA/TiO$_2$ blend films with different TiO$_2$ contents.
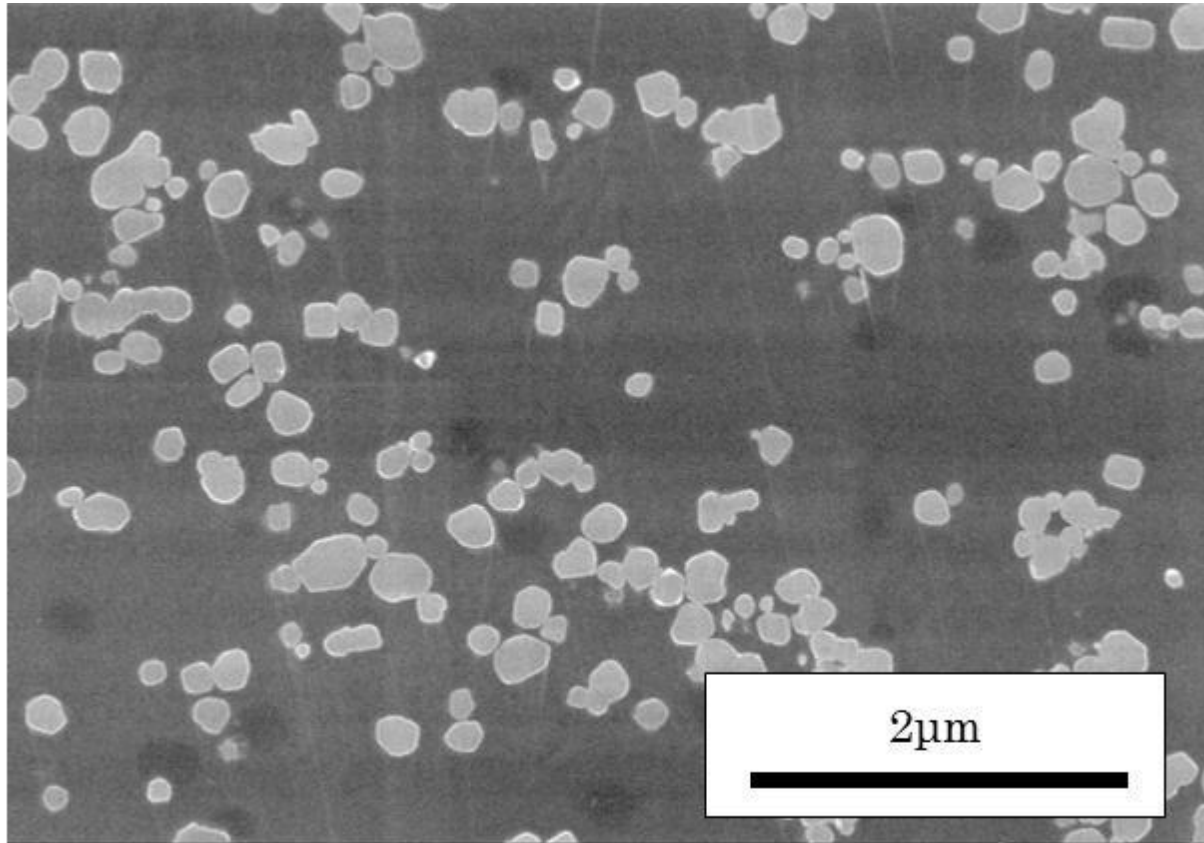
Figure 3-3　SEM micrograph of the cross section of PMTi-30.

61
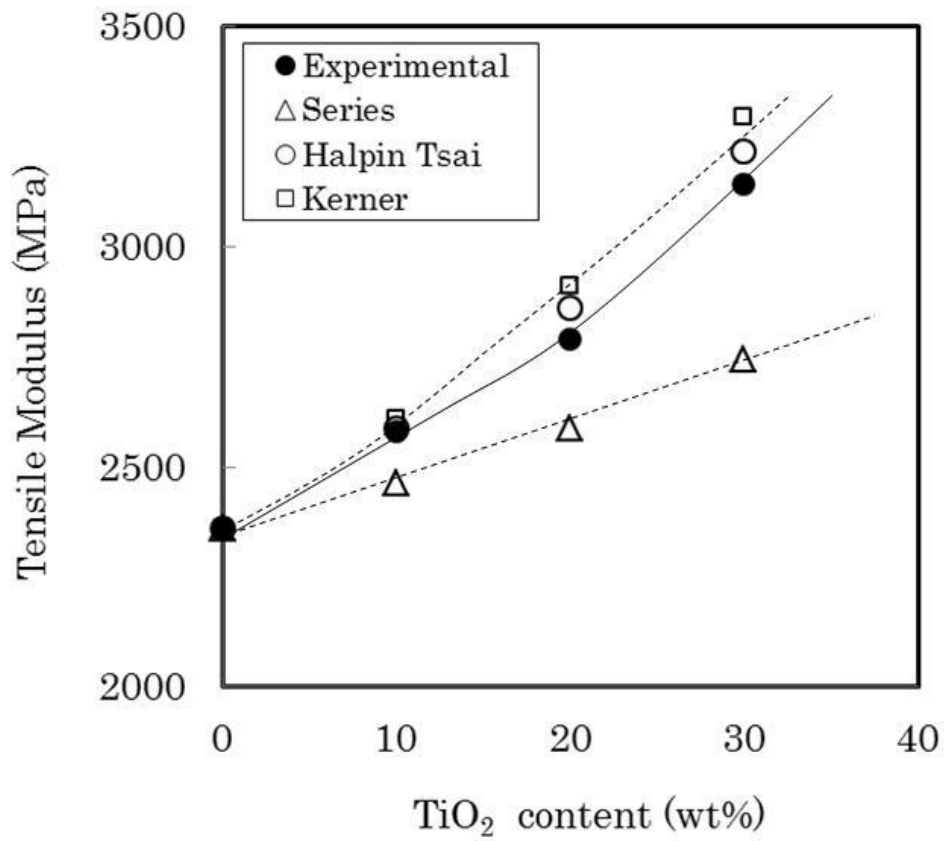
Figure 3-4   Comparison of the experimental tensile
modulus and theoretical prediction in machine
direction (MD) for PVDF/PMMA/TiO$_2$ blend films.
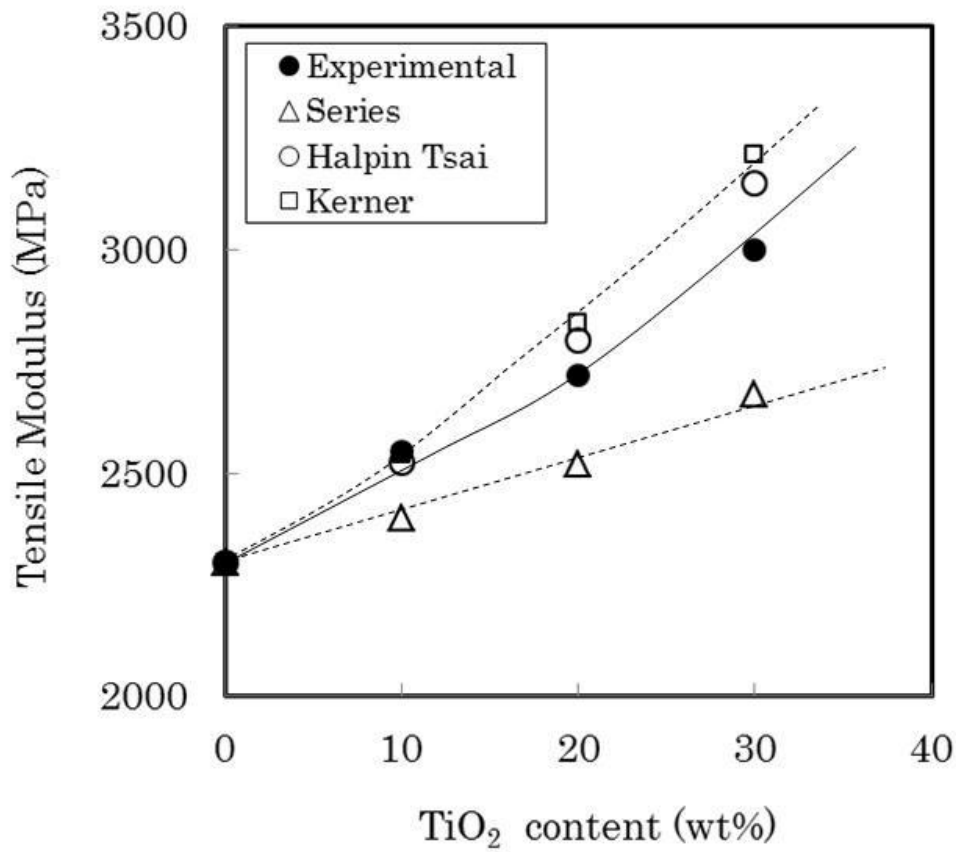
Figure 3-5　Comparison of the experimental tensile modulus and theoretical prediction in transverse direction (TD) for PVDF/PMMA/TiO$_2$ blend films.
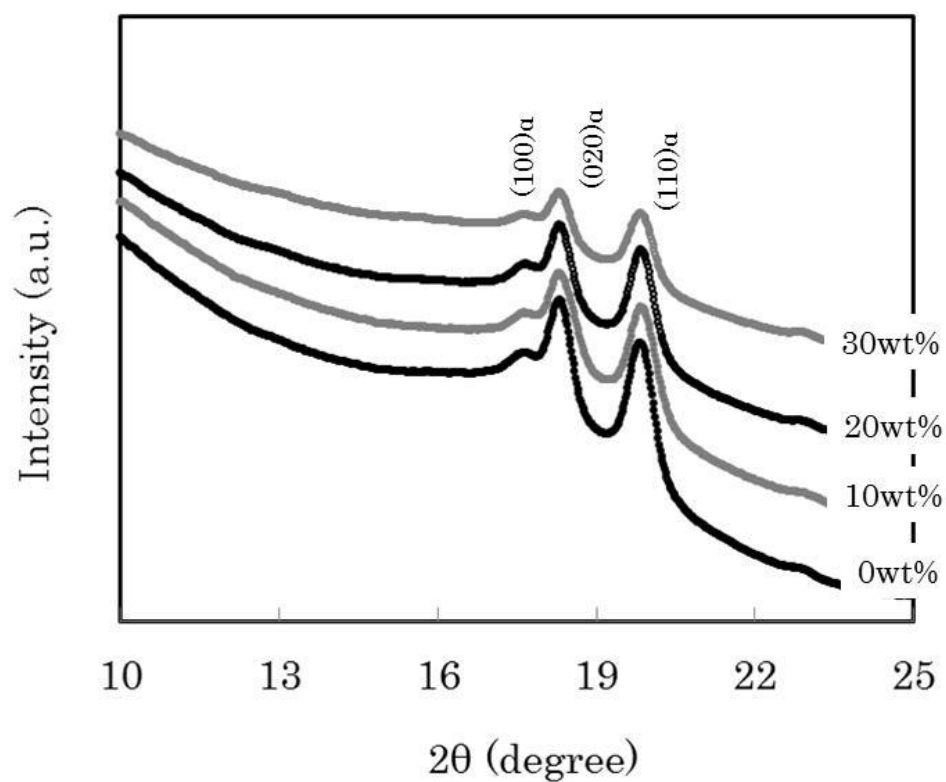
Figure 3-6　WAXD profiles of PVDF/PMMA/TiO$_2$ blend films with different TiO$_2$ contents.
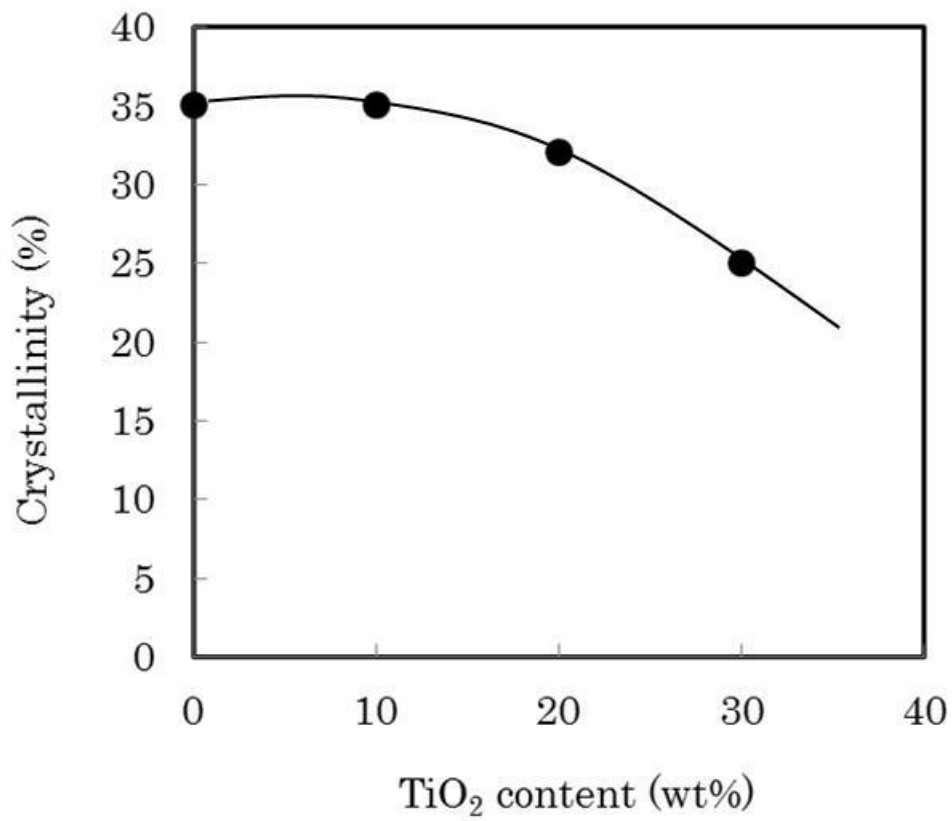
Figure 3-7　Crystallinity of PVDF/PMMA/TiO$_2$ blend films with different TiO$_2$ contents.
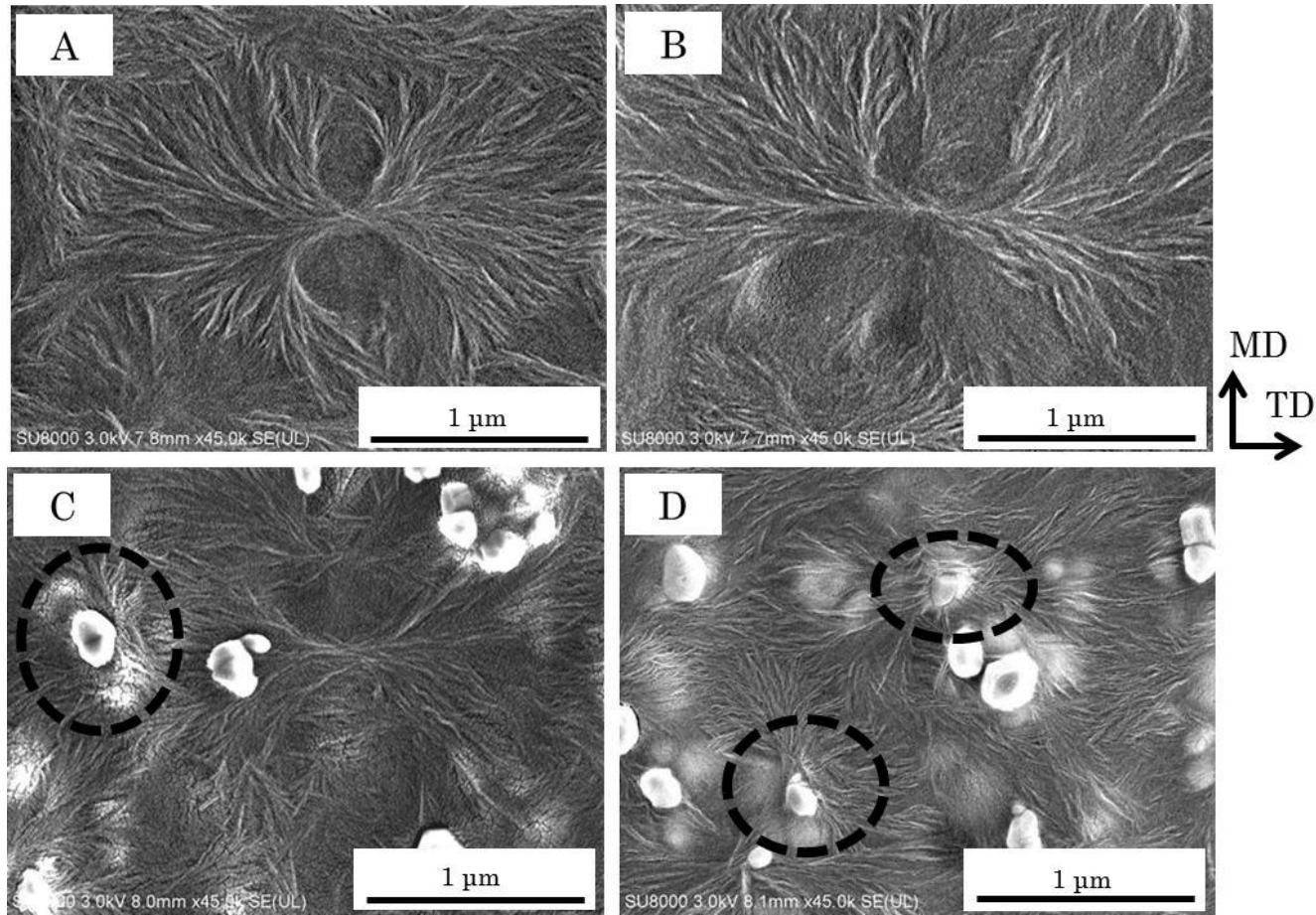
Figure 3-8   SEM micrographs of film surfaces: (A) chill roll side for
PMTi-0, (B) opposite side of chill roll for PMTi-0, (C) chill roll side for
PMTi-30, and (D) opposite side of chill roll for PMTi-30.
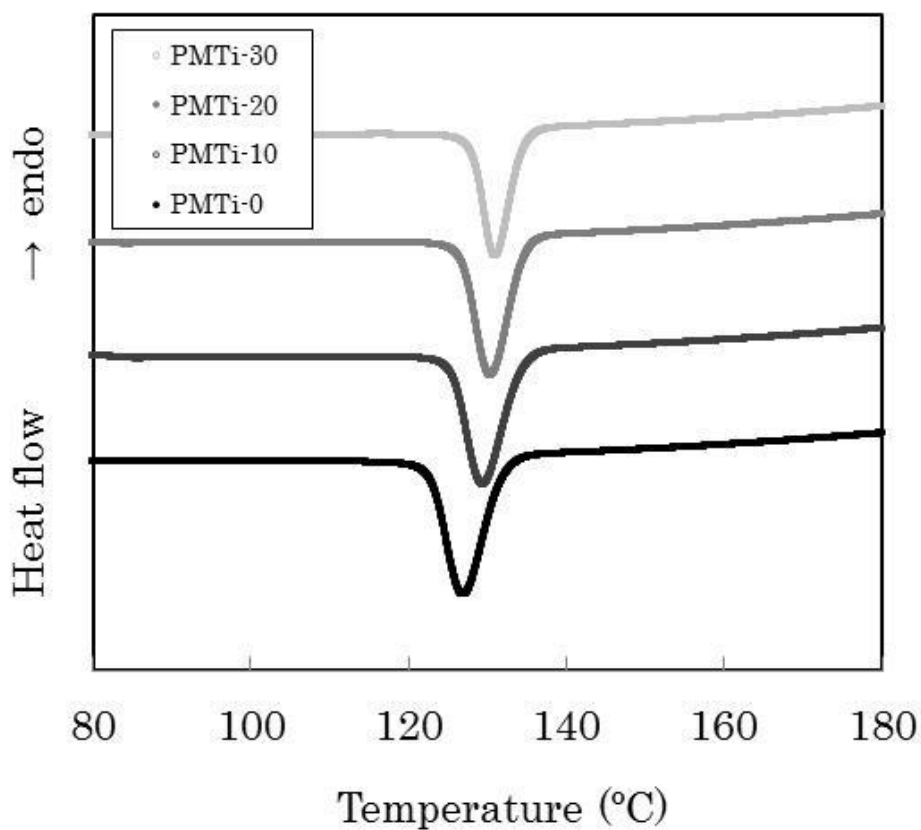
Figure 3-9 DSC thermograms of PVDF/PMMA/TiO$_2$ blend films with different TiO$_2$ contents for the cooling scan (Cooling rate = 20°C/min).
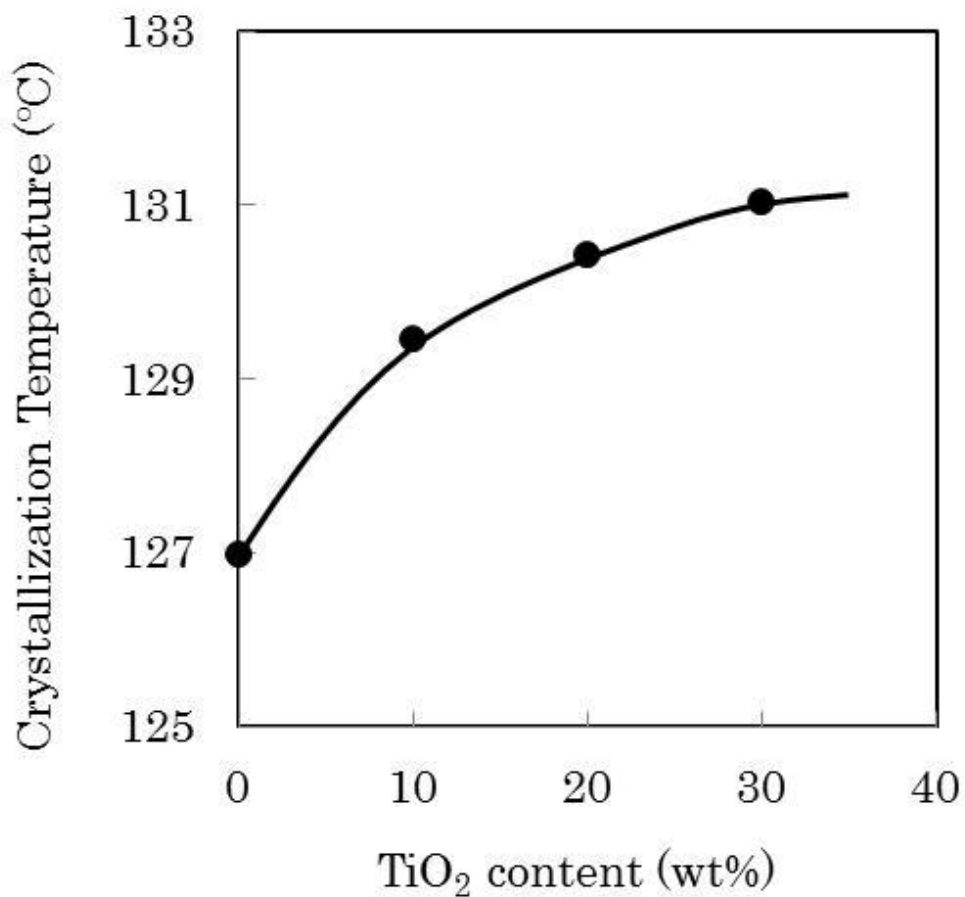
Figure 3-10 Dependence of crystallization
temperatures of PVDF/PMMA/TiO$_2$ blend films
with different TiO$_2$ contents on the cooling scan
(Cooling rate = 20°C/min).
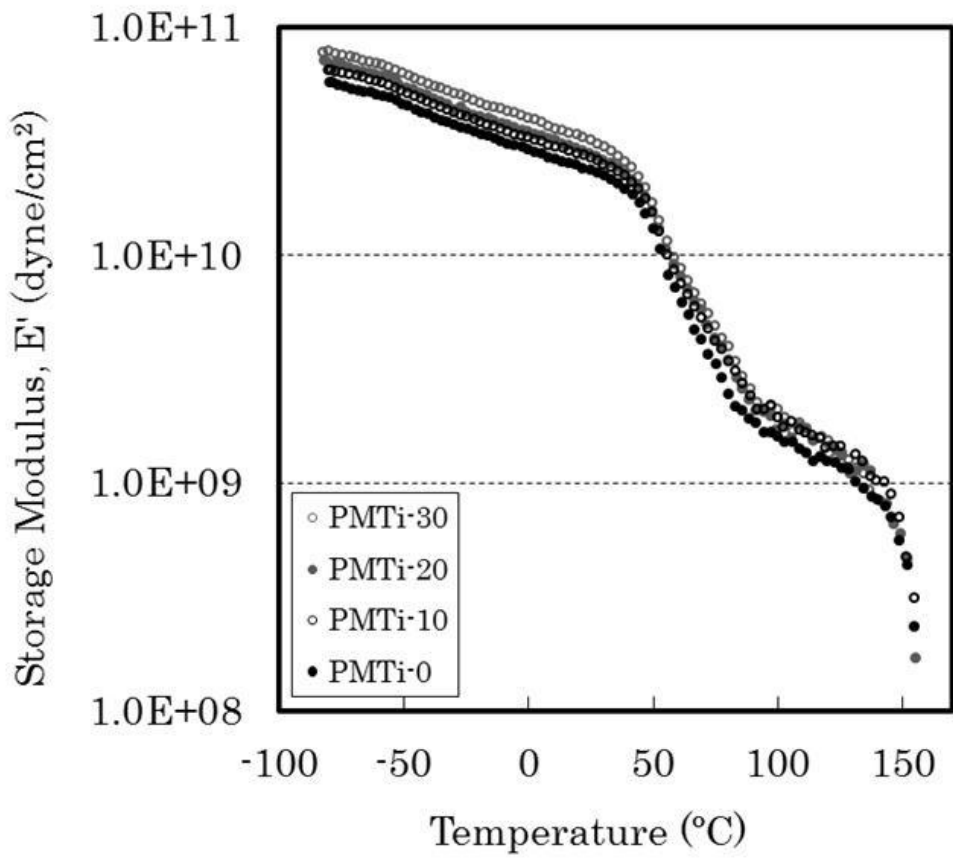
Figure 3-11 Temperature dependence of storage modulus, E', for PVDF/PMMA/TiO$_2$ blend films with different TiO$_2$ contents.
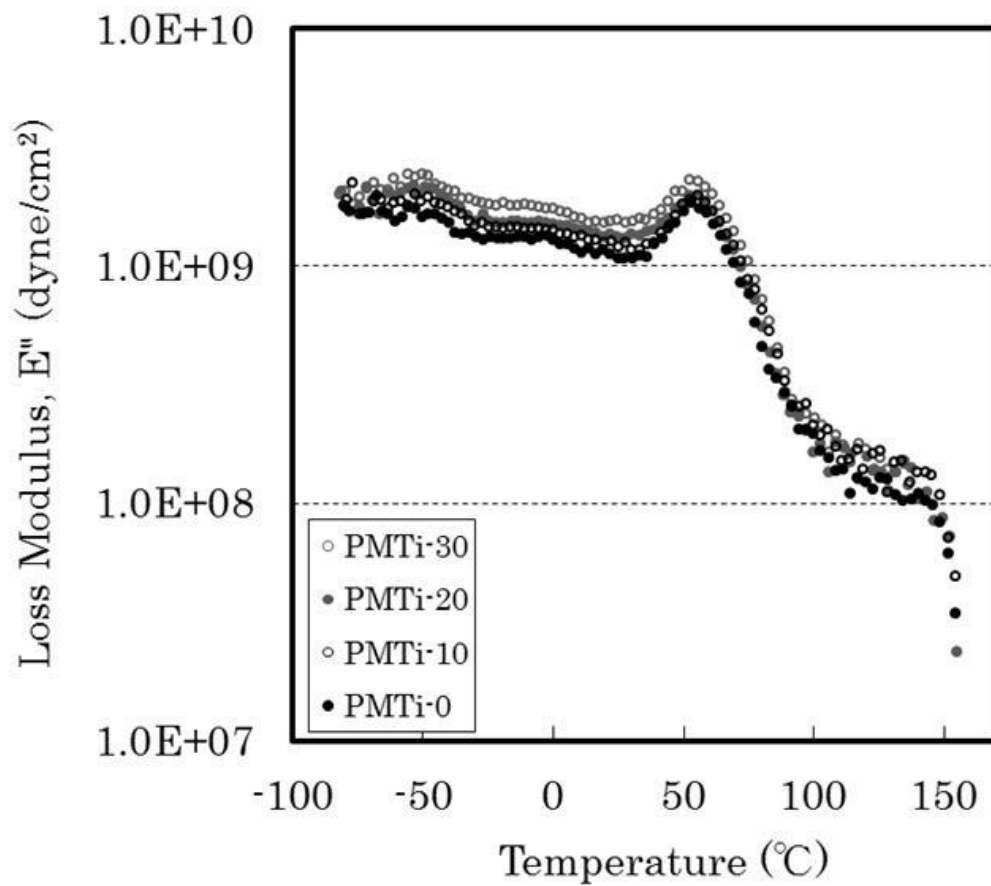
Figure 3-12　Temperature dependence of loss modulus, E", for PVDF/PMMA/TiO$_2$ blend films with different TiO$_2$ contents.
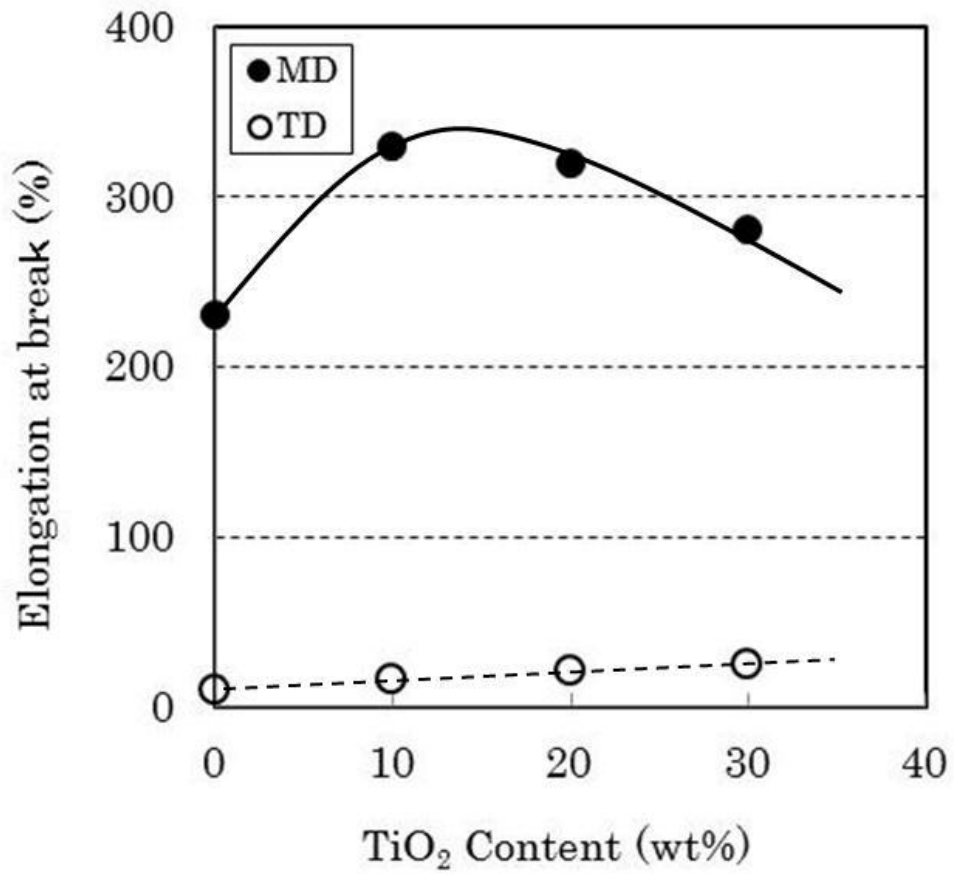
Figure 3-13　Elongation at break of
PVDF/PMMA/TiO$_2$ blend films with different TiO$_2$.
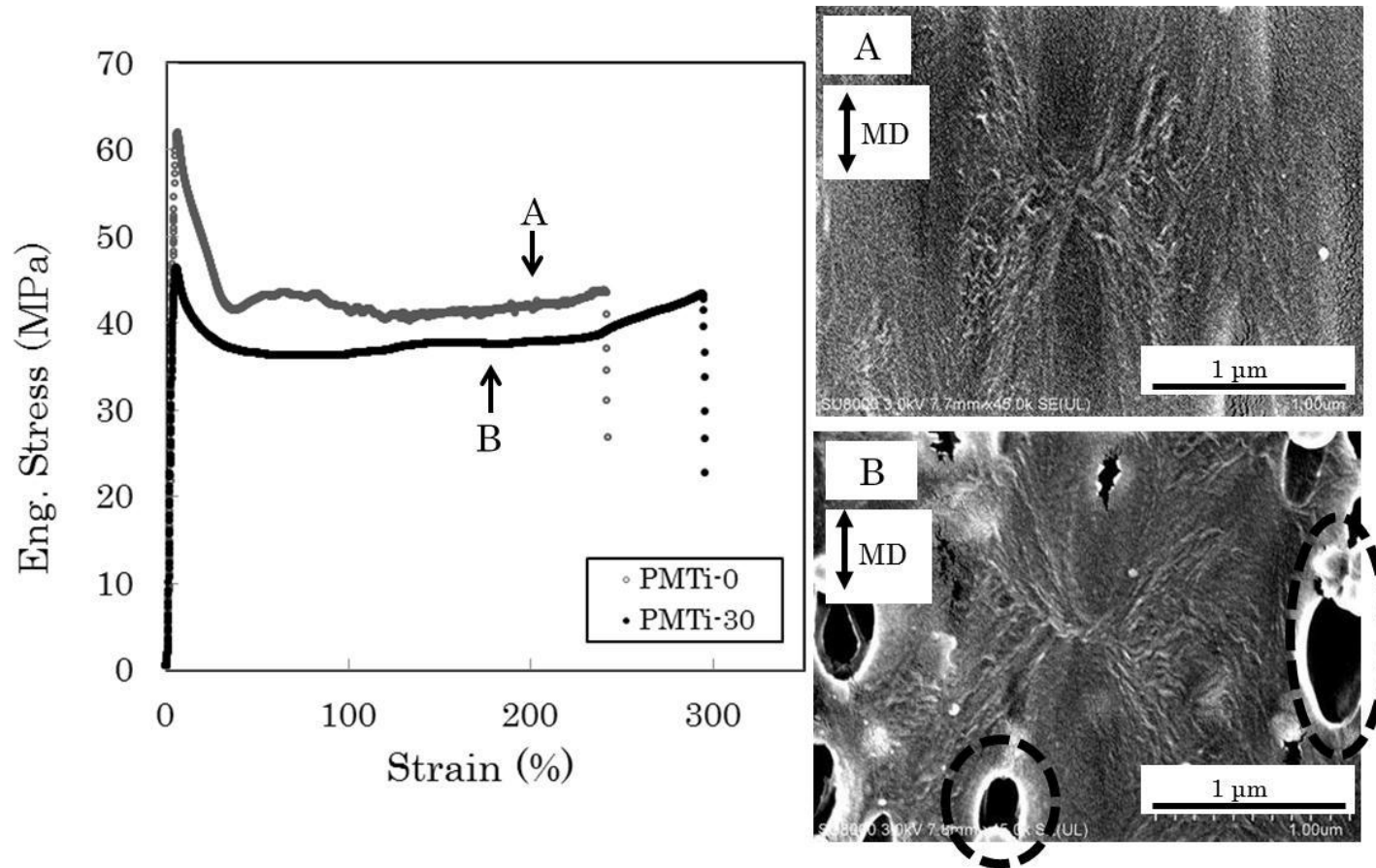
Figure 3-14　Engineering stress–strain curves for PMTi-0 and PMTi-30 in TD, and SEM micrographs of film surfaces: (A) 200% elongation of PMTi-0 and (B) 170% elongation of PMTi-30.
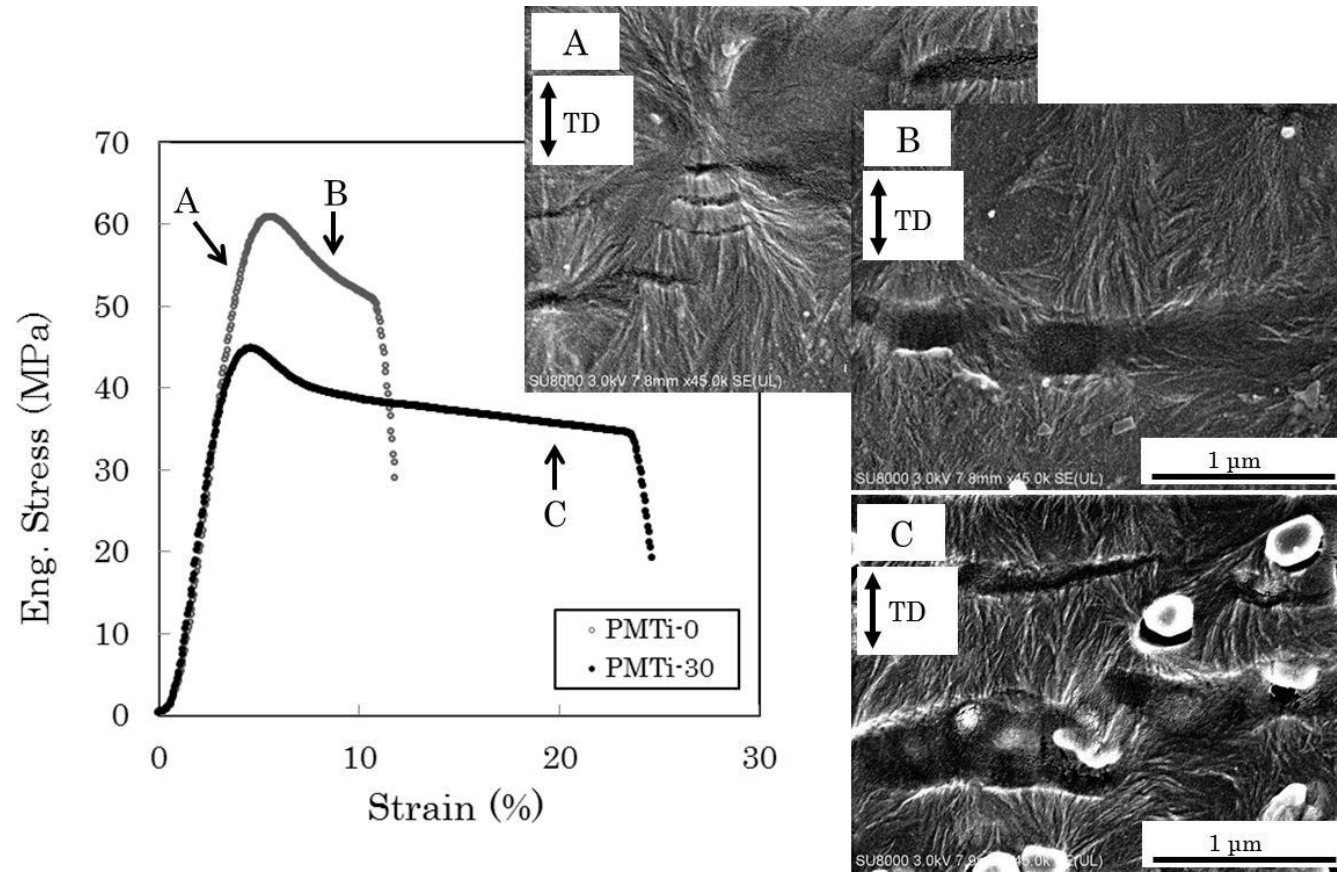
Figure 3-15　Engineering stress–strain curves for PMTi-0 and PMTi-30 in MD, and SEM micrographs of film surfaces: (A) 4% elongation of PMTi-0, (B) 8% elongation of PMTi-0, and (C) 20% elongation of PMTi-30.
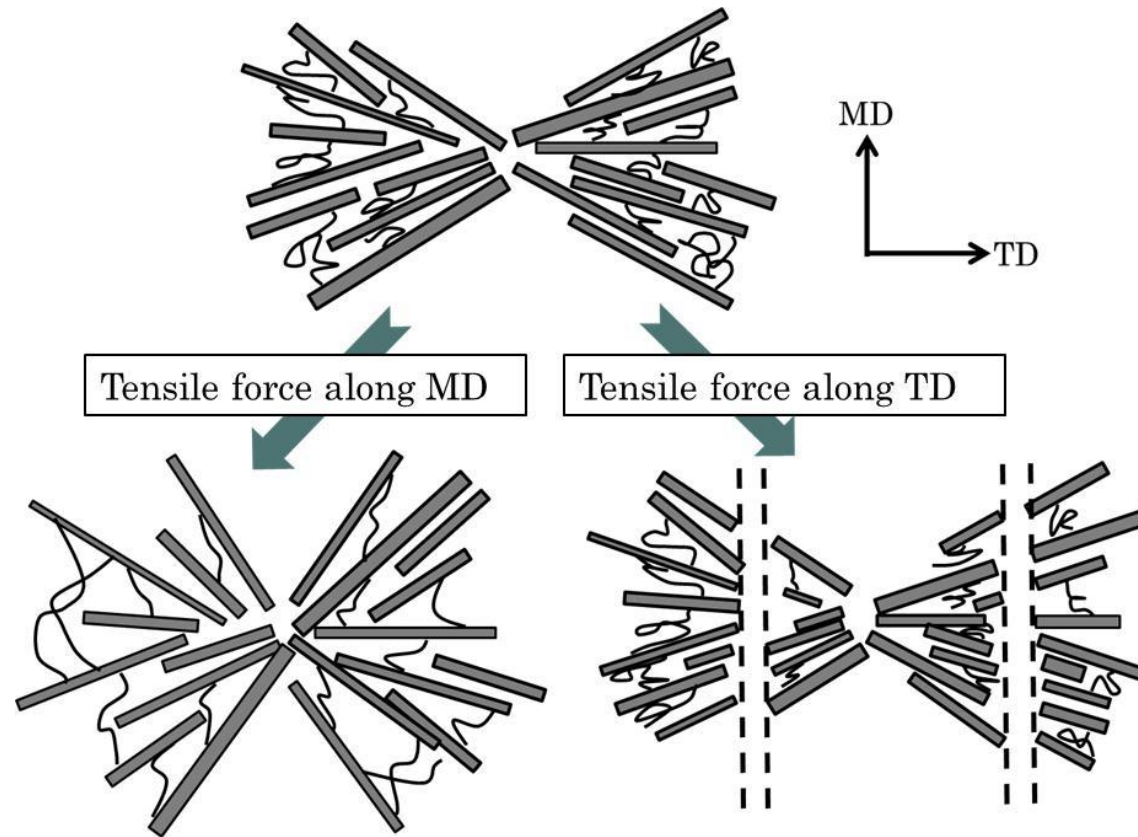
Figure 3-16 Schematic illustration at deformation
of spherulites under tensile force.

Chapter 4.

Morphological study of PVDF/PMMA/TiO₂ blend films prepared by melt casting process

4.1 Introduction

Poly(vinylidene fluoride) (PVDF) is a semicrystalline polymer that is widely used in industry because of its excellent mechanical properties, good chemical resistance, and superior resistance to severe environmental stress [1, 2]. Furthermore, many studies have been performed to improve other properties of this polymer. In a study on PVDF/graphite composites prepared by a solution precipitation method using N,N-dimethylformamide (DMF), it was reported that the storage modulus and dielectric constant of the composites linearly increased with graphite concentration. For example, when the graphite concentration was 10 wt%, the storage modulus at 20 °C and the dielectric constant at 104 Hz were approximately 83% and 93% higher, respectively, than those of pure PVDF [3]. The relationship between the physical properties (e.g., electrical conductivity and mechanical properties) and the morphology of a PVDF/polyamide 6 (PA6)/carbon nanotubes composite was investigated by Li et al. Their results showed that the formation of PA6 nanodomains in the PVDF phase by higher shear processing not only increased the electrical conductivity but also improved the ductility of the resulting blend nanocomposites [4]. Radiation grafted and sulfonated PVDF membranes were studied using thermal analysis and X-ray diffraction. It was assumed that the grafting took place mainly in the amorphous region of the PVDF membranes and close to the crystal surface, but the grafts did not penetrate into the crystals. The proton conductivity of the grafted and sulfonated PVDF membranes reached values comparable with those of Nafion membranes [5].

There are several reports on the polymer blends of PVDF and poly(methyl methacrylate) (PMMA). The general conclusion is that such systems exhibit lower critical solution temperature (LCST) behavior around 330°C. Therefore, these components are miscible in the amorphous state above the melting point of PVDF ($T_m \cong 170°C$), and PVDF crystallizes from the melt state below the T_m if the blend is maintained above its glass transition temperature (T_g) [6−13]. In particular,

several studies have described the mechanisms of phase separation induced by crystallization of PVDF in terms of the PVDF content in these composite materials. However, most of the attention has been given to their compatibility studies, and there are few studies on their property−morphology−processing relationships [14].

Dynamic mechanical measurements give useful information on the morphology of PVDF/PMMA blend materials [14−18]. Quenching the PVDF/PMMA blends forms an imperfect crystalline phase, pure semicrystalline PVDF domains similar to form II (α phase), and secondary relaxation of PMMA [16−18]. In addition, an increase in the relative ratio of PMMA to PVDF in amorphous regions of the blend gives rise to higher T_g values [14]. Furthermore, the morphology of the melt-mixed blends is different from that of the solution-mixed blends [17]. Phase separation that was not caused by crystallization of PVDF was suggested by Hirata et al. According to their reports, the LCST can take place at a temperature as low as or lower than 200°C for PVDF/PMMA blend materials in which the PVDF content is >60 wt%. In a different study, it was reported that thermal annealing and the existence of the appropriate initial morphology gave effects to microphase separation in a diblock copolymer, and thermal annealing minimized the free energy of the polymer chains [19]. Therefore, investigating the relationship between the annealing conditions and morphology provides useful information on the equilibrium morphology.

It is well known that PVDF can crystallize into at least four different crystal forms (α, β, γ, and δ) [20]. Crystallization of PVDF from melt states under slow cooling rates leads to the formation of two types of crystalline phases, α or γ, depending on the temperature. At crystallization temperatures below 423–428 K, only the α phase are obtained [21−23], whereas a mixture of the α and γ phase is obtained at higher temperatures [24−26]. Hsu and Geil et al. reported that the α phase changed into the β phase during drawing and further concluded that the transformation is strongly affected by the drawing temperature [27]. Furthermore, a solution-cast film obtained from dimethylacetamide under slow evaporation produced a γ phase [28]. Obviously, the crystalline phase of PVDF in PVDF/PMMA blend materials obtained from melt states depends on both cooling conditions and the blend ratio of PVDF/PMMA [28−30]. Horibe et al. found that melt-mixed blends of PVDF/PMMA (70/30–80/20, wt/wt) formed the β phase of PVDF on quenching and annealing at 120°C. They concluded that this was due to the slow rate of crystallization in the presence of PMMA under the appropriate crystallization temperature because the β phase is formed when PVDF crystallizes slowly [29−30].

In the experiment, they applied with ice water for the quench and room temperature for the slow cooling, respectively. However, they did not perform a detail investigation of the effect of cooling temperatures on the crystal structure of PVDF in PVDF/PMMA blend materials.

An inorganic material titanium dioxide (TiO_2) has received the most attention because of its excellent properties such as long-term stability, nontoxicity, and resistance to discoloration under UV light [31]. PVDF composite membranes with nanosized TiO_2 particles were studied by Cao et al. The small nanoparticles (average diameter: ~10 nm) improved the antifouling property of the PVDF membranes and had a substantial effect on the crystallization of PVDF [32]. Recently, it was reported that the addition of 10 wt% TiO_2 (primary diameter: 260–300 nm) to PVDF/PMMA (70/30, wt/wt) resulted in an improvement in the tensile strength and elongation at break while maintaining the good intrinsic thermal stability of the PVDF/PMMA composite [31]. Tang et al. studied the mechanical properties, crystal structure, and surface morphology of melt-mixed PVDF/PMMA/TiO_2 blown films developed for solar cell encapsulation. In their study, films containing PVDF at 70, 80, and 90 wt% exhibited co-existence of the α and β phase. Upon adding TiO_2 (15 wt%) to PVDF/PMMA blends (70/30, wt/wt), they found that the elongation at the break of the blown films greatly improved. These results show that PVDF/PMMA/TiO_2 blown films present good mechanical properties [33].

PVDF/PMMA/TiO_2 blend films are a prospective film for industrial use, and there are a few reports on the morphology and mechanical properties. However, there is limited investigation into the influence of casting conditions on morphology, although the chill roll temperature, which is a parameter of the melt casting process, is an important factor dominating the morphology, mechanical properties, and thermal stability of films. In addition, thermal annealing is a key factor controlling crystallinity and microphase separation. Therefore, we focused on a morphological study of PVDF/PMMA/TiO_2 blend films prepared by a melt casting process, in terms of the effects of the chill roll temperature and thermal annealing. The films were evaluated by using Fourier transform infrared spectroscopy (FT-IR), wide angle X-ray diffraction (WAXD), scanning electron microscopy (SEM), and dynamic mechanical analysis (DMA).

4.2 Experimental

4.2.1 Materials

The PVDF used in this study was supplied by Kureha Corporation (Japan) and the molecular weights were 194,000 (Mw) and 86,000 (Mn). The PMMA was purchased from Asahi Kasei Chemicals (Japan) and the molecular weights measured by gel-permeation chromatography were 130,000 (Mw) and 86,000 (Mn). The rutile TiO_2 particles (average diameter: ~290 nm) was purchased from DuPont (Wilmington, DE, USA).

4.2.2 Film preparation

PVDF/PMMA/TiO_2 blend films were prepared by a melt casting process with a slit die. The composition of PVDF/PMMA/TiO_2 was fixed at the weight ratio of 56:14:30. The composite materials of PVDF/PMMA/TiO_2 were first pelletized by using a twin screw extruder. After obtaining pellets, films (20 µm in thickness) were extruded and cast at different chill roll temperatures. The barrel temperature was 240°C, the width of the slit die was 270 mm, and the die gap was 0.5 mm. The shear rate was calculated to be 39 s^{-1} from the extrusion output of 3.1 kg h^{-1}, density of 2.0 g cm^{-3} of the blend material, and die size. Different chill roll temperatures of 30, 50, 78, 90, 110, and 115°C were applied in this study. The corresponding films were coded as Ch30, Ch50, Ch78, Ch90, Ch110, and Ch115, respectively. Ch30 and Ch115 were annealed at 115°C for 24 h and coded as Ch30−AN and Ch115−AN, respectively.

4.2.3 Measurement

The film surface temperature during the melt casting process was measured by a contact thermometer. The measured area was not evaluated in this study because its appearance was insufficient. In this study, chill roll temperature refers to the surface temperature of the chill roll measured by a contact thermometer.

FT-IR spectra were obtained using a SPECTRUM 2000 instrument (Perkin−Elmer Inc., Waltham, MA, USA) in the range of 900–700 cm^{-1} (resolution: 8 cm^{-1}, number of scans: 8) at room temperature.

WAXD measurements were performed using a NANO-Viewer system (Rigaku Co.,

Japan). Cu–Kα radiation (40 kV, 40 mA) was generated and collimated by a confocal mirror system. The wavelength and the camera length were 1.54 Å and 70 mm, respectively. An imaging plate (IP; BAS-SR 127; Fujifilm Co., Japan) was used as a two-dimensional detector, and the IP reading device RAXIA-Di (Rigaku Co.) was employed to transform the obtained image into text data.

The morphology of the film surfaces was observed using SEM (model SE8020, Hitachi Hightechnologies Co., Japan) with the accelerating voltage of 3 kV after coating platinum particles under vacuum-dried conditions.

DMA measurements were conducted by using an RSA-3 device (TA Instruments Inc., New castle, DE, USA) at the heating rate of 2 °C min^{-1}. The frequency was 10 Hz and the temperature range was from −80°C to 120°C.

4.3   Results and Discussion

4.3.1   Film temperature during the melt casting process

Figure 4-1 shows the film temperature profile during the melt casting process at the chill roll temperature of 30°C. Zero seconds on the x axis refers to the time at which the molten material just begins to flow from the die gap. As seen the figure, a rapid decrease in the film temperature begins at 2.6 s because the molten material contacted the chill roll at this time. It was found that the film temperature reached 32°C at 4.2 s. The film was pealed from the chill roll after casting for 10 s. This result indicates that the cooling system is sufficient for allowing the films to reach the chill roll temperature. We confirmed that the film temperature attained the chill roll temperature in a series of experiments by using a chill roll at different temperatures such as 30, 50, 78, 90, 100, and 115°C.

4.3.2   Effect of chill roll temperature on crystal structures

Figure 4-2 shows the FT-IR spectra of films cast at different chill roll temperatures. It can be clearly seen that the transmittance at 845 cm^{-1} decreases, whereas those at 767, 798, and 856 cm^{-1} increase with increasing chill roll temperature. The peak at 845 cm^{-1} seen in the Ch30 spectrum is ascribed to the β phase, and those at 767, 798, and 856 cm^{-1} seen in Ch115 are ascribed to the α phase [34, 35]. With increasing chill roll temperature, the intensity of the β phase peak decreased, and

that of the α phase peaks increased. From the results, it was revealed that the β phase was formed when the chill roll temperature was 30°C, and the crystalline phase changed to the α phase with increasing chill roll temperature. The relative fraction of the β phase, denoted as F(β), in films containing both α and β phase can be calculated by equation (1) [3, 4]:

$$F(\beta) = \frac{A_\beta}{1.3A_\alpha + A_\beta} \tag{1}$$

where A_α and A_β are the absorbences at 767 and 840 cm^{-1}, respectively. The relationship between F(β), calculated from equation (1), and the chill roll temperature is shown in Figure 4-3. The F(β) value for Ch30 was 0.91, whereas Ch50 not only had the F(β) value of 0.61 but also had the α phase fraction of 0.39. When the chill roll temperature was above 78 °C, the α phase fraction increased to greater than approximately 0.9.

The crystal structures and crystallinity were investigated using WAXD measurements. The direction of the incident X-ray was as follows: through, perpendicular to the plane of the film; edge, parallel to the plane of the film and perpendicular to the MD of the film; and end, parallel to both plane and MD of the film.

It is well known that PVDF has at least four different crystal forms, α, β, γ, and σ, as mentioned above. The α phase has a trans–gauche–trance–gauche′ (tgtg′) backbone, forming a monoclinic (pseudo-orthorhombic) unit cell with the following dimensions: a=0.496 nm, b=0.964 nm, and c (chain direction)=0.462 nm, and all unit-cell angles equal 90°. The β phase has an all-trans backbone consisting of nearly planar zigzag chains packed in an orthorhombic unit cell having the following dimensions: a=0.858 nm, b=0.491 nm, and c=0.256 nm [2, 35, 36]. The unit cell of the γ phase is orthorhombic (dimensions: a=0.497 nm, b=0.966 nm, and c=0.918 nm). The chain formation tttgtttg′ has been previously reported [36−38]. Figure 4-4 shows two-dimensional diffraction images observed from each direction of the incident x-ray. Each image shows a single concentric diffraction ring having strong intensity. The diffraction ring is ascribed to the (110) plane of rutile TiO$_2$ particles [32]. The diffraction images seen inside the ring are ascribed to the PVDF crystalline phase.

The WAXD profiles calculated from the whole scan of the end-view image are represented in Figure 4-5. Regardless of the direction of the incident x-ray to films, similar WAXD profiles were confirmed, namely the peak positions observed in the

through-view and edge-view images were the same as that in the end-view images. Ch78, Ch90, Ch100, and Ch115 had peaks at 2θ of 17.7°, 18.4°, and 20.0°, and these peaks correspond to the α phase Bragg diffraction of (110), (020), and (110), respectively [32, 33]. On the other hand, the peak at 20.4° seen in Ch30 corresponds to (200) and (110) of the β phase [32, 33]. The peak position shifted slightly to a higher diffraction angle in Ch50 owing to the coexistence of the α and β phase. The results obtained from the WAXD measurements were consistent with the interpretation based on the FT-IR measurements. In the previous study, it was revealed that the β phase in the presence of PMMA was formed when PVDF/PMMA (70/30–80/20, wt/wt) blends were melted, quenched by ice water, and annealed at 120 °C for 800 h. In contrast, slow cooling at room temperature from the melt state has been shown to produce the α phase [29, 30]. Therefore, our results with respect to the crystalline phases formed at different chill roll temperatures exhibited crystalline transitions similar to those of the previous study. In addition, the effect of adding 10 wt% TiO_2 to PVDF/PMMA (70/30, wt/wt) on the crystallization of PVDF in the resulting PVDF/PMMA/TiO_2 blend films was also previously investigated, and the results showed that the presence of TiO_2 in PVDF/PMMA did not change the crystalline phase of PVDF [32]. Our results also suggest that TiO_2 has little effect on the crystal structures of PVDF, even though 30 wt% TiO_2 was used in our experiments.

In addition, the intensity along the meridian in the through- and edge-view diffraction images of Ch78, Ch90, Ch100, and Ch115 in Figure 4-4, ascribed to (100), (020), and (110) of the α phase was weak. Because these planes are parallel to the molecular chains of PVDF, it suggests that these chains are oriented along the MD of the film. This is probably due to the shear flow field caused by the melt casting process with the slit die. However, the concentric diffraction ring assigned to the PVDF crystals in the through- and edge-view images of the films cast using a chill roll temperature below 78°C was observed . This represents a nonorientated state. It has been considered that because the growth rate of the crystal of PVDF is slow below 78°C, relaxation of the PVDF chains might occur during the casting process.

From these results, it was revealed that the transition temperature of crystal structures of PVDF/PMMA/TiO_2 (80/20/30, wt/wt/wt) blend films prepared by a melt casting process with a slit die is approximately 50°C.

Figure 4-6 shows the dependence of crystallinity on the chill roll temperature, as calculated by equation (2):

$$Xc\ (\%)\ =\ \frac{A_c}{A_\alpha\ +\ A_c}\ \times\ 100 \tag{2}$$

where A_c is the area of the crystalline phase and A_α is the area of the amorphous phase in the WAXD profiles presented in Figure 4-5. As seen in Figure 4-6, crystallinity increased with chill roll temperature: the crystallinity of Ch30 was 28.7%, and that of Ch115 was 44.7%.

The β phase of PVDF is formed when PVDF slowly crystallized, and the α phase is formed under rapid crystallization [29−30]. Therefore, the reason Ch30 exhibited low crystallinity in our experiment was that the PVDF in Ch30 did not sufficiently crystallize during the casting process.

4.3.3　Effect of morphology on dynamic mechanical behavior

In this section, the relationship between the morphology and dynamic mechanical behavior is described. To eliminate the effect of molecular orientation, tensile force in DMA measurements was applied along the transverse direction (TD) of films. TD is perpendicular to the machine direction in the melt casting system.

Figure 4-7 shows plots of the storage modulus (E′) versus temperature. As seen in Figure 4-7, the values of E′ increased with increasing chill roll temperature over the entire temperature range. Figure 4-8 denotes plots of the loss modulus (E″) versus temperature, and the curves are slightly shifted along the Y axis to distinguish each curve in the figure. All samples exhibited a peak at approximately 55 °C, and the peak temperature did not significantly change under different chill roll temperatures. In addition, a small peak was observed at approximately −40 °C for all samples.

Hirata et al. clearly defined the E″ peaks for the melt-mixed PVDF/PMMA blends. They suggested that there is a four-phase morphology in the melt-mixed PVDF/PMMA blend materials and that the PVDF content is >60 wt% [16, 17]. The four-phase morphology composed of a mixed amorphous phase with $T_g \approx 55°C$, an amorphous PVDF phase with $T_g \approx -40°C$, an imperfect crystalline phase, and a nearly pure PVDF crystalline phase. It was also reported that T_g assigned to the mixed amorphous phase in the binary polymer blend of PVDF and PMMA does not significantly vary over a range of compositions (PVDF/PMMA: 90/10–60/40, wt/wt) [14−15, 18].

Based on previous studies, the peak observed near 55°C was attributed to the mixed amorphous phase, and that near −40°C was attributed to the amorphous PVDF phase for the films obtained in our experiments. Although PVDF/PMMA/TiO$_2$ (80/20/30, wt/wt/wt) blend films were prepared in a shear flow field and contained 30 wt% TiO$_2$, the interpretation of the dynamic mechanical behavior suggested in the previous studies is very consistent with our results. Therefore, the result implies that TiO$_2$ has little effect on not only the crystal structures of PVDF but also the structures of the mixed amorphous regions.

As seen in Figure 4-7, a sharp decrease in E′ occurred in the temperature region above approximately 50°C for all samples. The decrement above 50°C in E′ became smaller as the chill roll temperature increased. However, the inflection temperature, which corresponds to T$_g$ ascribed to the mixed amorphous phase (~50°C), hardly changed under different chill roll temperatures. It is expected that the decrement in E′ above T$_g$ was caused by differences in the crystallinity of the films, so we annealed Ch30 and Ch115 at 115°C for 24 h in order to increase the crystallinity.

The crystal structures and crystallinities are shown in Table 1. Figure 4-9 represents the WAXD profiles calculated from the end view of both unannealed and annealed films. It was identified that Ch30 and Ch115 maintained the β and α phase, respectively, after annealing. On the contrary, the crystallinity in Ch30 remarkably increased to 58.4% from 28.7%, whereas that in Ch115 slightly increased to 48.0% from 44.7% by annealing. The small change in the crystallinity of Ch115 caused by the annealing process suggests that most of the crystallization occurred during the melt casting process. In contrast, the crystallinity of Ch30 had a small value (28.7%) before annealing because crystallization was not sufficiently promoted in the melt casting process. These results are owing to a slower growth rate for β phase compared with that for the α phase, as mentioned above.

Figure 4-10 shows the temperature dependence of E′ for Ch30−AN and Ch115−AN. For comparison, the E′ curves of Ch30 and Ch115 from Figure 4-7 are also shown. Figure 4-11 shows the temperature dependence of E″ for Ch30−AN and Ch115−AN. For comparison, the E″ curves of Ch30 and Ch115 from Figure 4-8 are also shown.

As seen in Figure 4-10, for Ch115 and Ch115−AN, the inflection temperature at which E′ begins to decrease slightly shifted to a higher temperature after annealing, and the values of E′ in the high temperature range from 50 to 120°C slightly increased on account of the annealing process. Figure 4-11 shows that the peak

ascribed to the mixed amorphous phase in Ch115, which represents T_g, shifted to a higher temperature by approximately 10°C on annealing at 115°C for 24 h. There are two reasons to be considered for explaining the behavior of E' in the temperature range from 50 to 120°C and the shift of the T_g observed in the E''. One is the slight increase in the PMMA fraction (from 31.1% to 32.5%) in the mixed amorphous phase by crystallization, as seen in Table 1. The other reason is that the crystalline regions act as physical cross links and that they are expected to restrict the onset of molecular motion in amorphous regions [14].

Comparing Ch30 and Ch30−AN, it was observed that the inflection temperature shifted to a higher temperature by approximately 10°C as a result of annealing at 115°C for 24 h, as seen in Figure 4-10. However, the behavior of E' for Ch30-AN in the temperature region above 50°C was not close to that of Ch115, although the crystallinity became 58.4%. Therefore, the difference in the E' curves of Ch30 and Ch115 in the temperature region above 50°C is not caused by variation in crystallinity but by other factors, which are subsequently described.

Table 1 shows the weight fractions of amorphous PVDF and PMMA, calculated from the crystallinity. As mentioned above, the decrement in the E' value of Ch115 above the T_g attributed to the mixed amorphous phase was less than that of Ch30 in the same temperature region. According to previous reports on PVDF/PMMA melt blends, E' in the region above T_g causes a small decrease with the decrease of weight fractions of PMMA in the materials [15-17]. Therefore, we deduced that the actual weight fraction of PMMA in the mixed amorphous phase of Ch115 is lower than that in Ch30. However, the weight fraction of PMMA calculated from the crystallinity of Ch115 is 31.1%. The value is higher than the one calculated from the crystallinity of Ch30 (26.0%). This result is inconsistent with the fact that, in the temperature region above T_g, the decrement in the E' value of Ch115 is less than that of Ch30. Judging from these results, we inferred that the actual weight fraction of PMMA in Ch115 is lower than that in Ch30. In addition, Okabe and Saito reported that amorphous pockets are formed in the region between the bundles of lamellar stacks in spherulite and that the excluded PMMA existed in the amorphous pockets [39]. In another study, it was reported that an amorphous component was entrapped within the inter-lamellar region as an amorphous phase for poly(ε-caprolactone)-poly(vinyl chloride) (PCL/PVC) blends [40]. Based on the previous suggestions, it was speculated that a large amount of PMMA can be entrapped within the interlamellar region formed in Ch115 if spherulites are present.

Figure 4-12 shows the SEM micrographs of the film surfaces of both chill roll side and the opposite one of the chill roll for Ch30 and Ch115. Many spherulites can be clearly seen in the micrographs of both sides for Ch115, and the two micrographs are almost the same. On the other hand, the SEM micrographs of Ch30 show TiO_2 particles and the polymer matrix. Therefore, it was suggested that the excluded PMMA became entrapped within the interlamellar region in the spherulites for Ch115. A process may readily occur owing to the rapid growth rate of the α phase. As a result, although the calculated weight fraction of PMMA in the mixed amorphous phase in Ch115 is 31.1%, it is deduced that the actual weight fraction of PMMA in Ch115 is lower than 26.0%, which is the calculated value for Ch30. This interpretation clearly explains the behavior of E′ in the temperature region above T_g.

By annealing, the weight fraction of PMMA in the mixed amorphous phase in Ch30 increased to 37.5% from 26.0% because the annealing process promoted crystallization. Thus, the larger decrease in the E′ value of Ch30−AN above approximately 50°C resulted from an increase in the weight fraction of PMMA, and the shift in the inflection temperature of E′ to a higher temperature was due to the same effect. No spherulite was observed in Ch30−AN, as seen Figure 4-13, although the film had high crystallinity (58.7%). This is probably because many tiny crystals uniformly exist in the film. Therefore, it was considered that entrapment of the excluded PMMA within the interlamellar region did not occur during annealing because of the slow growth rate of the β phase in Ch30. From these results, it is concluded that the difference in the dynamic mechanical behavior of Ch30 and Ch115 in the high temperature region above T_g is due to morphological differences.

On careful study of the E″ curves of Ch30 and Ch30−AN in Figure 4-11, it was observed that the intensity of the peak seen near −40 °C ascribed to the amorphous phase of pure PVDF increased by annealing. In general, blend materials of PVDF and PMMA exhibit LCST behavior at approximately 330°C and are molecularly miscible in the amorphous state [6−13]. Hirata et al. studied the dynamic mechanical behavior of PVDF/PMMA (72/28 and 95/5, wt/wt) blend materials. Their results showed that the T_g of the film obtained from a solution-casting method using DMF was close to that of the press sheet obtained from a melt-mixed blend after annealing the solution-cast film. Eventually, after annealing for 3400 min at 200°C, the T_g of the blend material obtained by the solution casting method nearly coincided with that of the press sheet. In addition, the intensity of the peak

near −40°C increased upon annealing [16, 17]. Based on these results, they suggested that the LCST for the melt-mixed PVDF/PMA blend materials might occur as low as or lower than 200°C [17]. As seen in Figure 4-11, a slight increase in the intensity of the peak at approximately −40°C was observed for Ch30. This is due to the increase in the extent of the pure amorphous PVDF phase. Specifically, it is inferred that annealing at 115°C promotes not only an increase in the weight fraction of PMMA in Ch30, resulting from crystallization of PVDF, but also phase separation in this particular system.

4.4　Conclusion

PVDF/PMMA/TiO$_2$ (80/20/30, wt/wt/wt) blend films were prepared by a melt casting process, and their morphology and dynamic mechanical behavior were studied as a function of the chill roll temperature and thermal annealing by using FT-IR , WAXD, SEM, and DMA. It was found that the crystal structure of PVDF changed from the ß phase to the α phase with increasing chill roll temperature. Specifically, the ß phase of PVDF was formed in Ch30, and coexistence of both α and ß phase was observed in Ch50. In addition, the α phase was produced when the chill roll temperature was above 78°C. Consistent with previous reports, our results showed that TiO$_2$ had little effect on the crystal structures of PVDF.

Crystallinity increased with the increase of chill roll temperature. The crystallinity of Ch30 was 28.7% and that of Ch115 was 44.7%. The reason why Ch30 exhibited low crystallinity in the experiment is that PVDF in Ch30 did not sufficiently crystallize during the casting process because the growth rate of the ß phase was slower than that of the α phase. The crystalline phase in Ch30 and Ch115 was maintained on thermal annealing at 115°C for 24 h.

A small decrement in E′ occurred in the temperature region above the T$_g$ ascribed to the mixed amorphous phase in the films, as the chill roll temperature increased. This was not due to the crystallinity. Comparing Ch115 and Ch30, we determined that the calculated weight fraction of PMMA in Ch115 is higher than that in Ch30, and it was observed that the decrement in E′ above T$_g$ for Ch115 is lower than that of Ch30. Based on the previous studies, we deduced that the actual weight fraction of PMMA in Ch115 is lower than that in Ch30. From the morphological studies, it was suggested that a large amount of PMMA is entrapped within the interlamellar region in the spherulites in Ch115. Entrapment of the excluded PMMA can readily occur because the growth rate of the α phase is fast. On the contrary, in Ch30, PMMA uniformly exists in the mixed amorphous phase because of the slow growth rate of the ß phase. The morphological observations strongly support our deduction. In addition, it was implied that promotion of microphase separation is caused by annealing at 115°C for 24 h.

4.5 References

[1] McCarthy, R. A., *Encyclopedia of Polymer Science and Engineering*, Vol. 3, ed., John Wiley, New York, 1985.

[2] Scheinbeim J. I., *Polymer Data Handbook*, 1999, Oxford Univ. Press

[3] He F., Fan J., *Polymer Testing*, 2008, 27, 964

[4] LI Y., Shimizu H., *Macromolecules*, 2008, 41, 5339

[5] Hietala S., Holmberg S., *J. Mater. Chem.*, 1997, 7, 721

[6] Bernstein R. E., Barlow J. W., *Macromolecules*, 1977, 10, 3, 681

[7] Noland J. S., Schmitt J. M., *Adv. Chem. Ser.*, 1971, 99, 15

[8] Nishi T., Wang T. T., *Macromolecules*, 1975, 8, 909

[9] Wang, T. T., Nishi T., *Macromolecules*, 1977, 10, 421

[10] Douglass D., McBrierty V. J., *Macromolecules*, 1978, 11, 766

[11] Chuang H., Han C. D., *J. Appl. Polym. Sci.*, 1984, 29, 2205

[12] Wolf M., Wendorff J. H., *Polymer*, 1989, 30, 1524

[13] Yang H., Han C. D., *Polymer*, 1994, 35, 1503

[14] Mijovic J., Han C. D., *Polym. Eng. and Sci.*, 1982, 22, 4, 234

[15] Paul D. R., Altamirano J. O., *Adv. Chem. Ser.*, 1975, 142, 371

[16] Hirata Y., Kotaka T., *Reports on Progress in Polymer Physics in Japan*, XXⅡ, 1979

[17] Hirata Y., Kotaka T., *Polymer J.*, 1981, 13, 3, 273

[18] Jarray J., Halary L. J., *Macromol Symp.*, 2003, 198, 103

[19] Hosoda T., Gido S. P., Yamada T, *J. Polym. Eng.*, 2013, 33, 49

[20] Tashiro K, *Ferroelectrics*, 1981, 32, 167

[21] Nakamura S., Sasaki T., *Makromol Chem.*, 1975, 176, 3471

[22] Welch G. J., Miller RL., *J. Polym. Sci. Polym. Phys. Ed.*, 1976, 14, 1683

[23] Mancaella L, *Polymer*, 1977, 18, 1240

[24] Prest M. W. Jr., Luca D. J., J Appl. Phys., 1979, 46, 4136

[25] Lonvinger A. J., Keith H. D., *Macromolecules*, 1979, 12, 919

[26] Morra B. S., Stein R. S., *J. Polym. Sci. Polym.* Phys. Ed., 1982, 11, 2243

[27] Hsu T. C., Geil P. H., *J. Mater. Sci.*, 1989, 24, 1219

[28] Tashiro K., Kobayashi M., *Reports on Progress in Polym. Phys. in Japan*, 1987, XXX, 119

[29] Horibe H., Baba F., *Nippon Kagaku Kaishi*, 2000, No.2, 121

[30] Horibe H., Taniyama M., *J. Electrochem. Soc.*, 2006, 153, G119

[31] Li W., Li H., *J. Mater. Sci.*, 2009, 44, 2977

[32] Cao X., Ma J., *Applied Surface Sci.*, 2006, 253, 2003

[33] Tang E., Yuan H., *J. Mater. Sci.*, 2011, 46, 6656

[34] Gregorio Jr. R., Cestari M., *J. Polym. Sci. Part B*, 2012, 32, 859

[35] Chinaglia D. L., Vollet D. R., *J. Applied Polym. Sci.*, 2012, 125, 527

[36] Morra B, Stein R. S., *J. Polym. Sci. Polym. Phys. Ed.*, 1982, 20, 2261

[37] Hasegawa R., Tadokoro H., *Polym. J.*, 1972, 3, 600

[38] Tripathy R., Taylor P. L., *Macromolecules*, 1979, 12, 656

[39] Okabe Y., Saito H., *Polymer*, 2010, 51, 1494

[40] Khambatta F. B., Warner F., *J. Polym. Sci. Polym. Phys. Ed.*, 1976, 14, 1391
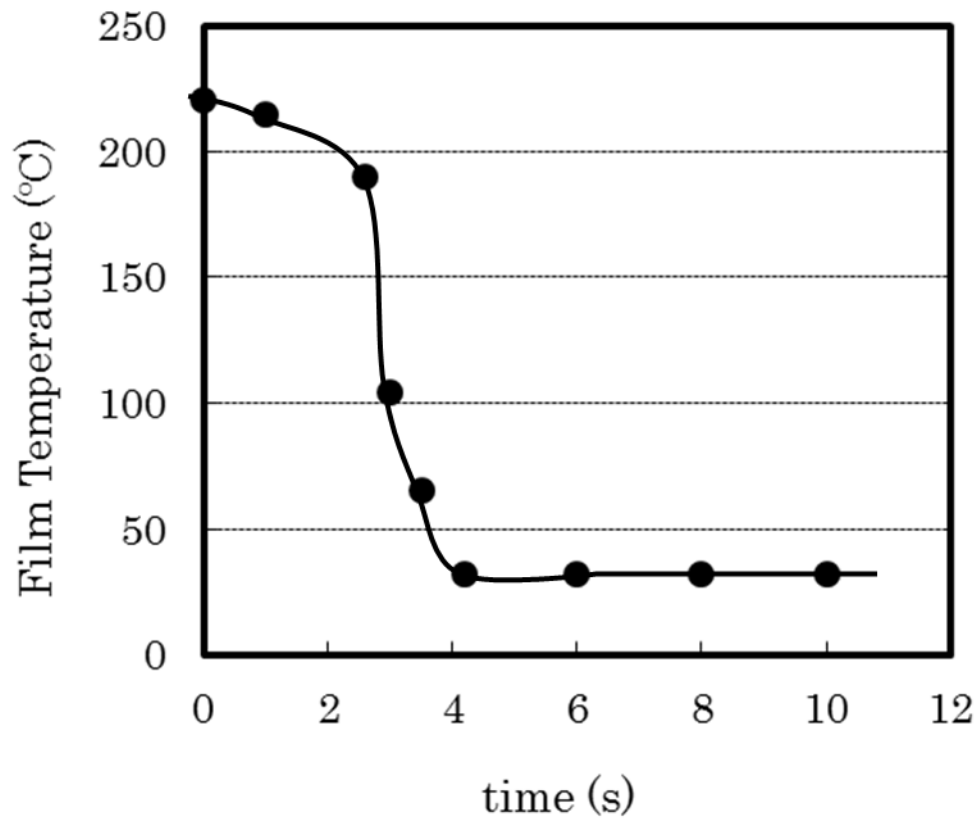
Figure 4-1　The film temperature profile during
the melt casting process.
(Chill roll temperature; 30ºC)
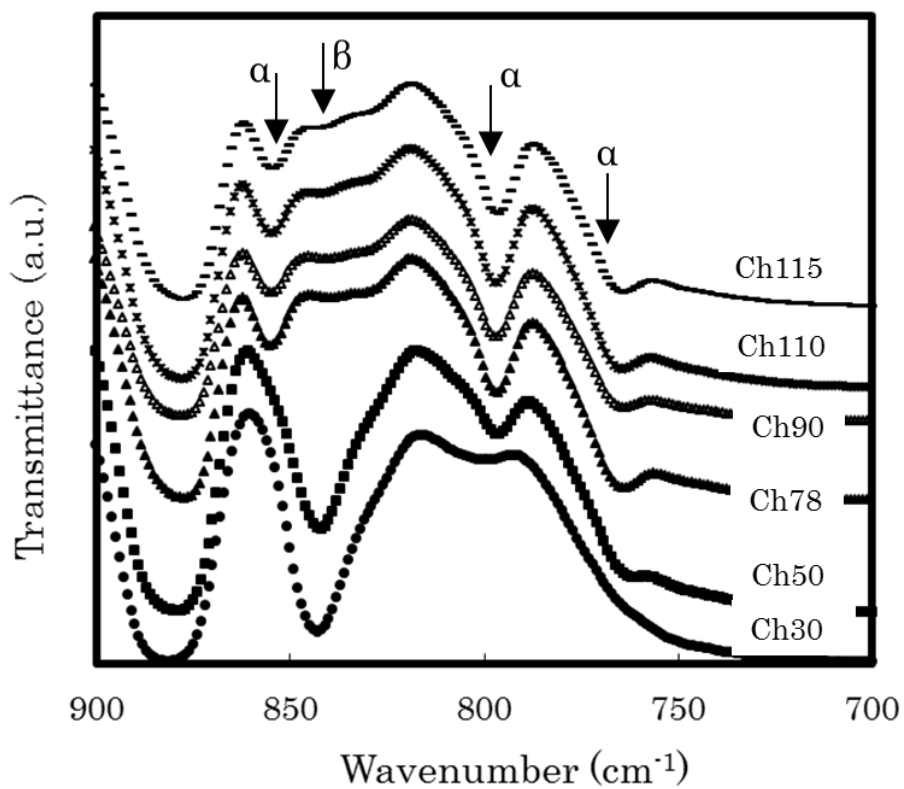
Figure 4-2   FT-IR spectra of films cast at different chill roll temperatures.
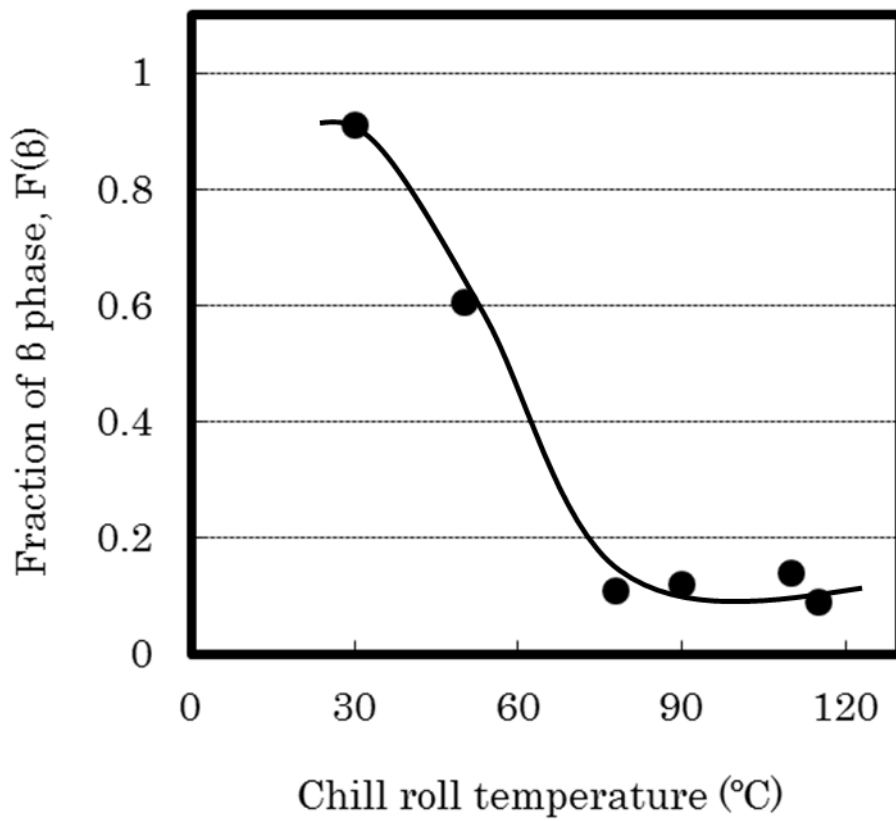
Figure 4-3 Fraction of ß phase, F(ß), of films cast at different chill roll temperatures.
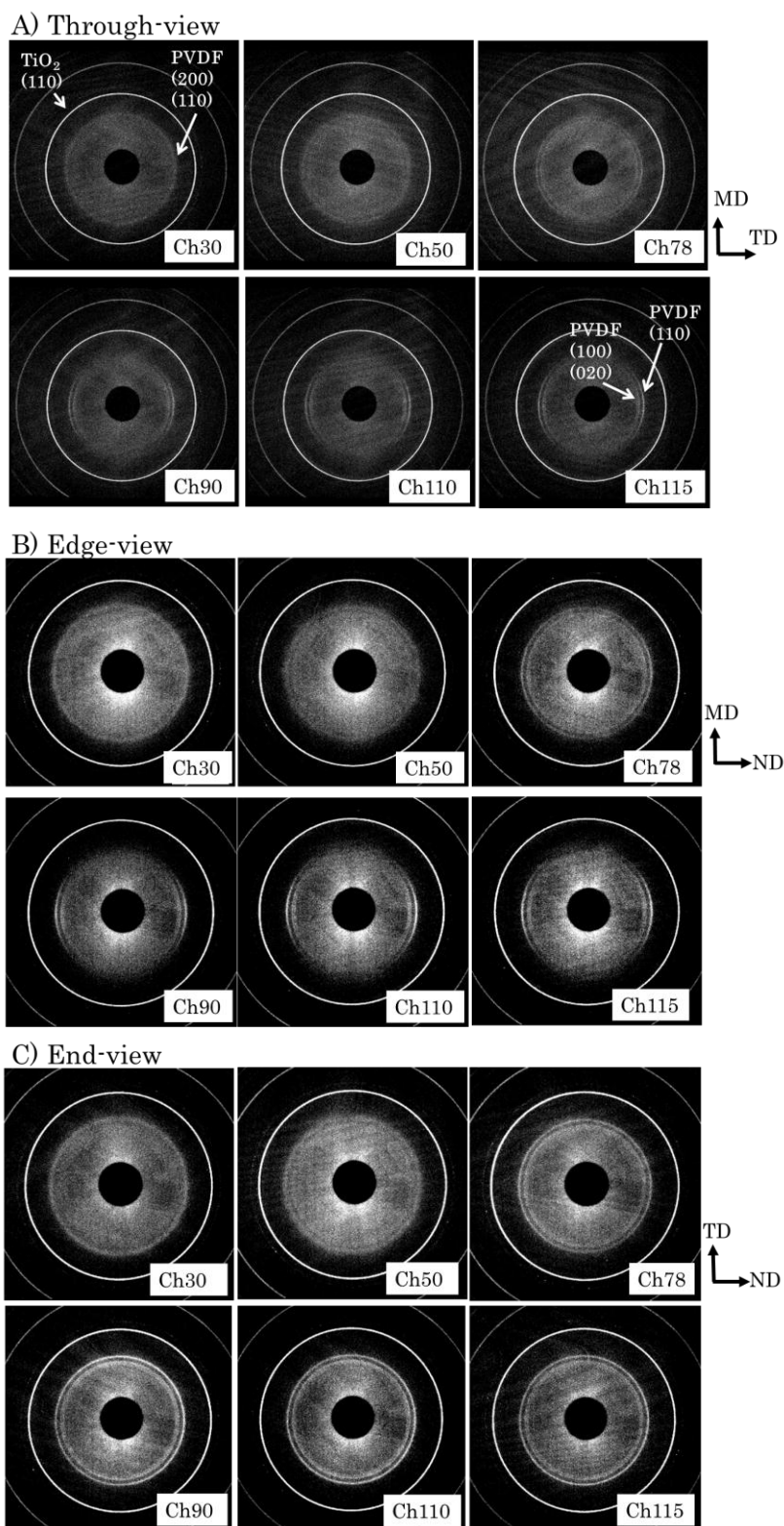
Figure 4-4　WAXD images of films cast at different chill roll temperatures: A) Through-view, B) Edge-view, and C) End-view.
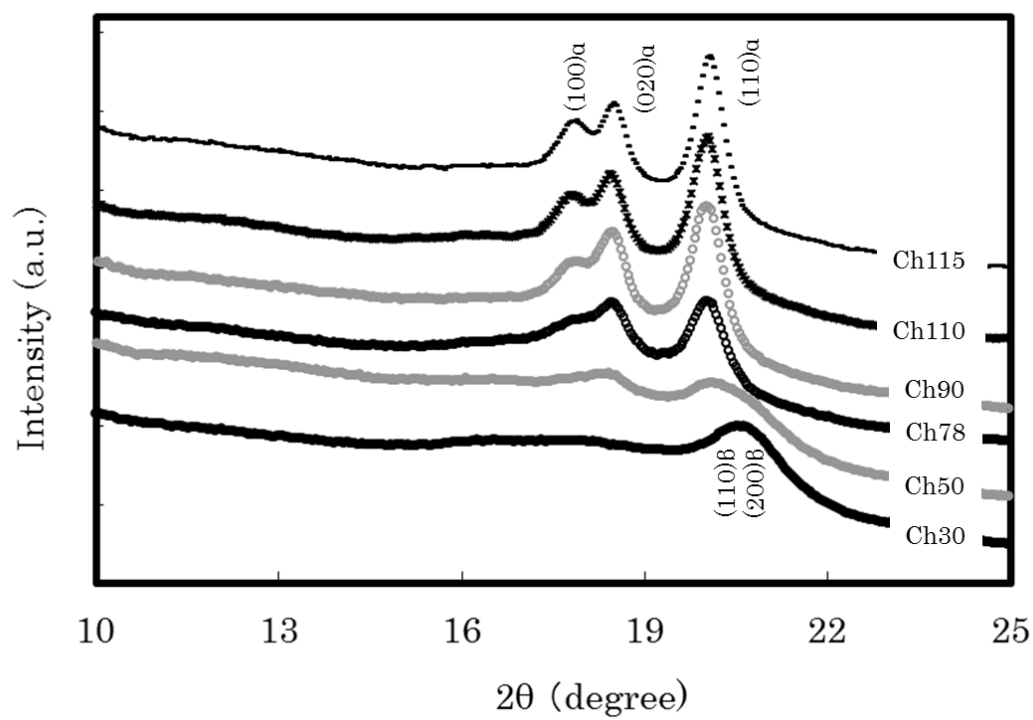
Figure 4-5　WAXD profiles of films cast at different chill roll temperatures.
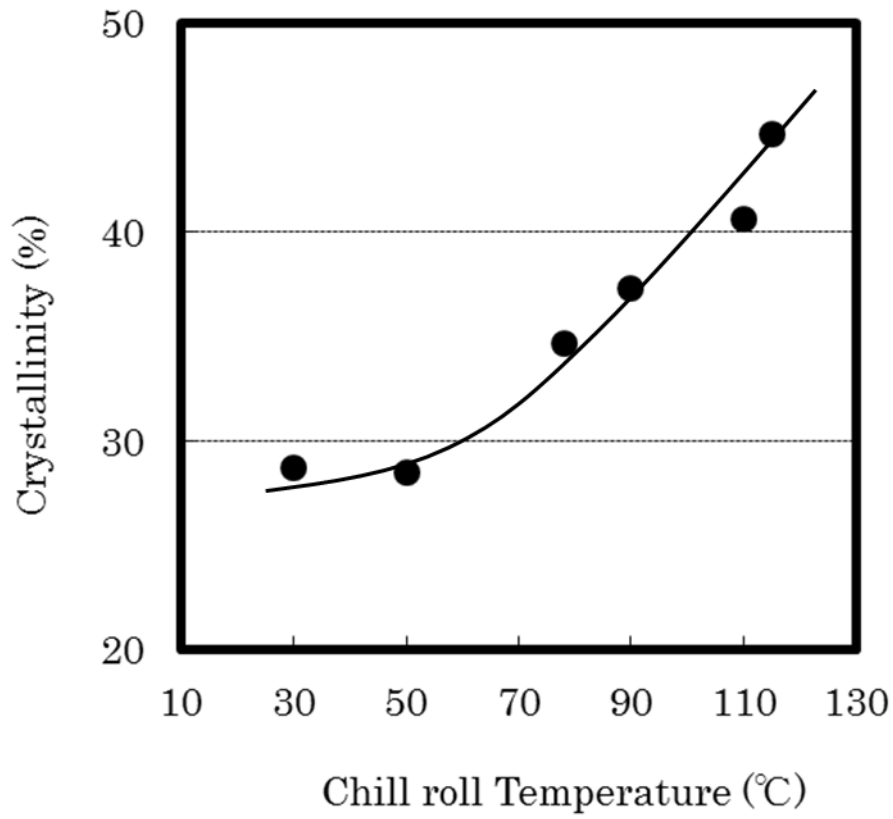
Figure 4-6　Dependence of crystallinity on the chill roll temperature.
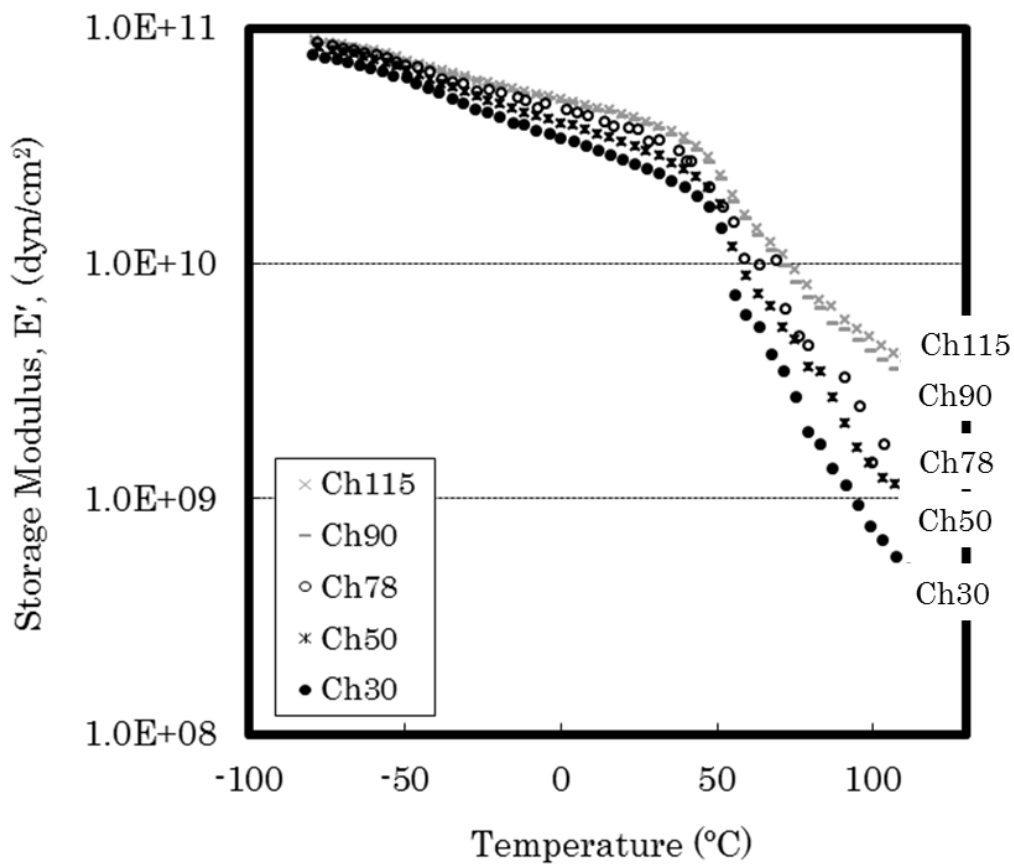
Figure 4-7　Temperature dependence of storage modulus, E′, for films cast at different chill roll temperatures.
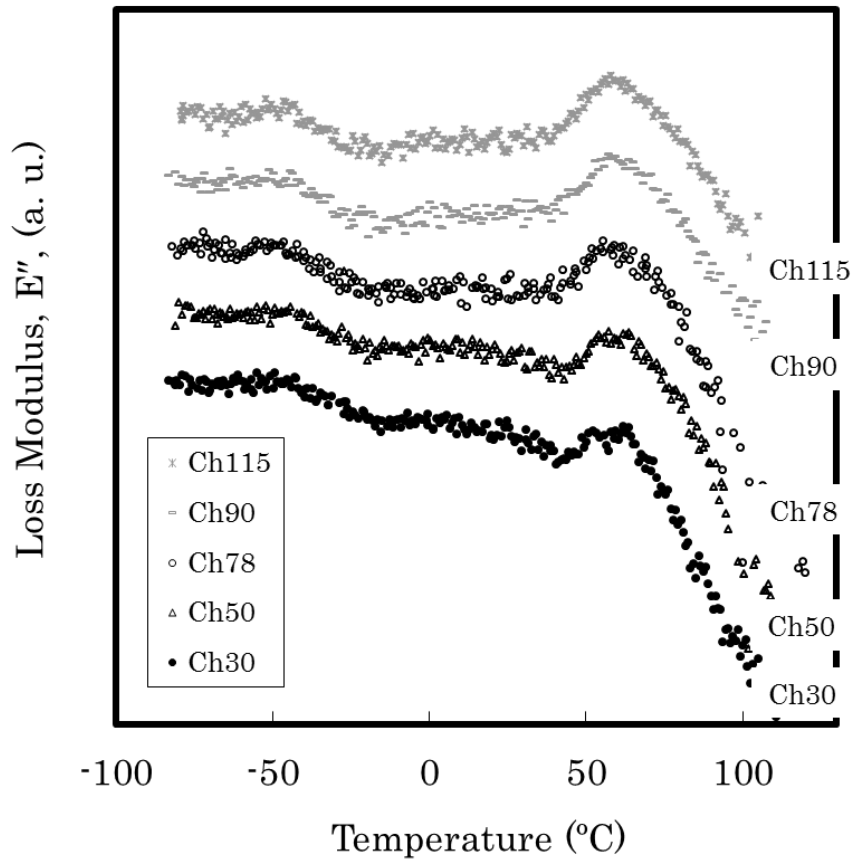
Figure 4-8   Temperature dependence of loss modulus, E″, for films cast at different chill roll temperatures.
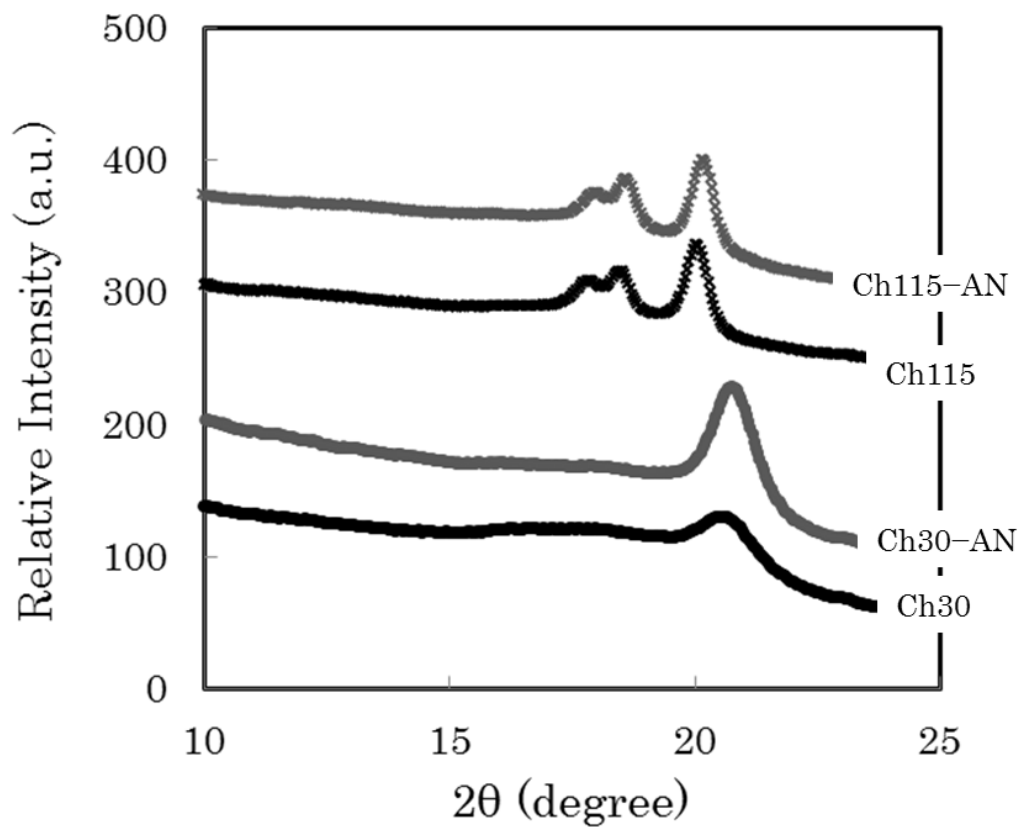
Figure 4-9　WAXD profiles of unannealed and
annealed films.
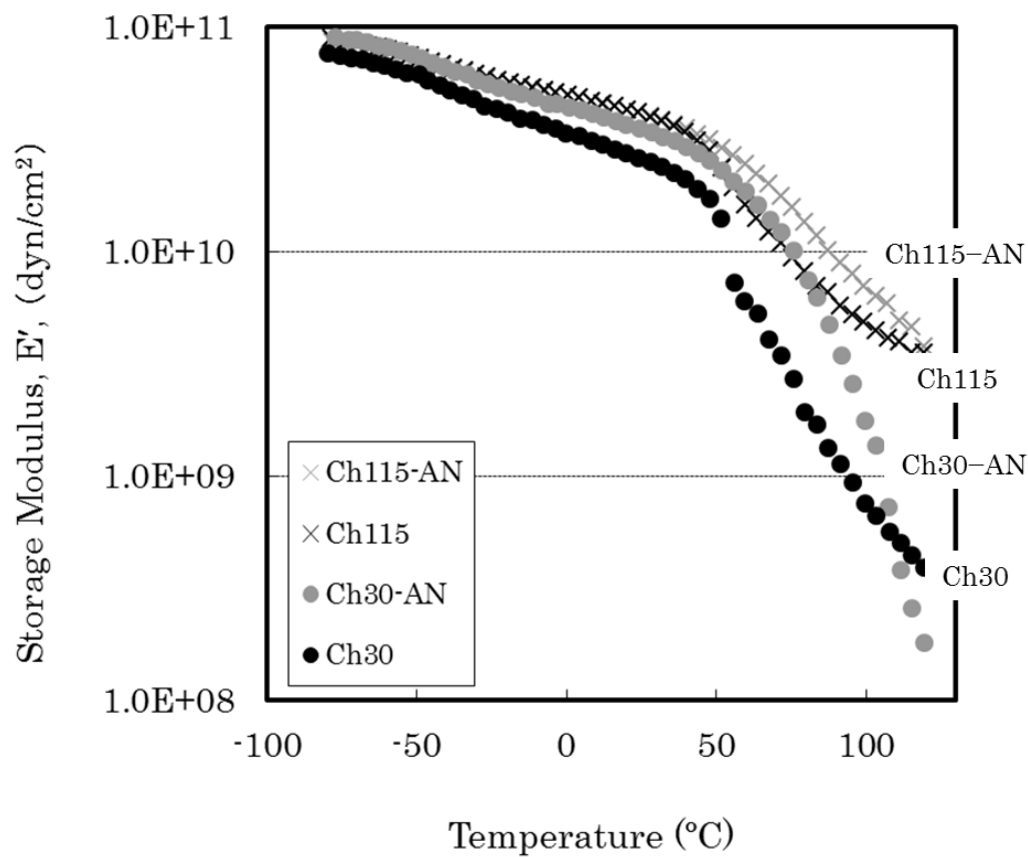
Figure 4-10   Temperature dependence of storage modulus, E′, for unannealed and annealed films.
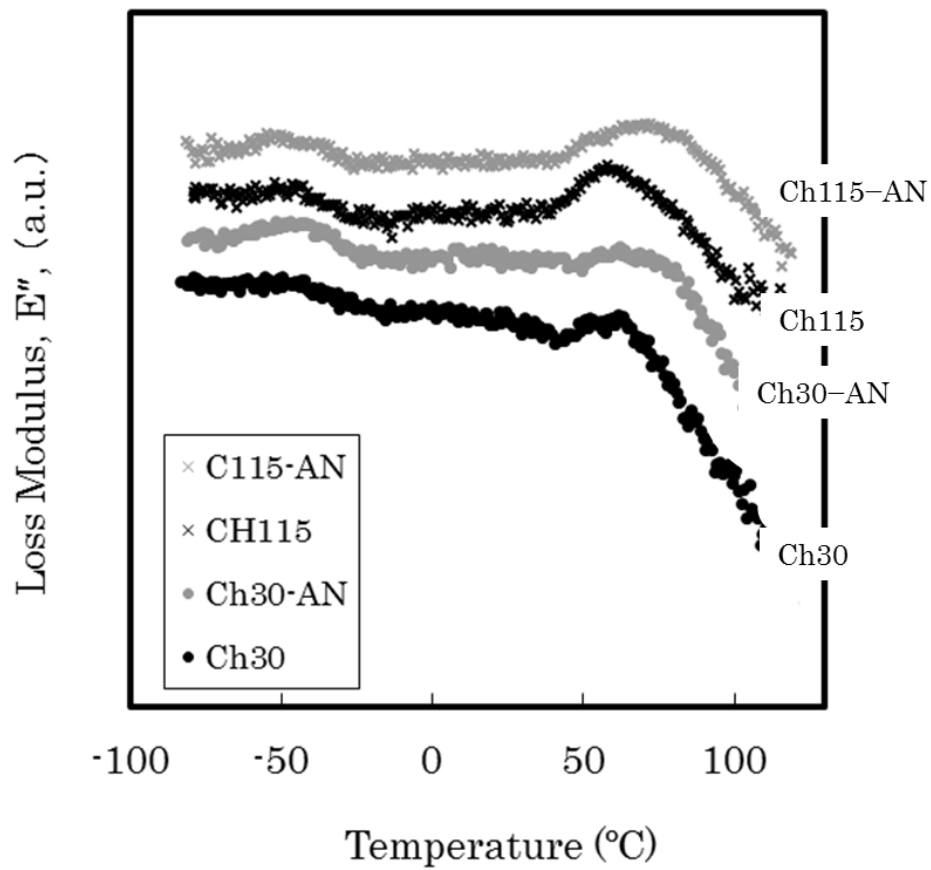
Figure 4-11　Temperature dependence of loss modulus, E″, for unannealed and annealed films.

Table 4-1　Crystallinity, crystal structure and weight fractions of amorphous PVDF phase and PMMA phase

| Sample Code	Chill roll Temperature (ºC)	Annealing Condition	Crystal Structure	Crystallinity (%)	amo.-PVDF weight fraction (%)	PMMA weight fraction (%)
Ch30	30	Unannealed	β	28.7	74.0	26.0
Ch30−AN	30	115ºC for 24 h	β	58.4	62.5	37.5
Ch115	115	Unannealed	α	44.7	68.9	31.1
Ch115−AN	115	115ºC for 24 h	α	48.0	67.5	32.5
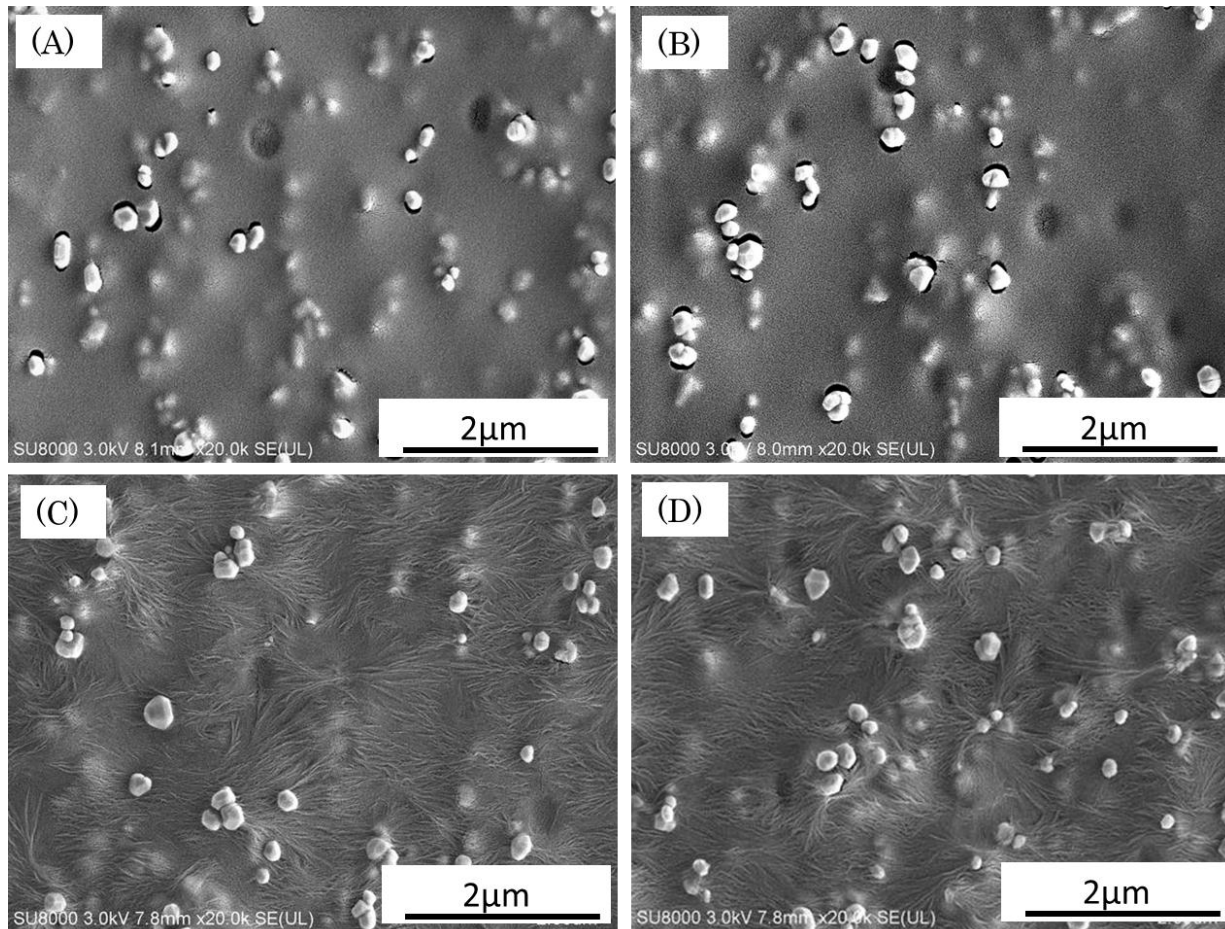
Figure 4-12　SEM micrographs of film surfaces: (A) chill roll side for
Ch30, (B) opposite side of chill roll for Ch30, (C) chill roll side for
Ch115, and (D) opposite side of chill roll for Ch115.
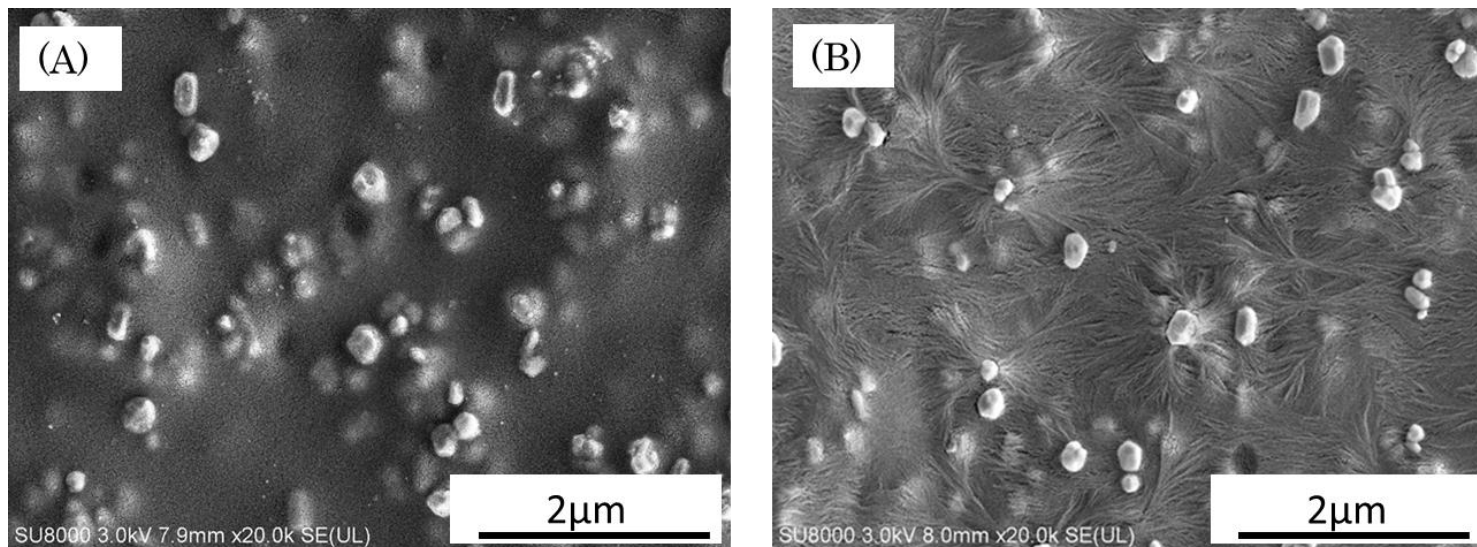
Figure 4-13　SEM micrographs of film surfaces: (A) chill roll side for Ch30−AN and (B) chill roll side for CH115−AN.

Chapter 5.

Conclusion

Effect of solvents and thermal annealing on the morphology development of s-PS-*b*-f-PI and property-morphology-processing relationship on PVDF/PMMA/TiO₂ blend films were studied.

The film of the block copolymer ionomer with an acid form (sH-PS-*b*-f-PI), which cast from THF, developed a well-ordered cylindrical morphology of the f-PI domains in the sH-PS matrix. The morphology was explained by the solubility parameter and the Bjerrum length. Based on the solubility parameter, it was estimated that the sH-PS chains were extended in the solution due to the small difference between the solubility parameters and f-PI chains became more attractive of the large difference in the solubility parameter. In addition, the Bjerrum length suggested that sH-PS chains behaved uncharged block polymers. From those reasons, we could explain that sH-PS blocks having calculated volume fraction of 21.4% formed the matrix phase.

The well-ordered morphology changed to the no-long range ordered structure through thermal annealing at 120°C. This behavior was very different from the usual behavior of uncharged diblock copolymers and was assumed to be due to the ionic cluster formation. In order to reveal the existence of ionic clusters, the block copolymer ionomer with a cesium neutralized form (sCs-PS-*b*-f-PI) was prepared, and IMAXD was conducted.

The sCs-PS-*b*-f-PI films cast from THF/Water (98/2, wt/wt) had a disordered morphology of the sCs-PS matrix and the ionic cluster formation. Both the morphology and the ionic cluster formation did not change by thermal annealing at 140°C. It was considered that adding a small amount of water to THF helped the ionic cluster formation and induced a stable structure. In case of using DMSO as a solvent, the lamellar morphology and a small amount of the ionic cluster formation were developed. The lamellar morphology was explained by the solubility parameter and the Bjerrum length. With thermal annealing at 140°C, the promotion of ionic aggregation and the increase of lamellar d-spacing were observed. This experiment exhibited that the promotion of the ionic aggregation and the increase of the free energy in each chain in the lamella.

Our results grasped the promotion of the ionic cluster formation owing to water

and thermal annealing, and it was deduced that the order-disorder transition seen in sH-PS-*b*-f-PI was induced by the ionic cluster formation.

PVDF/PMMA/TiO$_2$ blend films were prepared by a melt casting process, and property-morphology-processing relationship was studied in terms of TiO$_2$ contents and anisotropy. As increasing TiO$_2$ content, tensile moduli in both the MD and TD increased. The values of tensile moduli calculated by the Halpin-Tsai and Kerner model were consistent with the values of experimental moduli in both the MD and TD for PVDF/PMMA blend films containing 10 wt% TiO$_2$. However, the values of experimental tensile moduli exhibited smaller values compared with the values of calculated ones, as the TiO$_2$ content increase to 30 wt%. Based on morphological observations, it was revealed that TiO$_2$ particles did not affect the crystal structure of PVDF and the morphology of the amorphous phase. In addition, the decrease of crystallinity with increasing TiO$_2$ content was due to the hindrance of crystal growth by some TiO$_2$ particles, even though different TiO$_2$ particles acted as a nucleus regent.

The MD elongation at break showed more than 200%, and the TD elongation at break exhibited less than 20%. It was observed that sheaflike spherulites can deform along the MD when tensile force was applied along the MD. By contrast, those spherulites were fractured when tensile force was applied along the TD. It was observed that the amorphous phase existing within the interlamellar region could be stretched and sheaflike spherulites themselves could not deform. Such anisotropic properties were due to the morphology of the anisotropic spherulites formed by the orientational effect.

It was found that the crystal structure of PVDF changed from the ß phase to the α phase with increasing chill roll temperature. Specifically, the film cast at the chill roll temperature of 30°C formed the ß phase of PVDF, and the film cast at the chill roll temperature of 50°C exhibited both the ß and α phase, and the film cast at chill roll temperature of more than 78°C formed the α phase. It was clarified that the ß phase maintained after the annealing of 115°C-24 h. For all samples, a decrement in E´ became smaller in the temperature region above the T$_g$ ascribed to the mixed amorphous phase, as the chill roll temperature increased. It was expected that the decrement in E´ above T$_g$ was caused by differences in the crystallinity of the films, and we annealed the film cast at the chill roll temperature of 30°C and 115°C. As a result, it was indicated that the difference in the E´ curves of the films cast at the different chill roll temperature was not

caused by variation in crystallinity but by other factors. Based on the previous studies, it was deduced that a large amount of PMMA is entrapped within the interlamellar region in the spherulites in the film cast at chill roll temperature of 115°C. On the contrary, in the film cast at chill roll temperature of 30°C, PMMA uniformly exits in mixed amorphous phase. The morphological observation supported our deduction and the morphology was due to the difference of growth rate between the α and β phase. As a result, it was assumed that the actual weight fraction of PMMA in the mixed amorphous phase in the film cast at chill roll temperature of 115ºC became lower compared with that of 30 ºC.

The study revealed the microphase-separated structure of the newly-synthesized block copolymer ionomers, in terms of the solvent effect and the Bjerrum length, and the ionic cluster formation using SAXS, IMAXD, and TEM. In the study of PVDF/PMMA/TiO$_2$ blend films prepared by a melt casting process, we revealed that the elongation at break was dominated by the anisotropic morphology of spherulites and that values of E′ above T$_g$ was influenced by the ratio of PVDF and PMMA. Such mechanical properties are one of the important properties in practical usage, and it is expected that properties of polymers will be increasingly controlled through study of property-morphology-processing, hereafter.

Research Contribution

1. List of publications

Chapter 2

<u>Tomonori Hosoda</u>, Samuel P. Gido, Jimmy W. Mays, Tianzi Huang, Chong Rae Park, Toshiro Yamada

"Effect of solvents and thermal annealing on the morphology development of a novel block copolymer ionomer: a case study of sulfonated polystyrene–block–fluorinated polyisoprene"

（新規なブロックコポリマーのモルフォロジー形成における溶媒と熱処理が及ぼす影響：スルフォン化ポリスチレン−フッ素化ポリイソプレンブロックコポリマーについて）

Journal of Polymer Engineering, vol. 33, pp.49−59, 2013. 03

Chapter 3

<u>Tomonori Hosoda</u>, Toshiro Yamada

"Effect of TiO_2 on morphology and mechanical properties of PVDF/PMMA blend films prepared by melt casting process"

（溶融成形法によって得られた PVDF/PMMA ブレンドフィルムのモルフォロジーと力学特性に TiO_2 が及ぼす影響）

Journal of Applied Polymer Science, accepted, 2014. 01

Chapter 4

<u>Tomonori Hosoda</u>, Toshiro Yamada

"Morphological study of PVDF/PMMA/TiO_2 blend films prepared by melt casting process"

（溶融成形法によって得られた PVDF/PMMA/TiO_2 ブレンドフィルムのモルフォロジーに関する研究）

Journal of Polymer Engineering, vol. 33, pp. 639-649, 2013. 11

2. Proceedings

2-1 <u>Tomonori Hosoda</u>, Samuel P. Gido, Jimmy W. Mays, Tianzi Huang, Chong Rae Park, Toshiro Yamada

"Effect of solvents and thermal annealing on the morphology development of a novel block copolymer ionomer: a case study of sulfonated polystyrene−block−fluorinated polyisoprene"
（新規なブロックコポリマーのモルフォロジー形成における溶媒と熱処理が及ぼす影響：スルフォン化ポリスチレン−フッ素化ポリイソプレンブロックコポリマーについて）
Proceedings of Asian Workshop on Polymer Processing 2012（AWPP2012），
要旨集、pp. 34−37, 2012. 08

2-2 Tomonori Hosoda, Samuel P. Gido, Tianzi Huang, Jimmy W. Mays
"Morphology of Fluorinated and Sulfonated diblock Copolymers
（フッ素化およびスルフォン化されたダイブロックコポリマーのモルフォロジー）
Proceedings of American Physical Society March Meeting, Baltimore, MD, March 13-17, 2007
プログラム、pp. 11, 2006. 03

3. Patents
3-1. 細田 友則、雑賀 徹
"キトサンを含有する組成物及びそれからなるフィルム
特開 2002−327090

3-2. 細田 友則、飛田 寿徳
"熱処理ポリ−p−フェニレンスルフィドフィルムの製造方法
特許第 5069545 号　2012 年 8 月登録

3-3. 大倉 正之、細田 友則
"触媒層形成用転写シート及びこれを用いた膜−電極接合体の製造方法
特許第 5184138 号　2013 年 1 月登録

3-4. 細田 友則、佐藤 祐輔、大場 弘行、赤津 正道、小松崎 哲也
"ポリフッ化ビニリデン樹脂フィルム、多層フィルム、及び太陽電池モジュール用バックシート、並びに、フィルムの製造方法"
WO 2012/172876 A1

4. Book

4-1. 大杉 透、細田 友則
　　書籍名：フィルムの機能性向上と成形加工・評価技術
　　監修、金井 俊孝
　　発行所、株式会社 AndTech
　　"第 5 章、次世代太陽電池用バックシートの開発"